Inferring 3D Cellular Forces from Confocal Image Stacks

by

Ahmad Ehsandar

A thesis
presented to the University of Waterloo
in fulfillment of the
thesis requirement for the degree of
doctor of philosophy
in
Civil Engineering

Waterloo, Ontario, Canada, 2015

AUTHOR'S DECLARATION

I hereby declare that I am the sole author of this thesis. This is a true copy of the thesis, including any required final revisions, as accepted by my examiners.

I understand that my thesis may be made electronically available to the public.

Abstract

If we are to understand why cells move in contexts such as early embryo development, wound healing, cancer metastasis and construction of engineered organs, and if we are to learn how to better influence their associated medical outcomes, we must learn how to determine, in detail, the forces that are involved in cell movement and shaping. Significant progress has recently been made in this direction through force inference techniques that allow us to estimate the net forces along individual cell-cell and cell-medium interfaces, in epithelia and other two dimensional (2D) aggregates, from images and time-lapse movies.

The goal of this thesis is to show how current 2D force inference techniques can be extended to three dimensional (3D) systems. As part of this process, I developed a software toolbox to accurately digitize cell outlines of 2D images extracted from a confocal stack. The digital information was then used to construct a 3D aggregate. These 3D reconstructions allowed the calculation of cell contact angles and face curvatures which were then used to build force balance equations for each set of contact angles. Together, these equations were used to calculate, a self-consistent, scalable set of values for the interfacial tensions along each cell-cell and cell-medium interface. If experimental values are available for some of these tensions, then the set can be properly scaled. The equations assume the system to be static, with all forces and junctions in equilibrium. To be consistent with this assumption, image sets with negligible amounts of deformation over time were used in this work.

To validate the proposed algorithm in this thesis, it was applied to computer-generated synthetic data sets for which the ground truth tensions and pressures were known. The

synthetic data was generated for two different aggregate sizes generated by two completely different techniques. A smaller patch included fifteen cells generated by the Voronoi technique, whereas a larger patch included thirty three cells generated with software named “Surface Evolver”. Both geometries were annealed and then sliced along the z-axis to generate a synthetic image stack.

The 3D code is equipped with two different face fitting algorithms for estimating contact angles: sphere fitting and point cloud projection. Analysis of the results demonstrated that a hybrid method in which external cells are fitted with spheres, and internal cells are fitted with point clouds, leads to the best tension calculations (within 6% of their true values). The accuracy of the results depends on the number of slices over the entire aggregate. The author determined that having nine slices per cell is the minimum for obtaining face tensions with error of less than 10%. Analysis of biological data showed a good match between the tensions calculated using this approach and those obtained from physical experiments.

Acknowledgements

First and foremost I want to thank my advisor, Professor G. Wayne Brodland, for his guidance, encouragement and patience over the last four years. He has shown me how good research depends on being meticulous and thorough. I also appreciate his contribution of time, ideas, and funding to make my Ph.D. a productive experience. His joy, passion and wisdom in research to make the world a better place will always linger in my mind. I would also like to thank my lab-mate Jim Veldhuis for his help, invaluably constructive criticism and friendly advice. Finally, I want to thank Dr. Simon Cox of the Aberystwyth University for his help with Surface Evolver.

I also want to thank my family. Words cannot express how grateful I am to my parents, and my lovely sisters and brother for all of the sacrifices that you've made on my behalf. Special thanks to my beloved wife, Aida who supported me in so many ways, especially during the difficult moments.

Dedication

I dedicate this thesis to my family for nursing me with affections and love and their dedicated partnership for success in my life.

Table of Contents

List of Figures

List of Tables

Chapter 1
Introduction

Embryonic cells take on specific arrangements and undergo particular self-driven motions in order to form mission-critical structures. For many years, it has been widely recognized that if these arrangements and motions do not occur properly, birth defects can result (Cowin 2000, Trinkaus 1984, Clausi, Brodland 1993). This observation gives rise to such questions as: what drives cells to move in the ways that they do? What are the governing principles that determine how they rearrange? For a biological system, the answer to these questions may lie in the fields of physiology, chemistry or medicine. However, from a mechanical point of view, one can say with certainty that mechanical forces must be acting along the edges of the cells, otherwise, no motion would result (Glazier, Graner 1993).

More recently, it has been recognized that cell movements play a significant role in a much broader range of biological processes from wound healing to tissue engineering to cancer metastasis (Nodder, Martin 1997, Trinkaus 1984, Walgenbach, Voigt et al. 2001, Chaffer, Weinberg 2011). Understanding the forces involved in these processes is crucial to understanding the causes of their respective cell motions. It is hoped that a deeper knowledge of the relationship between cell motion and the forces that drive it, will open up new horizons

and lead to new (and vastly improved) clinical prevention or treatment strategies relevant to birth defects, wound healing and cancer.

The cellular level forces can arise from cytoskeletal and membrane adhesion (active) and cytoplasm viscosity (passive). The latter one is only available when the cytoplasm undergoes deformation which results in dissipation of the energy in cytoplasm. The microfilament network available in cytoplasm is capable of generating contractile force on membrane opposing the adhesion forces generated by the proteins in the membrane structure. The amount of these forces varies for different neighbor cells or medium. These separate forces can be replaced with a resultant force vector tangent to the membrane and usually referred as membrane force.

One process that has received particular attention is cell sorting, where multiple types of cells brought together in an aggregate will spontaneously sort themselves out according to their histological type. The cell movements that drive sorting turn out to be driven by differences in interfacial tensions, as are the motions that produce a wide range of phenomena, including cell dissociation, cell and tissue engulfment and formation of checkerboard patterns (Brodland 2002, Brodland, Chen 2000a, Steinberg 1970, Steinberg 1996). These interfacial tensions also drive single cell invasion and the motions associated with cancer metastasis (Kumar, Weaver 2009).

Interestingly, these same forces have also been found to drive the wound healing process (Wong, Akaishi et al. 2011, Dahmann, Oates et al. 2011, Brugues, Ester et al. 2014). Once the protective barrier provided by a monolayer epithelium is broken, the wound healing

process is set in motion. It starts with certain biochemical events and leads to proliferation and movement of epithelial cells so as to reseal the injured site. Again, interfacial tensions, including purse-string forces along the wound edge, play a key role in the closure process (Clark, Henson 1988).

It is now clear that in order to understand and possibly manipulate the full range of cell movements, it is vital to be able to measure or calculate, in detail, the forces that drive cells (Campas, Mammoto et al. 2014). It is very difficult to measure these forces experimentally. Limited information can be obtained from atomic force microscopy (AFM) (Thomas, Burnham et al. 2013, Sun, Graham et al. 2005) and laser microsurgery (LM) (Hutson, Veldhuis et al. 2009). Micropipette aspiration can only yield surface tensions (Maitre, Berthoumieux et al. 2012) and the substrate deformation technique is limited to traction forces (Legant, Miller et al. 2010, Tambe, Croutelle et al. 2013). The main problem with these techniques is that they typically provide information at a single point only, and several are destructive to the cell and surrounding tissues. Furthermore, some of techniques can only be applied to cells on the surface of a mass or to monolayer cells/tissues.

Video force microscopy (VFM) is a recently developed computational method that can calculate a detailed map of the surface tensions present in a two dimensional (2D) cellular system (Brodland, Conte et al. 2010). Introduced by Brodland and his group, VFM is the first non-ablative technique in which a complete map of forces within an aggregate can be provided. In this technique, all passive forces are considered to be replaced by an effective viscosity μ at the strain rates characteristic of morphogenetic movements (responsible for dissipating the energy generated in the cell) (Brodland, Conte et al. 2010). In this approach,

the tissue or an aggregate is divided into small regions corresponding to cells or groups of cells. Each node is then tracked through the process of interest in time-lapse movies. Then, inverse finite element (FE) analysis is used to determine the net force that needs to act on each node (based on the viscosity μ) to make the cells move as observed. VFM then uses inverse methods to determine the forces that must act along each cell edge in order to drive the observed motions.

The VFM approach was first implemented on 2D movies of cross-sections of *Drosophila* embryos (Figure 1-1) undergoing ventral furrow formation (Brodland, Conte et al. 2010). In that context it was possible to reveal the forces acting along individual cell edges.

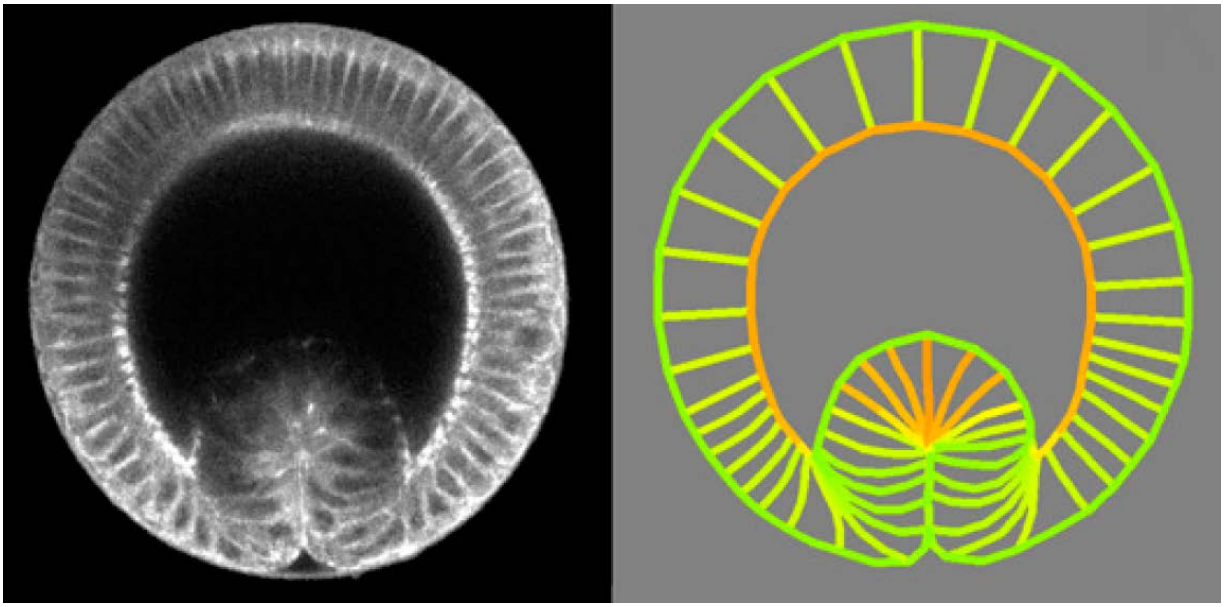

Figure 1-1 – VFM results of Drosophila melanogaster. Warmer colors show the higher tensions calculated in that spot (Brodland, Conte et al. 2010).

The VFM approach spurred development of another computational method called the Cellular Force Inference Toolkit (CellFIT). When it is used, cells in an image are digitized

into a computerized model with equilibrium equations for each triple junction (TJ) (Brodland, Veldhuis et al. 2014). These equations are assembled based only on the edge tensions and the angle at which they reach the TJ. Overall, for an aggregate of several cells the system is overdetermined. Therefore, a solution can be obtained even if a number of edges are not included in the equations (e.g., due to poor image quality or geometrical difficulties). The solution provides a set of relative tensions which can only be scaled to correct values using an external measurement (Figure 1-2). Later, intercellular pressures can also be calculated by means of Laplace equations. Again, an external reference is required to obtain true pressure values. Although this technique is able to calculate the tensions and pressures of a cell or group of cells, it can only be applied to 2D aggregates.

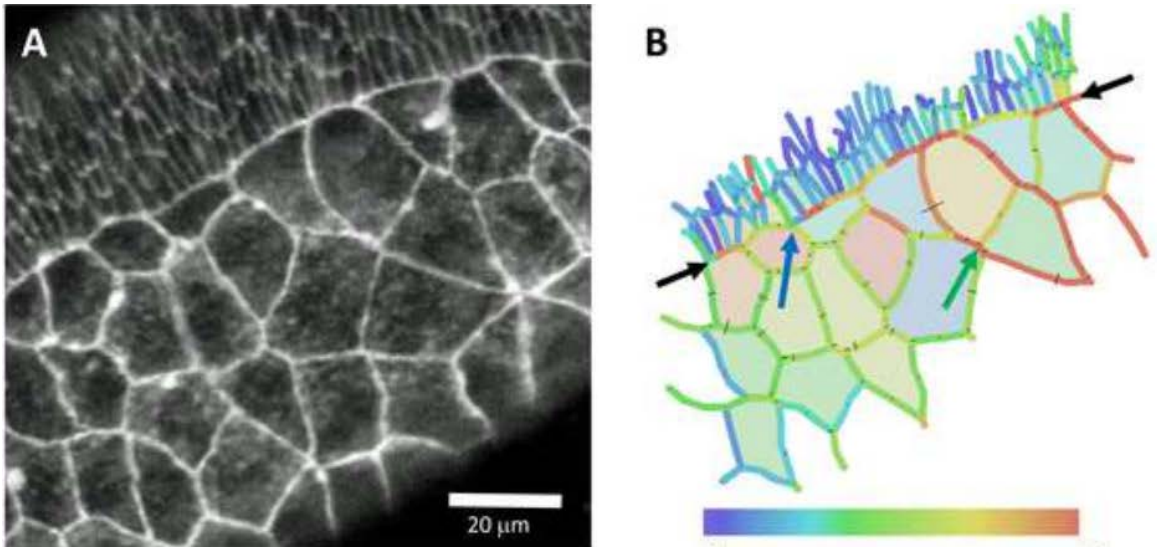

Figure 1-2 – (A) Shows an image of dorsal closure in a live Drosophila embryo. (B) Shows tensions and pressures calculated using CellFIT. The color spectrum from red to blue indicates high to low values, respectively (Brodland, Veldhuis et al. 2014).

Many cell motions of practical interest, from sorting to tissue self-assembly and cancer invasion, are fundamentally three dimensional (3D), and it is imperative to develop methods for 3D systems. However, by comparison with 2D systems, 3D methodologies present a number of inherent challenges that make them far more complex to develop. For example, 3D cell geometries must be reconstructed from confocal stacks, however, geometric information is invariably missing due to the distances between images in the stack and the angles of interest being skewed to the image planes. The goal of this thesis is to present a novel approach that overcomes these challenges and allows the tensions acting along cell-cell and cell-medium interfaces in 3D aggregates to be determined.

This approach uses a Watershed Algorithm to convert the images into cell tracings other software modules convert these tracings into a model representation in terms of nodes, edges and cells. Next, this information is used to construct a 3D Point Cloud (PC) model from which geometric data such as dihedral angles and tangent vectors for each of the 3D faces can be determined. In the end, a system of equations are assembled together and solved in least square manner. The solution gives the tensions that act along each cell face.

In order to validate the results, sets of synthetic data for which ground truth values were known were analyzed. When images in the stack were spaced sufficiently close together, such that on average each cell appeared in thirteen sections, tension values were found to be within 6% of their true values. The technique was also applied to 3D aggregates containing a mixture of two cell types, a situation that produces five distinct interface types, and the calculated edge tensions agreed well with experimentally-determined values.

Chapter 2
Literature Review

This chapter provides background on the cellular forces that drive and regulate cell motions. Section 2.2 summarizes the leading hypotheses which have been developed to describe cell movements and associated behaviors at the tissue level. Then, in Section 2.3, the role of cellular forces is discussed in the context of several embryological phenomena as well as a few diseases. Next, in Sections 2.4 and 2.5, the most recent force models and experiments are explained and categorized based on their methods. Finally, Section 2.6 outlines a new 2D technique that can obtain a map of cellular forces using confocal imaging techniques.

2.1 Source of Physical Forces

The membrane tension derives from both active and passive components. The active forces derive from components such as actomyosin networks, the cell membrane and its associated proteins, cell adhesion systems and microtubules, as these components act like motors that generate force and drive motions. Cell adhesion systems generate forces opposing the contractile forces (Brodland 2002). The resultant active force makes the passive components

such as cytoplasm and intermediate filament network move, and they dissipate system energy.

The net force along the cell membrane can be replaced by a single resultant tangent to the membrane (Figure 2-1). These force vectors are usually replaced with tensions (γ) that corresponds to the stress resultant (N/m) in each membrane. Since the height of the sheet of cells is assumed to be constant, the tension values can be reported as an amount of in-plane force N along each cell boundary.

It is commonly assumed that the volume of each cell is constant, and as a result the liquid in the cytoplasm must generate an internal pressure to balance the face tensions. This internal pressure might be different from one cell to another in an aggregate because of differences in cell tensions and sizes. Pressure differences across cells can cause the membrane to take a convex profile.

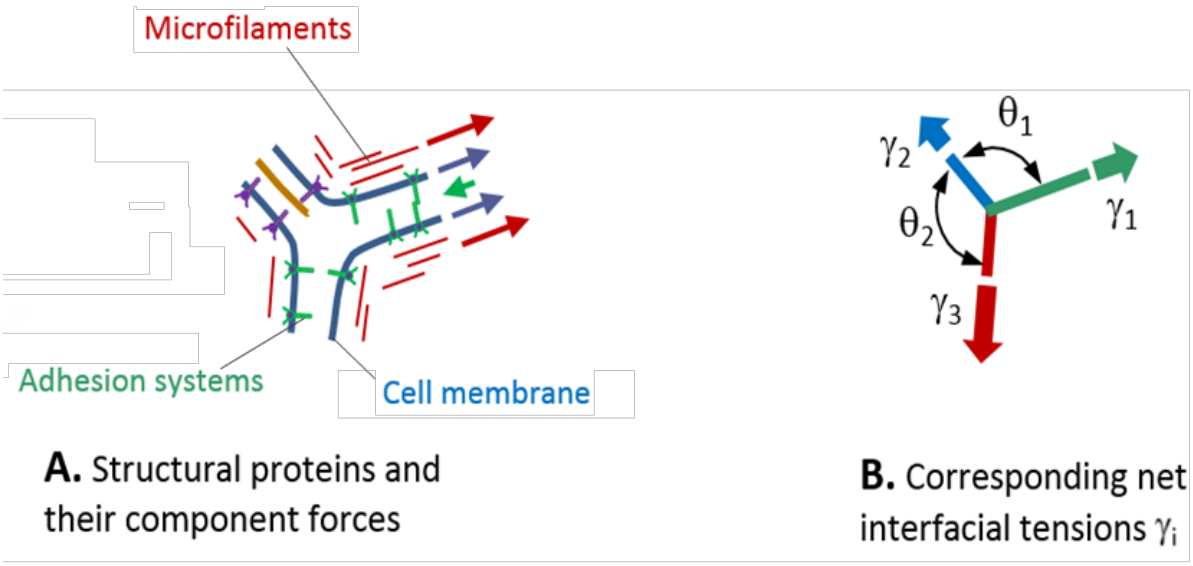

Figure 2-1 – Sources of Membrane Tensions

2.2 Theories of Cell Movement

The starting point in the process of investigating cell-cell interactions is the same as that for any other system governed by physical principles; for cells to move, and ultimately take on specific geometries, particular forces must be at work. During the last few decades, several models and hypotheses have been devised to explain cell sorting and other cellular phenomena. However, none of these concepts provide a basis for quantitative measurement of the forces producing the observed motion of cells. Measuring these forces is crucial to an in-depth understanding of cell rearrangement and other cell movements. Most studies to date have focused on learning about the sub-cellular structural components and gene networks that generate these forces rather than on their magnitudes and other mechanical characteristics. The three most dominant theories about the nature of the forces that drive cell motions are briefly discussed in this section. From these theories, it is possible to determine which of the many forces at work in cells are important to measure.

2.2.1 Differential Adhesion Hypothesis (DAH)

Undoubtedly one of the most widely known and accepted hypotheses in cell sorting is the Differential Adhesion Hypothesis (DAH), proposed by Steinberg in 1963 (Steinberg 1963). The whole idea of the DAH, came from similarities observed between the behavior of cells and liquids. When two immiscible liquids are mixed, individual droplets of one liquid round up and fuse together with the ultimate result that one fluid sorts out from the other – the same phenomenon that happens in cell sorting. Since the physical behavior of liquids is a well understood field in mechanics, the sorting behavior of liquid molecules can be easily explained based on differences in surface tensions (Adam 1968). Intermolecular forces is the

force acting between any two liquid molecules. The intensity of the intermolecular attraction is subject to change for different types of liquids. Furthermore, molecules at the surface of a droplet will experience a net inward force which is proportional to the surface tension for a given liquid. In the case where two immiscible liquids are mixed together, molecules with stronger attraction for one another tend to come together at the center and be engulfed by molecules which attract one another less strongly. According to DAH, cells in an aggregate can be considered as molecules in a droplet and the adhesion force between cells as equivalent to the intermolecular forces. To quote Steinberg (Steinberg 1970), “the differential adhesion hypothesis attributes sorting out behavior to differences in the strengths of intercellular adhesion. It suggests that cells in mixed population rearrange themselves to minimize their total adhesive free energy.” In other words, the DAH states that cell sorting is a procedure in which cells seek to maximize their intercellular attraction, consequently leading to a configuration associated with minimum adhesive free energy.

To support their hypothesis, Steinberg and his group performed three types of experiments (Steinberg 1970). In the first experiment, the transitivity of the hierarchical sequence of segregation was shown. For this experiment, six types of cells were used including: heart, neural tube, epidermal epithelium, precartilage, pigmented epithelium, and liver. The results appeared to be consistent with their theory. The second experiment showed that their hypothesis for sorting behaviors could be extended to engulfment as well. That is, if two masses of different types of cells are placed in contact, the cells that engulf the other type of cell are the same cells that sort out externally in the first experiment. Their third experiment demonstrated the resistance of different types of cells to flattening in a centrifugal field

(Phillips, Steinberg 1969). Here, they showed that the cells with higher adhesive forces are more resistant to flattening in the centrifugal field.

Although Steinberg and his group provided some evidence in support of their hypothesis, there remained several challenges to their theory that were left unresolved. Harris (Harris 1976) outlined these challenges. According to him, Steinberg's analogy between liquid surface tension and the effective surface tension of cell aggregates took several premises for granted that must be validated. In this regard, Harris raised the following objections to Steinberg's analogy:

1. Cells are alive while liquid molecules are not. Since cells can generate energy within their system, they cannot be considered thermodynamically closed systems akin to liquid molecules.
2. While forces like van der Waals, hydrogen bonding or even electrostatic forces, which explain close range attraction between molecules, are active at a range of distances between cells, cell adhesion is based on junctions like covalent bonds, antibody-antigen, enzyme-substrate-like complexes and Desmosome junctions, which are formed when cells are in contact with each other.
3. The breakdown of the aforementioned cellular adhesion bond is not the reverse of its formation process.

Although the DAH seemed to explain phenomena such as cell sorting and engulfment and predict their result based on the adhesion forces, its result was not consistent with many other cases. For instance, in the presence of membrane contraction, the apparent adhesion forces

would increase as the membrane shrinks and the density of the adhesion molecules increases. However, the DAH assumes that the adhesion forces associated with a face is only a function of the cell types that form the interface.

2.2.2 Differential Surface Contraction Hypothesis (DSCH)

In 1976, Harris proposed his theory of Differential Surface Contraction Hypothesis (DSCH), based on the observation of infolding of epithelial rudiments during embryonic development (Karfunkel 1970, Baker 1965). DSCH assumes that cells are capable of exhibiting contraction on their edges, and these contractions are responsible for cell movements like sorting. It also assumes that the intensity of these contractions varies from one cell type to another. That is, the strength of these contractions is greatest for medium faces, is less for faces between two different cells (heterotypic), and is the least for ones between the same cells (homotypic). According to Harris, engulfment and sorting out behavior can be attributed to surface contraction as well as invagination. The more strongly one cell type contracts, the more it will sort out internally relative to other cell types.

2.2.3 Differential Interfacial Tension Hypothesis (DITH)

The most recently developed explanation for cell sorting was introduced by Brodland and Chen in 2000. The differential interfacial tension hypothesis (DITH), was essentially inspired by computational models designed to investigate cell-cell interactions. Their first results for sorting and tissue engulfment were unexpectedly in direct conflict with Steinberg's DAH; but, further analysis revealed the consistency of their model with respect to the behavior of

fluids in cell sorting and cell engulfment and DICH proposed by Harris. Furthermore, they could also provide reasonable explanations for the discrepancies previously observed between the DAH and the physics of surfaces (Brodland, Chen 2000a, Brodland 2002). Brodland's group based their method on the idea that all forces internally generated by a cell, and all tensions along the cell's edges, can be replaced by an element with appropriate nodal forces and an internal pressure acting normally to the edges, where the internal pressure was also assumed to be responsible for maintaining the cell volume (Chen, Brodland 2000).

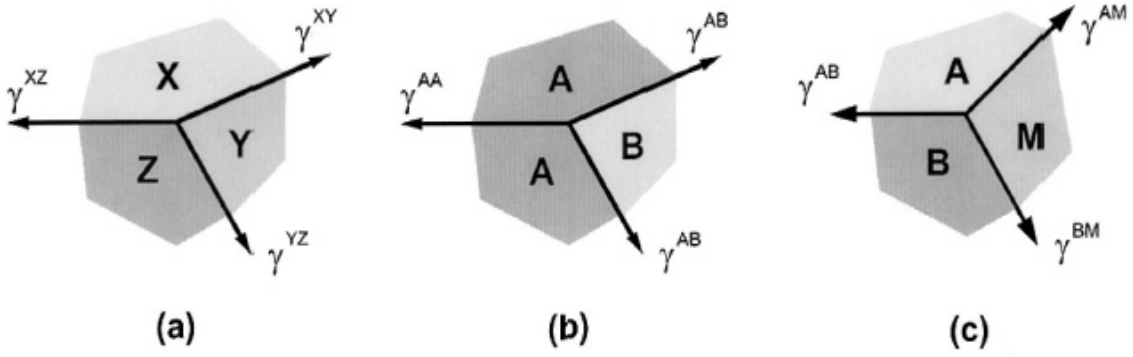

Figure 2-2 – a) A generic TJ with associated surface tension γ. b) An example of inside TJ and c) A TJ at the boundary of aggregate. (Brodland 2004).

According to the Brodland and Chen hypothesis, sorting can be explained by a TJ. Figure 2-2a shows a generic TJ along with interfacial vectors. The superscripts identify from which cells they are composed. In Figure 2-2b, a TJ of two cell types (A and B), is shown. The strength of tensions, and the angles the cells form, depend on the types of cells adjacent to the TJ. If the γ^{AA} is big enough, it can pull the TJ to the left which means that cell B is

getting in between type-A cells and the cells are mixing together. On the other hand, if the TJ moves toward the right, sorting will occur (Brodland 2002).

Today, this theory has become the *de facto* working hypothesis for cell-cell interactions (Lecuit, Lenne 2007, Rauzi, Lecuit 2009, Pilot, Lecuit 2005, Lecuit, Lenne et al. 2011). The goal of most current cell mechanics experiments and analysis techniques is to determine the effective interfacial tensions described by the DITH.

2.3 Important Role of Subcellular Forces

One of the fundamental questions in biology is "why do cells move and how are these movements regulated?" Cell rearrangements play an important role in many biological processes such as embryogenesis, cell sorting, wound healing, tissue engineering and cancer metastasis (Solon, Kaya-Copur et al. 2009, Kumar, Weaver 2009, Brodland, Chen et al. 2010, Varner, Voronov et al. 2010, Benko, Brodland 2007, Legant, Miller et al. 2010, Anon, Serra-Picamal et al. 2012, Martin 2010).

The morphogenetic processes through which an embryo takes on its distinctive shape is one of the most inspiring phenomena in nature. For almost half a century, a great deal of attention has been devoted to understanding embryonic cell movements and how they are regulated (Lewis 1947, Burnside, Jacobson 1968, Jacobson, Gordon 1976, Clausi, Brodland 1993). Among all steps occurring through embryogenesis, two morphogenetic processes have been the primary foci of research, namely: neurulation (Sausedo, Smith et al. 1997, Clausi, Brodland 1993, Brodland, Clausi 1995, Chen, Brodland 2008), and early heart tube

development (Ramasubramanian, Latacha et al. 2006). Both are seemingly simple processes, but have a high incidence of related birth defects in humans.

During the neurulation process a sheet of tissue rolls up to form a closed tube which later becomes the spinal cord and brain. Any abnormality in the movement of this sheet could result in neural tube defects, including spina bifida and anencephaly. The sequence of steps involved in neurulation is well known (Chen, Brodland 2008):

1. Genes and signaling pathways (Figure 2-3a) initiate and control the formation of proteins (Figure 2-3b; (Alberts, Bray et al. 2014).
2. Structural proteins begin interacting with one another, generating forces (Figure 2-3c) which produce cell-level reshaping or lamellipodium (Armstrong 1989, Keller, Davidson et al. 2000, Keller 2006).
3. Orchestrated cell-level reshaping leads to reshaping (Figure 2-3d) at the tissue level (Armstrong 1989, Clausi, Brodland 1993, Keller 2006, Veldhuis, Brodland et al. 2005).
4. Changes at the tissue level will cause morphogenetic movement at the embryo level (Burnside, Jacobson 1968, Brodland, Scott et al. 1996, Zamir, Czirók et al. 2005).
5. As a result of the previous steps, specific phenotypes are produced (Brun, Garson 1983), and various mechanical deformation feedback signals are generated between the genes (Stoltz, Wang 2002).

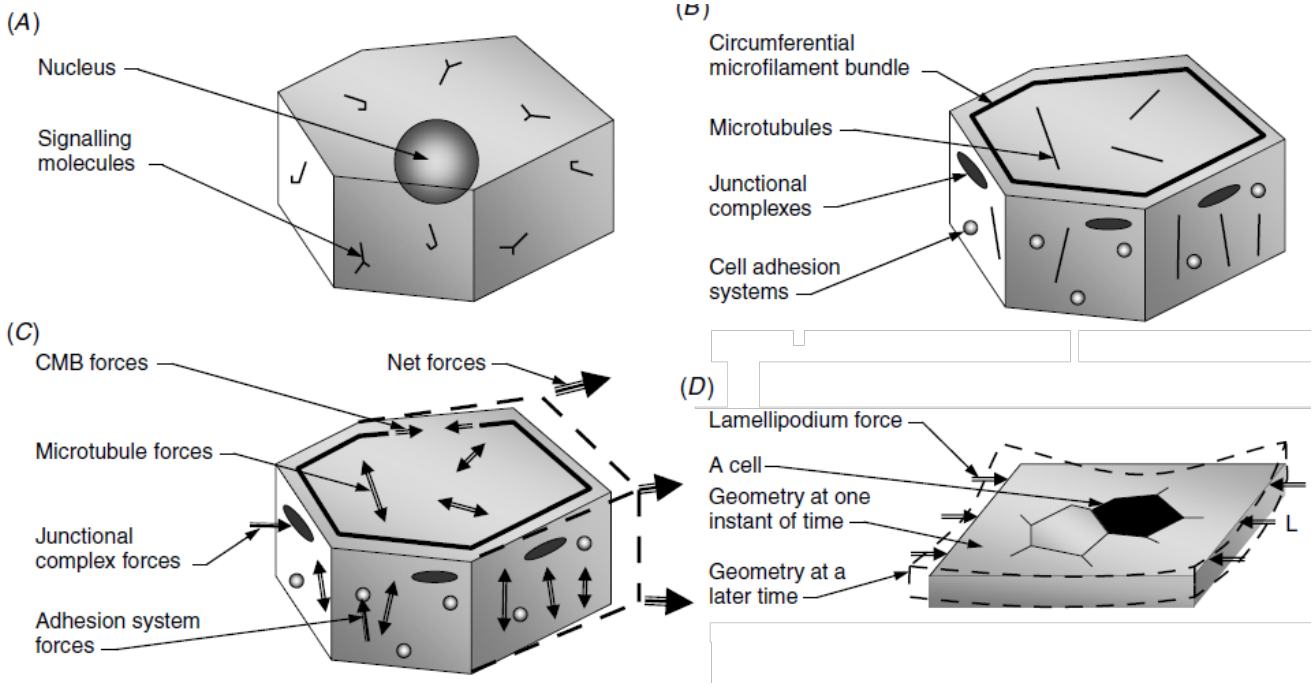

Figure 2-3 – Steps of neurulation (Chen, Brodland 2008).

Although more is now known about these processes from the biological side – for example, the role of gene expression in the development of cytoskeletal components – very little in known about the timing, location and strength of the driving forces. The big challenge to understanding these forces is the complexity of the 3D model (Ingber 2003, Brodland 2006) and obtaining driving forces and predicting the correct tissue deformations. Computational models have predicted that relatively small changes in the generated forces can significantly affect the resulting cell and tissue geometries and thereby affect the medical outcomes of the reshaping processes (Brodland 2004, Brodland, Chen et al. 2006). Thus, the forces are critical to the outcomes produced, and if a better particular outcomes is to be produced, the forces that produce them must be measured. A discussion follows of some of

these models, and what has been uncovered about the relationship between forces and the resulting geometries.

The invagination of sea urchin embryos has been studied as a process in which forces are known to play a key role. The process begins with a sheet of epithelial cells trying to bend inwards to form the archenteron. In order to simulate this process, it is necessary to consider both the mechanical properties of the epithelial sheet and the map of forces acting on each cell. In 2005, Davidson prepared a finite element model and tested five different hypothesized mechanisms. He showed that for each hypothesized set of driving forces, different cell shapes and invagination patterns resulted. Although his model could not calculate a unique set of cell-level forces, it showed that the motions produced are sensitive to details of the forces at work and that understanding the process would definitely require a known set of forces acting on the cells (Davidson, Koehl et al. 1995).

Cell sorting and tissue engulfment are two related phenomena which occur in heterotypic aggregates. Both have been topics of great research interest in the past few decades (Brodland 2003, Steinberg 1996, Armstrong 1989). The root cause of such cell behavior is the spontaneous cell rearrangement which occurs between different cell types. In order to describe these rearrangements various hypotheses have been published (Steinberg 1963, Brodland 2002, Harris 1976). However, as discussed in Section 2.2, none can provide a complete map of the forces working on the cells.

In cell sorting or tissue envelopment, a cell mass is assumed to start from an initial state and then undergo a sequence of incremental geometric changes. These changes will continue

until a final configuration is reached, after which no major changes occur. The cell-cell interactions within this process are understood to be driven by mechanical forces derived from the tensions in cell membranes. Any forward computational model would not be meaningful if it is not based on the true forces that drive cell-cell interactions. The availability of a trusted map of forces in action is necessary to accurately predict both cell- and tissue-level behaviors.

The majority of cancer fatalities are the result of metastasis, by which cancer cells migrate from their primary site to other organs. Thus, understanding the mechanisms that drive metastasis is one of the key goals of cancer research. However, despite the decades of work done in this area, metastasis is still poorly understood (Geiger, Peeper 2009, Shibue, Weinberg 2011, Baker, Lu et al. 2010). For instance, breast cancer is the most common cancer among women in North America and its cause is still unknown (American Cancer Society 2015). (Figure 2-4). A healthy mammary duct is made of two cell layers. The epithelium cells form the mammary duct and are responsible for secreting the milk. The outer layer is made of a different cell type, named: myoepithelium. These cells are a specialized combination of muscle and epithelial cells to contract and push the milk out of breast. Recent researches shows that in a benign breast cancer, the luminal cells are kept engulfed by the surrounding myoepithelial cells where those that metastasize malignant luminal cells spread out which leads to a 5-year survival rate of 25% [3]. The hypothesis is that mechanical interactions are the key to understand cell behaviors in both cases. The required forces to keep the cancer cells trapped inside (if known) could be associated to the structural

components of cells. This information would provide a framework for medical researches to make new drugs to avoid metastasis.

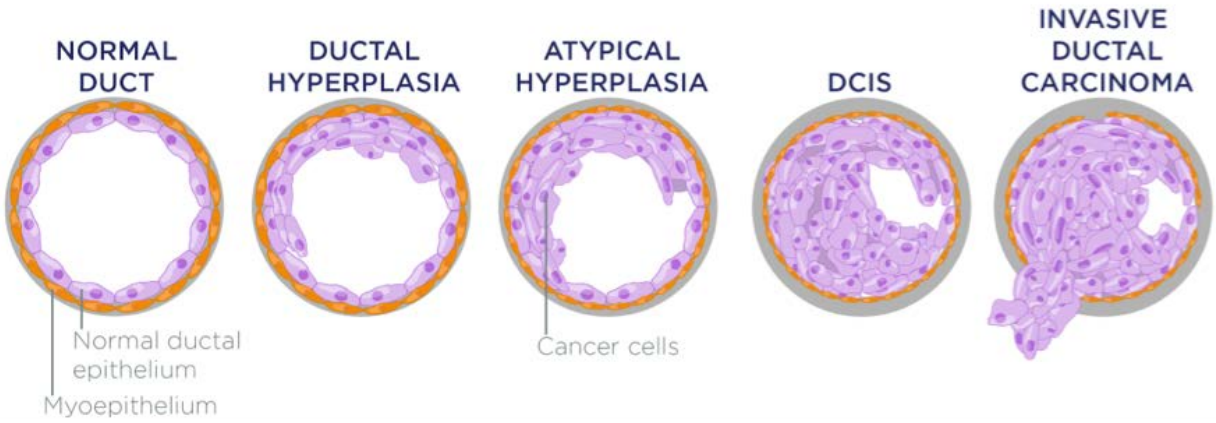

Figure 2-4 – Progression of breast cancer

Many factors have slowed progress towards understanding this important mechanism, including the variety of cancer types, the complexity of the metastatic process, and the fact that it occurs deep in the tissue where observation is very difficult, if not impossible (Marusyk, Polyak 2010, Said, Theodorescu 2009). Computational models of cell mechanics have provided key insights into the forces involved in the various steps of metastasis (Brodland, Veldhuis 2012), and are a promising avenue to developing a deeper understanding of metastatic processes.

2.4 Experimental Force Measurement Techniques

Throughout the last several decades, many researchers have tried to measure cell-level mechanical forces. However, it has proven to be an extremely challenging task. Part of the problem is that these forces are generated by various cell components, such as the

intracellular cytoskeleton, cell membrane and adhesion system. They are also in the range of 50-900 pN (Bausch, Moller et al. 1999), are subject to change with time (Martin, Kaschube et al. 2009), and location (Rauzi, Verant et al. 2008), and can be modulated by external stimulation (Lee, Scherr et al. 2007). Here, different approaches (Table 2-1) including AFM (Thomas, Burnham et al. 2013), LM (Hutson, Veldhuis et al. 2009), traction force technique (Micah, Wan 1999, Trepat, Wasserman et al. 2009), micropipette aspiration (Maitre, Berthoumieux et al. 2012), magnetic twisting cytometry (Kasza, Vader et al. 2011), optical tweezer (Borghi, Sorokina et al. 2012), and CellFIT (Brodland, Veldhuis et al. 2014) are briefly discussed.

Table 2-1 – Force measurement techniques

Technique	in vivo/ in vitro	Destructive	Information provided	Limitations
Atomic Force Microscopy	in vitro	Yes	Forces needed to deform or separate cells	Not applicable to interior cells.
Laser Microsurgery	in vitro	Yes	Edge forces in single cells, only	It is highly affected by far field stress.
Traction Force Microscopy	in vitro	No	Map of traction forces	Not applicable to interior cells.
Micropipette Aspiration	in vitro	No	Surface tensions of only one cell	Not applicable to interior cells.
Magnetic Twisting Cytometry	in vitro	No	Surface tension of only one cell	Affects cell properties. Not applicable to interior cells.
Optical Tweezers	in vitro	No	Surface tension of only one cell	Affects cell properties. Not applicable to interior cells.
CellFIT	in vivo	No	Spatial-temporal maps of edge tensions	Spatial and temporal images should have good quality.

Today, AFM (Thomas, Burnham et al. 2013) is a common method used to measure cell stiffness, and can also provide high resolution topography of the cell's surface. The AFM apparatus consists of a cantilever beam with a sharp tip. Once the tip is in contact with a sample surface, the contact force will bend the beam. According to the amount of deflection, the force can be obtained. Although this method can directly measure the tension in the membrane, it cannot be applied to the internal cells or cell-cell membranes. Cell ablation is another drawback of this approach.

LM (Hutson, Veldhuis et al. 2009) is another powerful method that can measure the membrane tension in embryonic epithelium. In this approach, a well-focused laser ablates a subcellular hole which makes the surrounding cells to recoil from the wound site. This displacement is observed over time. Then, a computational model uses this information to calculate the tensions in the cell membrane. The main disadvantages of this model is that it is only applicable to 2D tissues (monolayer), it is destructive and also the observed movements are highly sensitive to far field stresses.

The traction force method (Micah, Wan 1999, Trepat, Wasserman et al. 2009), is used to study motile cells adhered to the surface of a substrate. The idea behind using a thin elastic substrate for this purpose is rather simple; the cellular traction forces applied during locomotion cause the film to deform, which is highly visible and can be measured. This information, combined with the material properties of the substrate, can then be used to obtain the traction force of cells. However, the main disadvantage of this method is that it is not applicable to interior cells.

Micropipette aspiration (Maitre, Berthoumieux et al. 2012) attempts to measure the differential cell adhesion and face tensions between cells. The miniature pipette can keep cells from their natural movements or apply forces to them by producing negative pressure in the tube. Based on the number of cells drawn into the tube and the curvature of the membrane, the stiffness of the cell can be determined. It can also provide information to obtain edge tensions in cells. The main undesirable feature of this approach is that it can only be applied to surface cells.

Magnetic twisting cytometry is one of the newly developed methods to study cell micromechanics (Kasza, Vader et al. 2011). This method is based on twisting ligand-coated magnetic microbeads, which are attached to the proteins existing in the membrane, and measuring the resultant rotation with a magnetometer. The shear modulus, G can be easily obtained once the exerted force and measured rotation are available. The optical tweezer approach employs the same technique except that it uses a laser to move spherical beads inside the cytoplasm. Although both techniques are capable of measuring forces at the cell-level, they affect the structural properties of the cell by having the microbeads or beads inside the cytoplasm. It is also extremely difficult to apply them to a group of cells like an aggregate and control all of them simultaneously.

CellFIT is the only method capable of mapping interior forces in cells. Since it obtains its input data from confocal microscope images, it is non-destructive. CellFIT provides a map of tensions which can be extended through time as well. The single drawback of the method as it has been implemented to date, is that it only works with 2D models.

2.5 Computational Modelling Techniques

In order to understand force inference techniques, it is helpful to briefly consider the computational modeling techniques that gave rise to them. In the late 1970s, when computers became more powerful and widely available, biological scientists started using them to carry out their simulations (Gordon, Goel et al. 1972, Goel, Campbell et al. 1970, Honda 1978, Honda, Yamanaka et al. 1986, Chen, Brodland 2000). Some of the first simulations examined the mechanics of cell-cell interactions. Since then, models have become increasingly more complicated and accurate as computers have become faster and more powerful. Over the years, many models of cell-cell interactions such as cancer, embryo morphogenesis, engulfment, cell sorting and dissociation (Andasari, Roper et al. 2012, Brodland, Chen 2000b, Chen, Brodland 2000, Clausi, Brodland 1993), have been studied by means of computerized models. The massive calculation power of today's modern computers provides scientists with powerful research tools and has opened new horizons, especially in the medical field. Here, some of the cell-cell interaction models developed over the last several decades are presented.

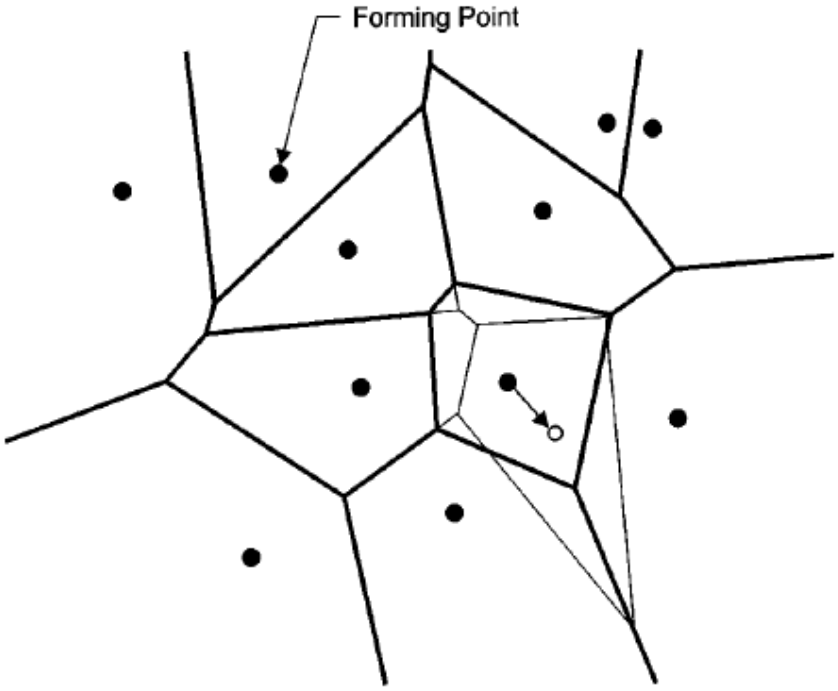

Figure 2-5 – Cell-centric model in 2D – the dark lines represent the initial geometry, whereas the light lines represent the altered geometry as a result of moving one forming point (Brodland 2004).

Figure 2-5 presents a model created using the Voronoi tessellation technique, an approach which starts with a required forming point (Tanemura, Ogawa et al. 1983, Tanemura 1988). In this technique, the cell boundaries and the shape of the mesh are directly related to the locations and the spacing of the points (Bodenstein 1986, Honda 1978, Umeda, Inouye 2004). The cell boundaries are formed with perpendicular bisectors to the lines joining the forming points. As a result, each cell is formed as a polygonal convex entity. Therefore, moving a forming point will alter all of the outlines corresponding to that point.

The cell-centric model is one of the first models developed to investigate cell-cell interactions. The Voronoi tessellation technique is used to generate the initial mesh. Once the

mesh is prepared (Figure 2-5), an algorithm starts to move the forming point around to find the largest drop in free energy as a function of the shape rearrangements and energy dissipation caused by the cell's viscous fluid (Honda 1983, Honda, Yamanaka et al. 1986). The process is repeated over each time increment until the system reaches equilibrium.

The main advantage of a cell-centric model is the ability of the mesh to form shapes that are more cell-like in nature (Honda, Yamanaka et al. 1986). One of the drawbacks of this model is the limited range of cell shapes that can be created; they must follow the rules defined by the Voronoi tessellation method because that is how the geometries are generated in each time step (Honda 1983, Tanemura, Ogawa et al. 1983, Tanemura 1988).

The cell-centric approach was also pursued in 3D (Palsson 2001). In this model, each cell was represented by a constant-volume ellipsoid whose properties could be cell specific. The model also allows cell movement and locomotion within the system. Each cell receives an internal stiffness value based on its ellipsoid dimension. In order to mimic the viscoelastic effects of the cytoplasm, a combination of springs and dashpots are used. The force exerted between the cells depends on the proximity of the cells to one another and their relative axes orientation (Figure 2-6a&b).

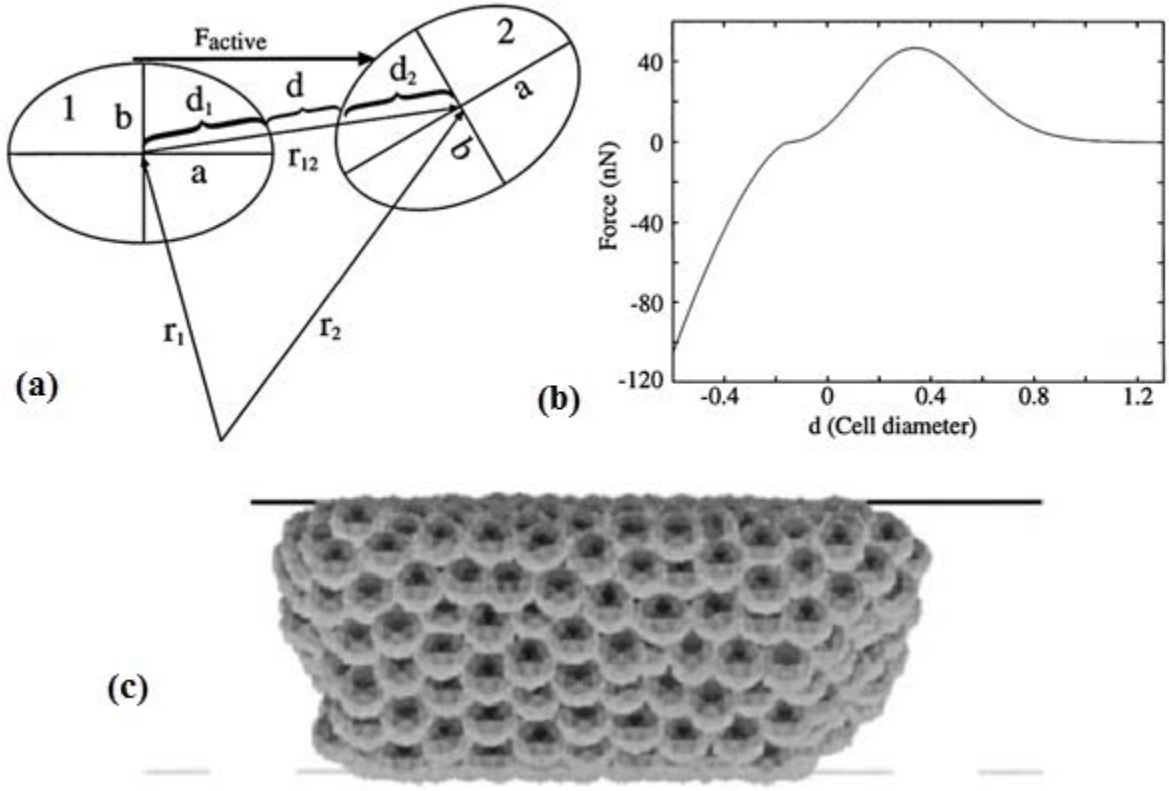

Figure 2-6 – Cell-centric model in 3D shows (a) how the distance d between two cells are calculated, and (b) how the forces acting on the cell depend on the distance d. (c) the approach could model an aggregate squeezed between two compressive plates. The forceF_{active}, is the active force that the cell applies (Palsson 2001).

Using this model, Palsson could simulate the squeezing of aggregates between two compressive plates (Figure 2-6c) as well as the cell sorting behavior of various cell types within an aggregate. The advantage of Palsson's model is the ability to include the motion of individual cells. However, the calculated stiffness and forces may not represent the physical system precisely. Another difference is that cells are allowed to have gaps which does not match with biological systems where cells completely fill the space.

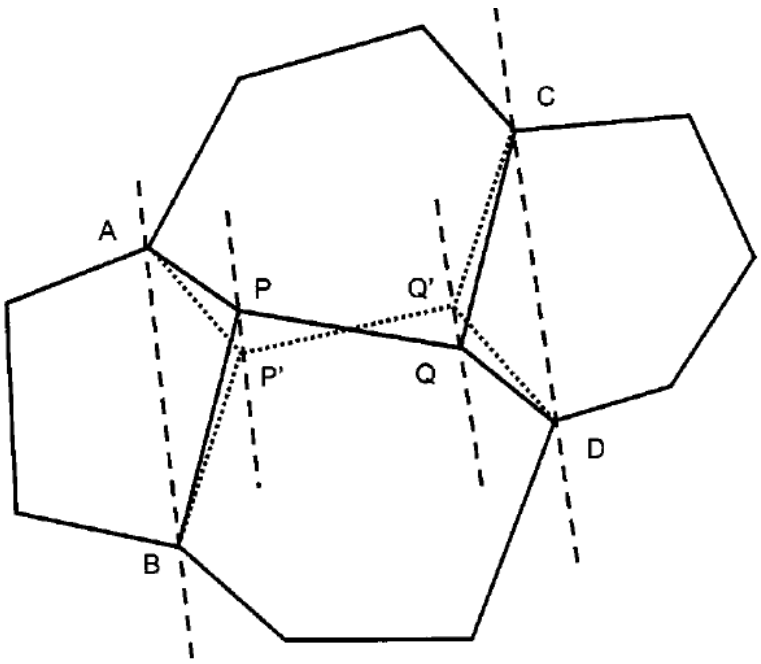

Figure 2-7 – Boundary vertex model in 2D. The space of a cell is defined based on the location of the vertices and edges connecting them. An edge can be adjusted by moving its forming points which in turn affect all four other connected edges (Brodland 2004).

Another approach that allows the cells to take a general polygonal shape and removes the restrictions of the cell-centric method is the boundary vertex model. In this model, the polygons are created by the vertices located by the spatial coordinate (Figure 2-7). Two versions of this method have been reported: a boundary-shortening version, in which the objective is to minimize the total boundary length, and a weighted boundary-shortening version that uses a weighting variable to find the minimum boundary length. The process starts with choosing an edge and adjusting its forming points to find the minimum boundary length. In the case of weighted system, each length is multiplied by its variable (weights) before the total boundary length is calculated. The process continues until the system reaches a minimum boundary length. This model was able to mimic behavior of the cell sheets. However, the main drawback was the inability to take viscous forces into account.

The boundary vertex model was developed from the understanding that a system of cells driven by interfacial tensions wants to minimize its free energy. Such a model was first formulated and introduced by (Fuchizaki, Kusaba et al. 1995), who had the experience of studying the grain growth of metals. In this model, cells are formed by polygonal faces. To allow the faces to have non-planar deformation, each face includes a center node (Figure 2-8b). Deformations occur by means of surface tensions. In the cases where an edge shrinks to a minimum specified length, the model can allow the cells to either join or separate by deleting or relocating certain nodes and edges (Figure 2-8a). This feature allows the cells to relocate within the aggregate (Yang, Brodland 2009).

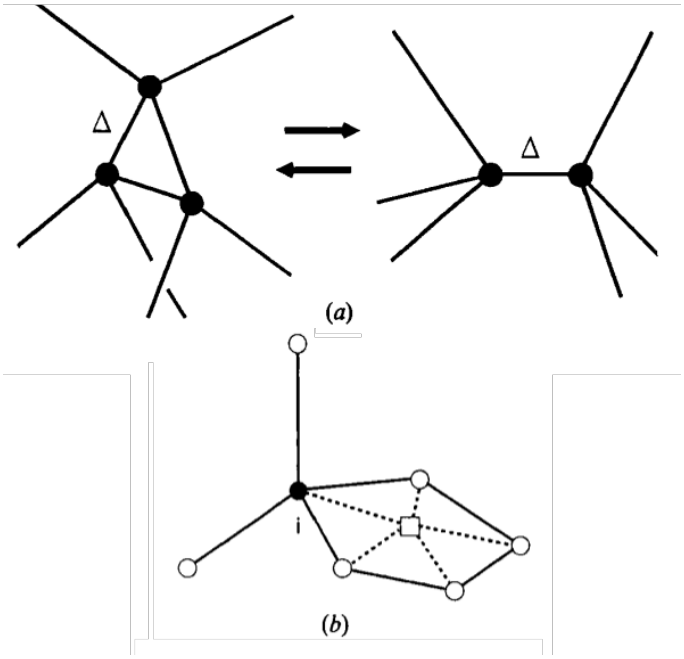

Figure 2-8 – Details of the boundary vertex model in 3D. (a) Neighbor changing process in which the system loses a triangular face. (b) A point denoted by a square is provided on the face; these are also considered as vertices upon triangulation (Fuchizaki, Kusaba et al. 1995).

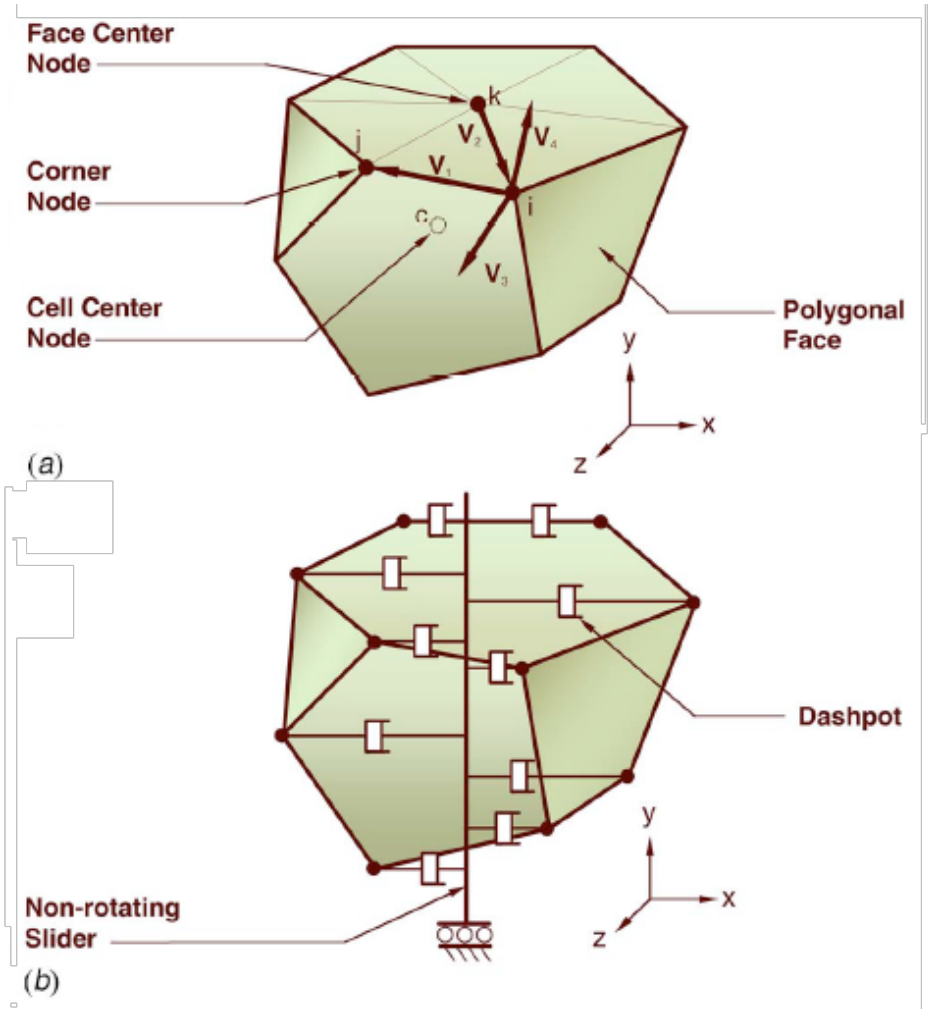

Figure 2-9 – The Cell3D model structure. (a) Node k is used in volume and stiffness calculations. It also allows the faces to take a non-planar shape. (b) Dash-pots and slider representing the cell viscosity.

In addition to the ability of cells to move and relocate within a 3D aggregate, the boundary vertex model also better represents the face behavior by adding an extra node to the face vertices. This extra node allows the faces to take curved shapes during the analysis. The main drawback though is that the system can remain stuck in a local minimum energy condition rather than finding the global minimum. The model also does not include the viscous effects or stiffness of the intracellular matrix.

Perhaps the most comprehensive model is the Cell3D model (Figure 2-9a). This model (Viens, Brodland 2007) uses a forward finite element technique to run a patch of cells. A constant tension γ is assumed to act along each cell-cell interface, and it is the primary driving force for cell motions. However, the cells are assumed to keep a constant volume which might not be true for all cases as water can migrate in and out of cell membranes (Alberts, Bray et al. 1998).

Since the strain rates experienced by real cells are modest, the cytoplasm can be considered to behave as a viscous fluid (Clausi, Brodland 1993). Therefore, each cell can be considered to have a constant viscosity of μ and modeled using a system of orthogonal dashpots (Figure 2-9b). From the computational perspective, this assumption can substantially decrease the run time, and from a physical perspective means that the residual stress can be ignored in cytoplasm. The model also allows neighbor changing in the same manner as the boundary vertex model. An example of the neighbor changing is shown in Figure 2-8.

2.6 Force Inference Techniques

The models described in the previous section showed that forces and geometries are intimately linked, and raised the possibility of inferring forces from detailed shape and motion information. The result was a series of approaches for inferring forces from cell shape. Another motivating factor was the recognition of the considerable limitations of available force measuring techniques. Force inference offers the prospect of a non-invasive approach with the power to provide detailed maps of the forces at work.

The first such technique was VFM, which showed that it was possible to calculate the forces acting on an embryo of *Drosophila melanogaster* from time-lapse images (Brodland, Conte et al. 2010). Like the computational models that inspired it, VFM divides the forces into two separate groups: active forces generated by intracellular subsystems of cells (e.g., action-myosin contraction), and passive forces arising from the mechanical properties of the cell structure (e.g., viscous cytoplasm). The VFM method assumes that the active forces act along cell boundaries and that passive internal forces dissipate energy. The computational model is created from the time lapse images and the deformation is measured from one image to the next. Then, a system of equations is assembled to find the forces that can make such deformations happen. The approach was validated through a series of runs performed on synthetic data where the result of VFM was compared against the synthetic model. The validation process starts by running a 2D model in which a specified set of forces act on each edges. Then, the displacement associated with each step are provided to the VFM code. Although the VFM technique was informative and could provide a map of the forces in a 2D aggregate but it was sensitive to noise.

VFM was used to calculate the edge forces acting in the embryo during ventral furrow invagination in *Drosophila melanogaster* based on time-lapse images (Brodland, Conte et al. 2010). This analysis showed that apical constriction and apical-basal shortening forces in the mesoderm are mainly driving the ventral furrow formation. More importantly, it also revealed valuable information about the shape of the forces acting on membranes. The apical forces are found to change almost in a parabolic fashion where the basal forces are observed to be more constant with time and position. A 2D *in silico* model is used in VFM to provide

the embryo's cross-section. The material properties and the shape of the cross section have formed in way to match the real embryo's cross-section. The observed deformations were used as input for VFM model and then it solves for a set of edge forces that could produce those information (Brodland, Conte et al. 2010). Techniques such as VFM are categorized as inverse models because they solve for driving forces (cause) where other properties such as materials and boundary conditions (effects), are assumed to be known.

CellFIT is another force inference approach done in 2D. The insight that led to its development was the realization that if edges were allowed to curve (caused by inside pressures or active intercellular forces), then the governing equation for each TJ can be simplified into an equation relating edge tensions and the limiting angles at which they approach the junction. These equations together set up a system of equations which is generally overdetermined. Solving these equations with a least square solver produces a map of relative edge tensions, that is, a self-consistent set of tensions whose scaling can only be determined with the aid of experimental force data. In cases where the pressure is of interest, Laplace equations can be constructed and solved for each cell boundary (Brodland, Veldhuis et al. 2014).

The advantages of this method are the clarity and robustness of the constructed equations, uniqueness of the obtained solution and insensitivity to noise. The main drawback is that this technique is limited to cell-sheet models.

Another approach which looks for the shape of the cells and their junctions with their neighbors was recently published by Ishihara in 2013. In this method, he tries to find the

tensions and pressures via a Bayesian solver (Ishihara, Sugimura et al. 2013). His main goal is to find the unknowns by only looking at the angles that the faces and edges make. Three different scenarios were applied to two different synthetic models of cell aggregates. The first scenario considered all cell pressures to be equal and constant and solved for tensions. The second scenario assumed tensions to be equal and calculated the inside pressures. And the last scenario tried to find tensions and pressures simultaneously. Both scenarios were validated with the synthetic models and the authors also compared their results against previously published biological data information.

Both Ishihara's method and this thesis are examining the angles that faces are making at junctions, but where Ishihara's approach assumes that the cell edges are straight, CellFIT allows them to be curved. This seemingly subtle difference strongly impacts the equations produced and the effectiveness of the technique (Brodland, Veldhuis et al. 2014). Also, Ishihara's approach only considered 2D cases like *Drosophila* epithelial cells where cells form a one layer sheet and is not applicable to 3D data.

In spite of the considerable advances in modeling techniques achieved in recent years, there remains a gap in finding an approach which can work with 3D data. In the present thesis, a solution to this problem is proposed which expands the 2D CellFIT approach to the 3D scope and applies it to both biological and synthetic models. The methodology and results will be discussed in Chapter 3 and Chapter 4 respectively.

Chapter 3
A New 3D Approach

Extending the successful 2D force inference methods outlined in the previous chapter to 3D is not a trivial problem, largely because it is difficult to determine the contact angles in 3D. In this chapter, a collection of software tools is presented that, when used together, make 3D force inference in cells possible. Figure 3-1 illustrates the steps taken in this process.

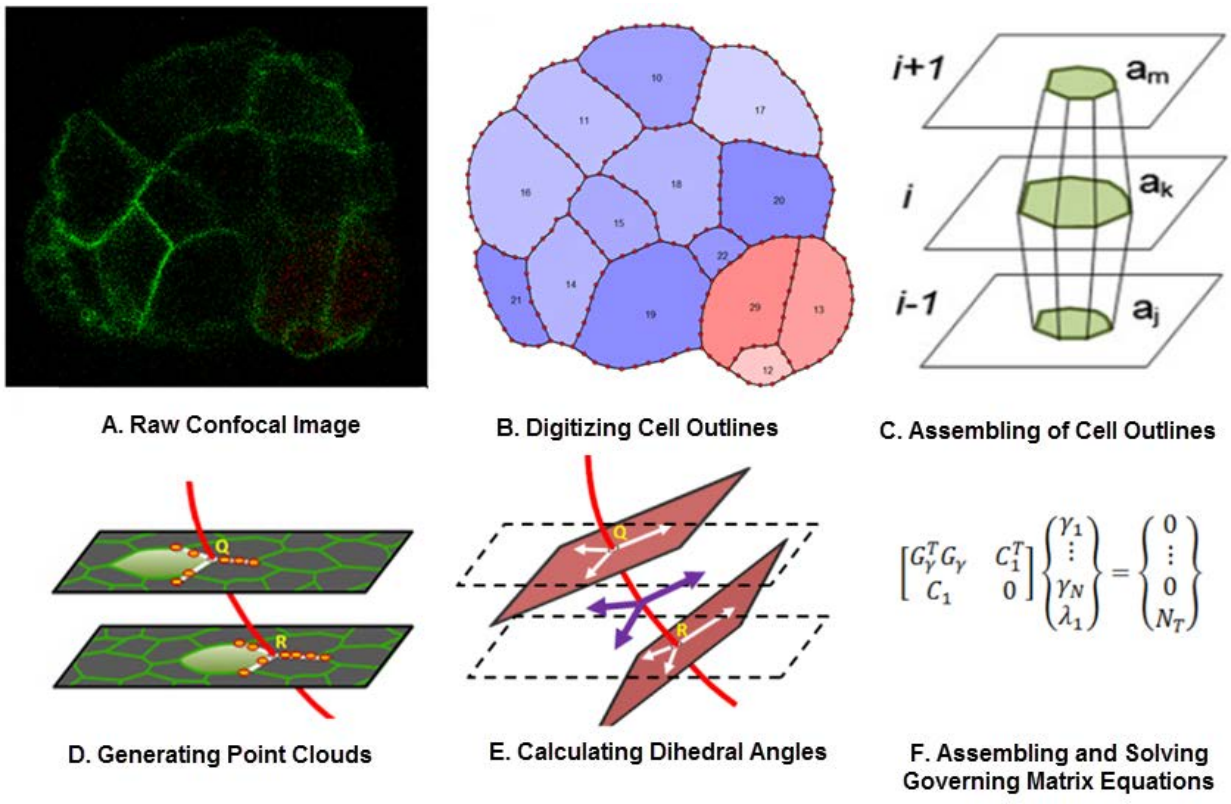

Figure 3-1 – Steps in our 3D approach.

The proposed approach comprises the following steps:

A. A spatial stack corresponding to a particular time is chosen from an image stack.

B. The stack is digitized by the toolbox (Figure 2-1B) developed by the author which makes it possible to trace the edges of the cells in the stack images. The digitizing toolbox and its corresponding algorithms are discussed in Section 3.1

C. Once the stack images are all digitized, the outlines associated with each cell in the stack are collected together. This process is called grouping (Figure 3-1C). In Section 3.2 we discuss a crucial difference between 2D and 3D, namely why a vertex-based approach like that used in CellFIT-2D will not work in 3D.

D. Next, a Point Cloud Model (PCM) is developed for each cell-cell and cell-medium interface (Figure 3-1D). This process will be discussed in detail in Section 3.3.

E. Once the PCM is constructed, we calculate the contact angles along the curves where each set of three cells contact each other, or two cells contact the medium (Figure 3-1E).

F. Finally, with dihedral angles available, the system of equations for each edge is assembled and is solved with least square method (Figure 3-1F).

3.1 Building a Model from 2D Sections

Figure 3-2 shows a set of confocal images that can be used to construct a 3D model. The basic steps involve tracking the outlines of individual cells by computational or manual means, grouping these outlines into sets for each cell, and generating point clouds for each

cell-cell or cell-medium interface. As the image suggests, the digitizing watershed toolbox used to segment the cells works best when the images are multi-channel so that there is information for distinguishing different types of cells in the cell aggregate. Figure 3-3 shows the home screen of the digitizing toolbox developed by the author using Matlab.

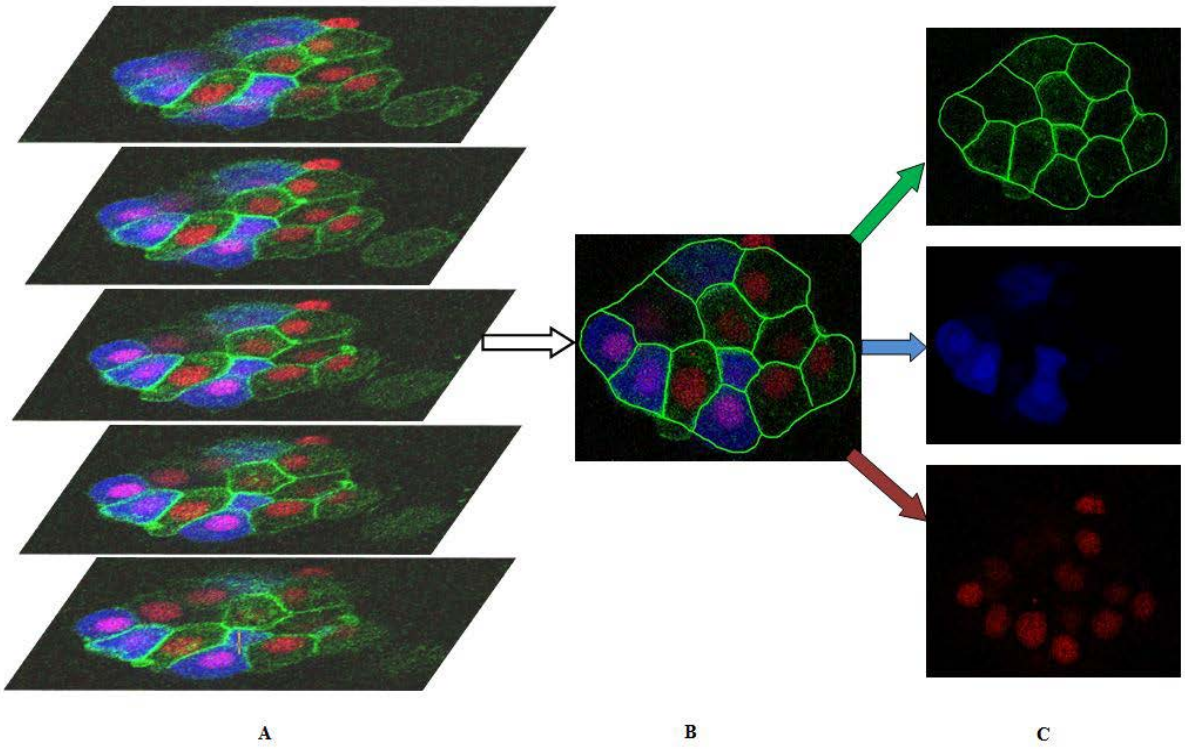

Figure 3-2 – (A) Image stack of one time step. (B) Green channel is brightened by the customized toolbox. (C) Blue channels show which cells have a different type from the rest and Red channels show the cell nuclei which confirms the presence of a cell.

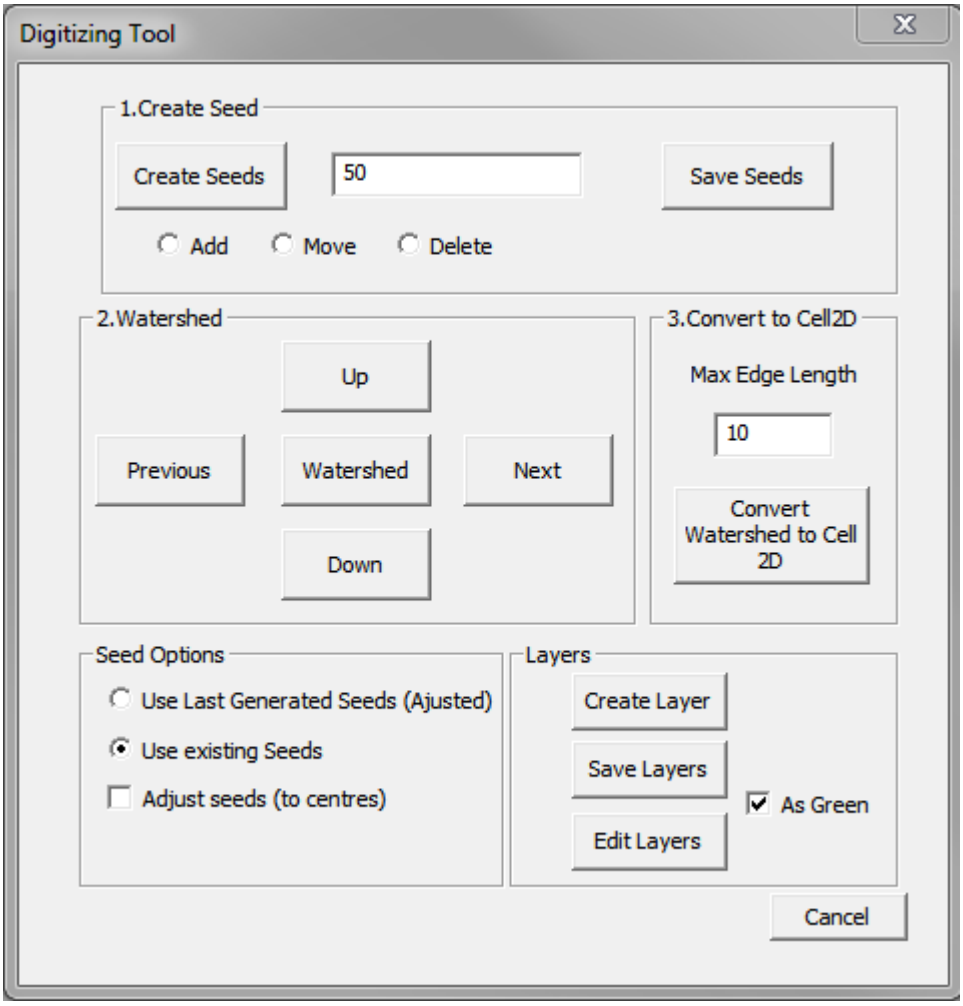

Figure 3-3 – Digitizing watershed toolbox home screen. This toolbox makes it possible to automatically generate seeds, perform watershed algorithms and do any modification necessary. It also uses the information from the last spatial image to more accurately locate the seeds for the next image.

Image segmentation, to produce individual cell outlines, can be accomplished using a "watershed by flooding" algorithm (Beucher, Meyer 1992). The toolbox allows an intensity image (Figure 3-4a) to be replaced with an associated topological map where the intensity level of a pixel is interpreted as its altitude (Figure 3-4b). Each cell, then, produces a basin-shaped form.

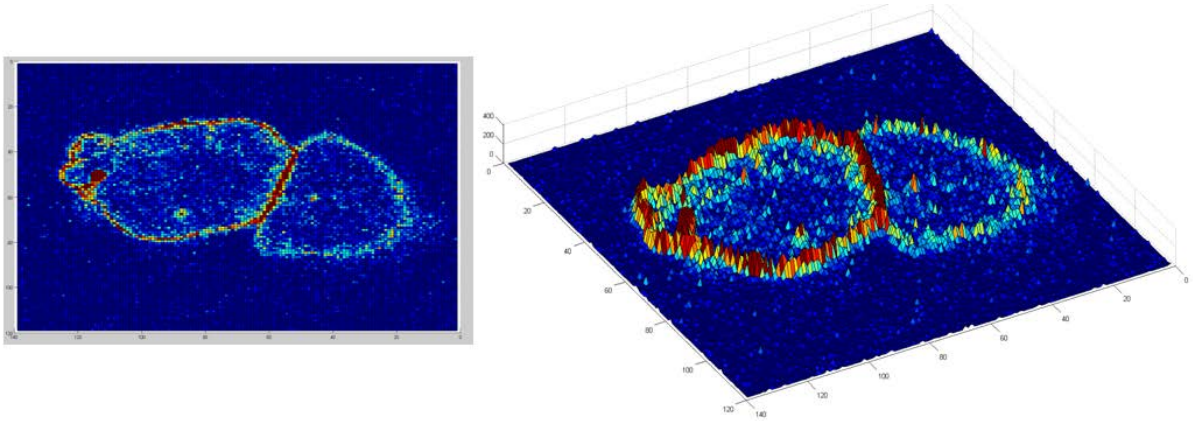

Figure 3-4 – Producing a grey scale image in 3D is the key to understanding the watershed algorithm. In 3D each cell looks like a basin where white pixels located on cell outlines have high value (shown as hot color), and the inside dark pixels have low value (blue).

The software then finds a local minimum and defines it as a seed, and gives these starting pixels a unique ID (label). It then begins to flood the area from that point. The partitioning process involves flooding all basins beginning from the seed at the bottom of each basin and ends when all such water bodies touch each other. The result is an image in which all of the pixels belonging to a particular cell have a uniform and unique label. The detailed steps in the overall process are:

1. Assign a set of seeds from which the flooding happens. A label with a unique number is assigned to each such pixel.
2. The water source and its neighboring pixels are inserted into a priority queue based on the gray level of the pixel. Any new pixel (i.e., non-labeled pixel), inserted into the queue gets the same label as its already-assigned neighbor.
3. The pixel with the highest grey value (i.e., lowest pixel value), is extracted from the queue and its non-labeled neighbors are inserted into the queue.
4. Step 3 is repeated until the priority queue is empty.

These steps are also shown in flowchart format (Figure 3-5) to better illustrate the Watershed procedure.

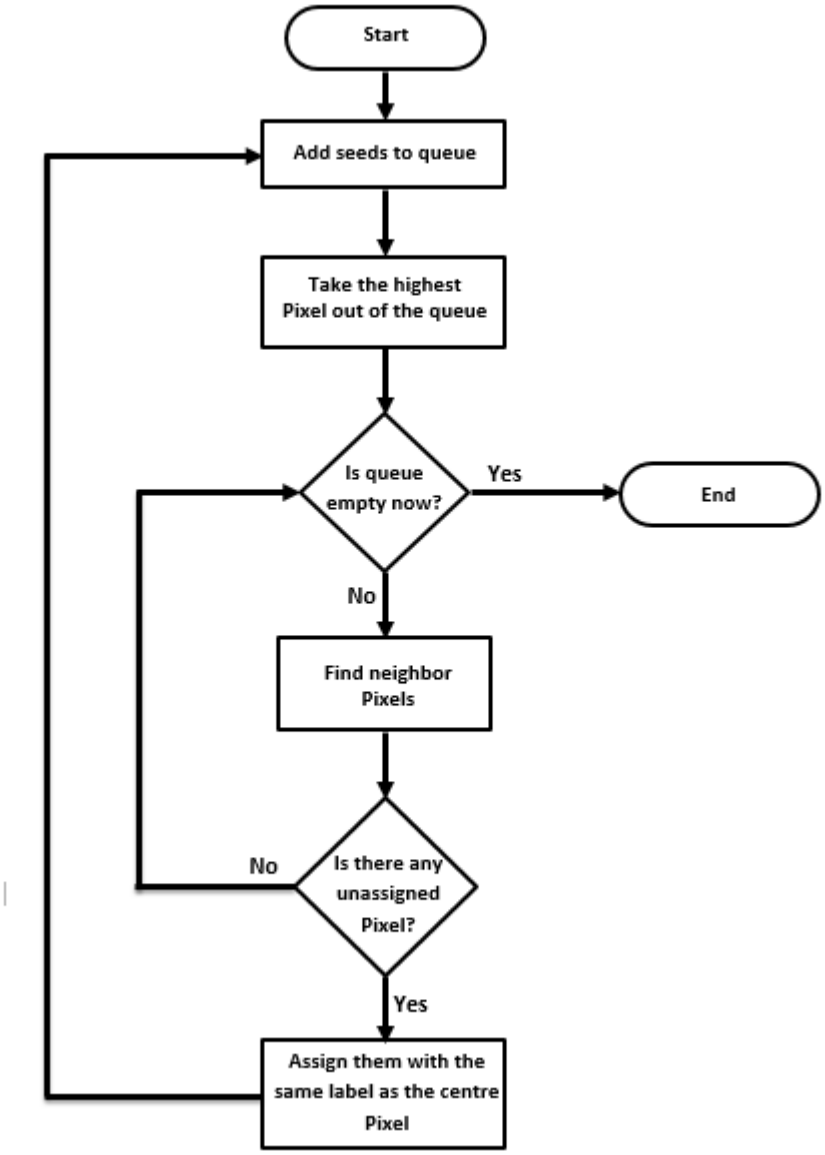

Figure 3-5 – Watershed core process in flowchart format.

Given the number of images, mistakes can be made if the user must manually choose the starting position for water sources. To reduce the user input error, the author improved the

code by adding one step preceding the watershed algorithm which automatically loads the consecutive images in stack and assigns water sources to them. Figure 3-6 shows the flowchart for the automated process of digitizing image stacks.

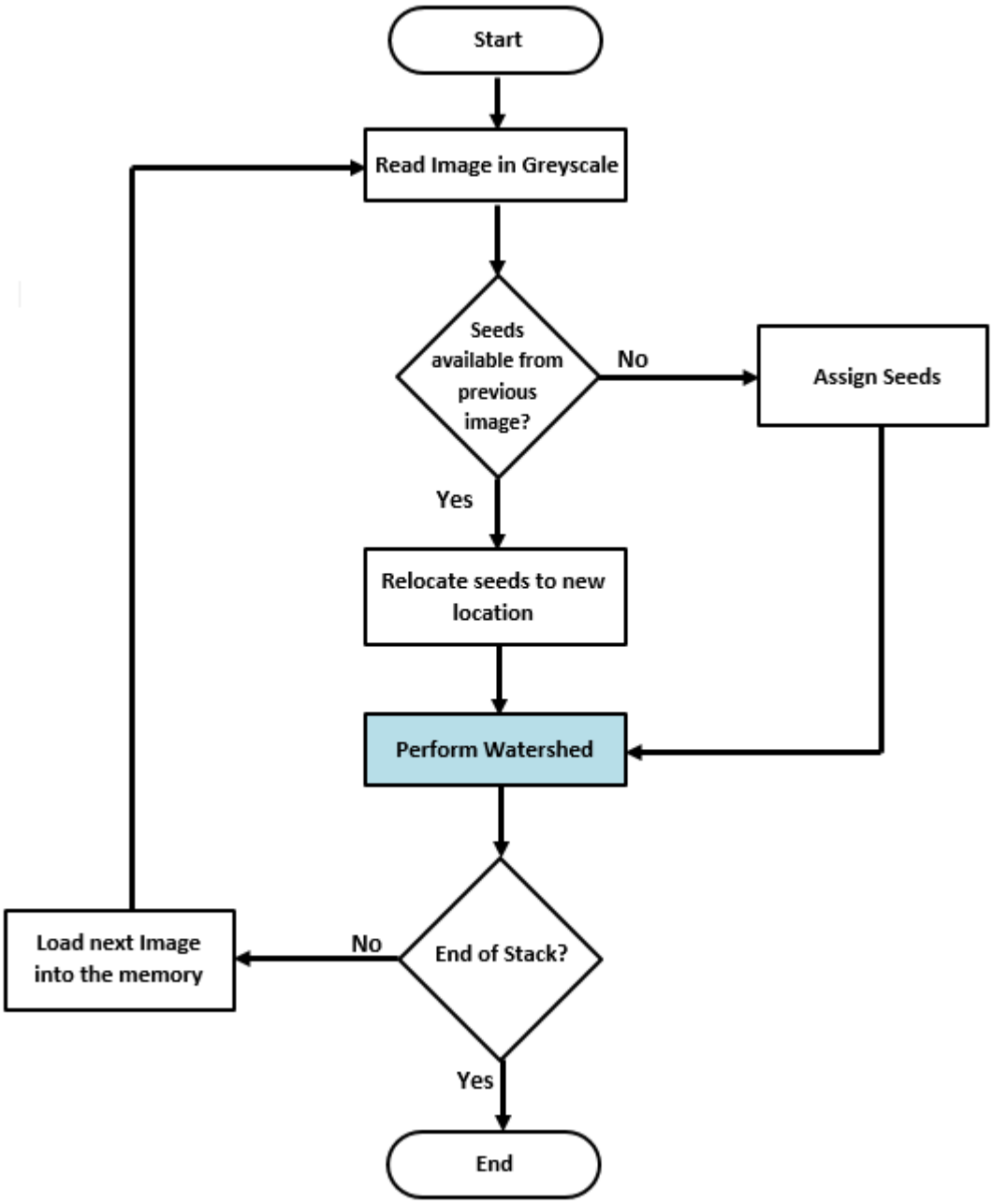

Figure 3-6 – Automated Watershed Algorithm. The blue rectangular shows the step in which Watershed's core process takes place.

For the watershed process to capture a cell and its boundaries, there should be one, and only one, seed inside each cell region. To assign only one seed to a cell, the local minima (darkest pixel within that cell) is calculated by applying a two consecutive median filters with windows of 7 and 5 pixels respectively, to smooth out the pixel values and assuring that only one minimum exists within each cell boundary. Frequently, for noisy data sets such as medical images, there is more than one minimum in some cells which leads to an over-segmented result and requires a second step of region merging process. Here, median filters are used beforehand to avoid the extra step. The smoothing process is carried out on a copy of the original image so that the original is retained for subsequent steps.

The results of the watershed process (Figure 3-7-B) are saved in an 8-bit grey-scale image. Images of this sort are composed exclusively of shades of grey varying from 0 (representing black), to 2^8-1 (representing white). The values of each pixel show the intensity of the white color. Therefore, the watershed algorithm can distinguish 127 cells (including the medium as a cell), in every 2D image. The coding then saves the results in a new image in which all pixels within each cell's area have a unique value (Figure 3-7-C). This new image contains all of the geometric information of the cells in the specific level where the image was taken.

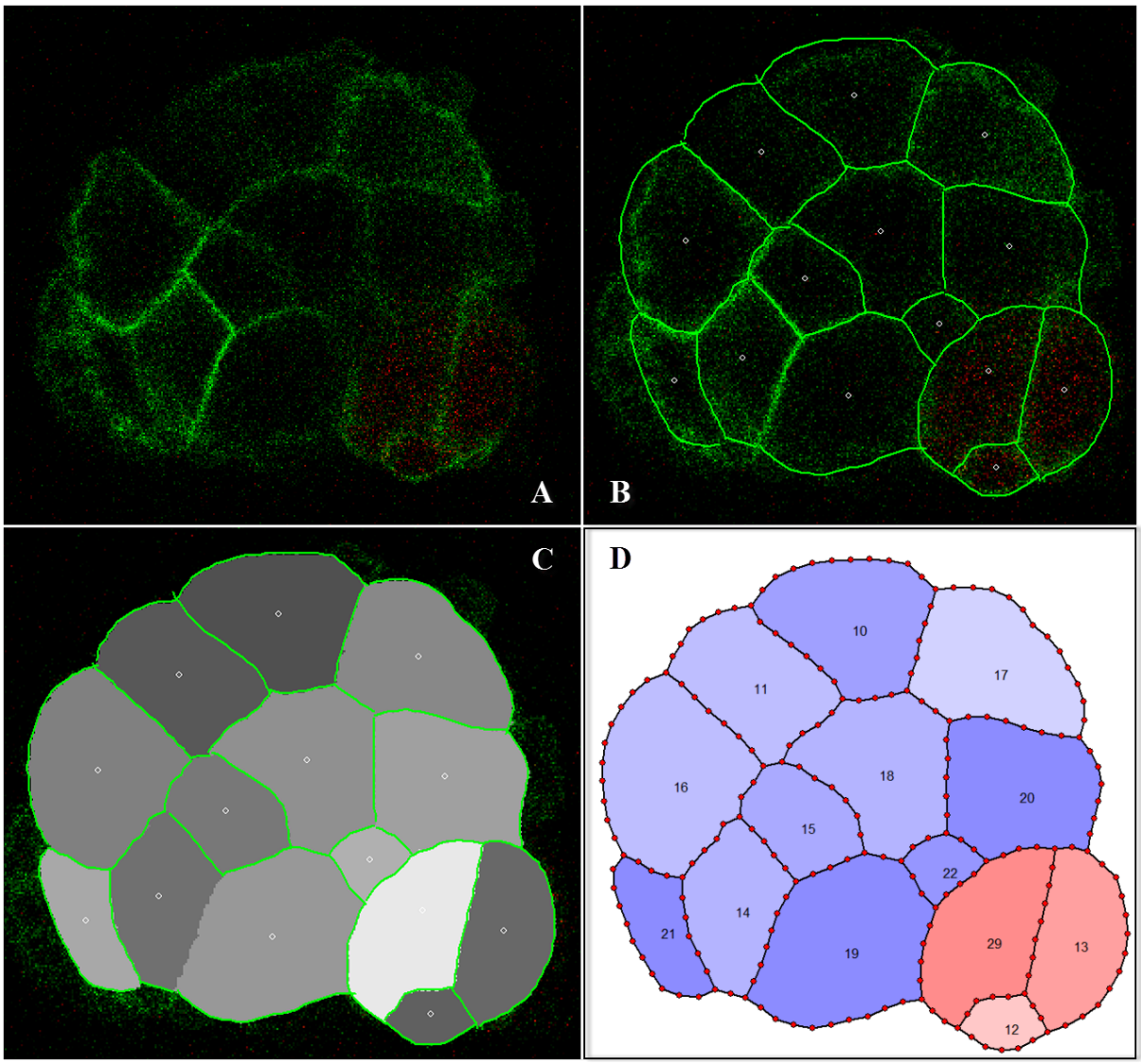

Figure 3-7 – Digitizing procedure. (A) Raw image. (B) Outlines enhanced and seeds placed within each cell. (C) Watershed algorithm assigns the value of the seed to a pixel inside a cell. (D) Watershed result is converted into Cell2D model.

Once the results of the watershed process are obtained (Figure 3-7-C), another process in the software begins scanning the image. A 2 by 2 pixel-wide scanning window is used to distinguish the pixels associated with edges and TJs (Figure 3-8). Based on the number of different values seen in the scanning window, the program determines if it has hit an edge, a

TJ or a quad junction (QJ). For instance, Figure 3-8-C shows the scanning window hitting the TJ between cells 10, 17 and the medium.

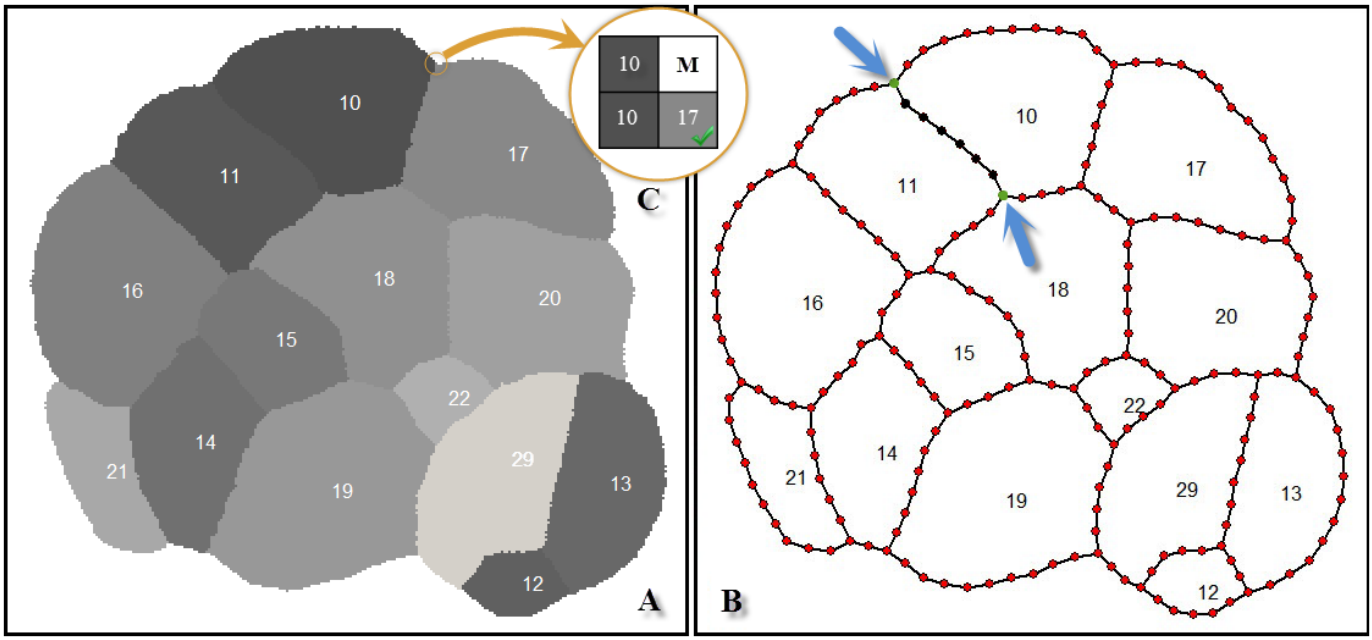

Figure 3-8 – Converting watershed to Cell2D models (A) Watershed result. (B) Cell2D model. The dots along each edge will later help to construct 3D faces and edges. (C) With three different values in the scanning window, it shows that this point is a TJ. This point will later be added to the 3D edge in common between cells 10, 17 and the medium.

In general, one of four cases will be seen in the 2x2 window, based on the number of different pixel values displayed. In the first case, only one number is seen which means the window is completely inside a cell and all four pixels have the same value. The program is set to take no action for this case and move the window to the next set of pixels. The cases with two and three pixels seen in the scanning window correspond to an edge and TJ, respectively. In general, edges and TJs are distinguishable from their neighbor cells: a TJ has

three neighboring cells whereas an edge has only two. Once the scanning window hits a TJ or edge, its location is added to the proper group based on the values in the scanning window. The case with four different pixel values corresponds to a QJ. To simplify the equations used in this research, each QJ is converted into two TJs (Figure 3-9). Therefore, there remain only two cases of interest: hitting an edge or a TJ.

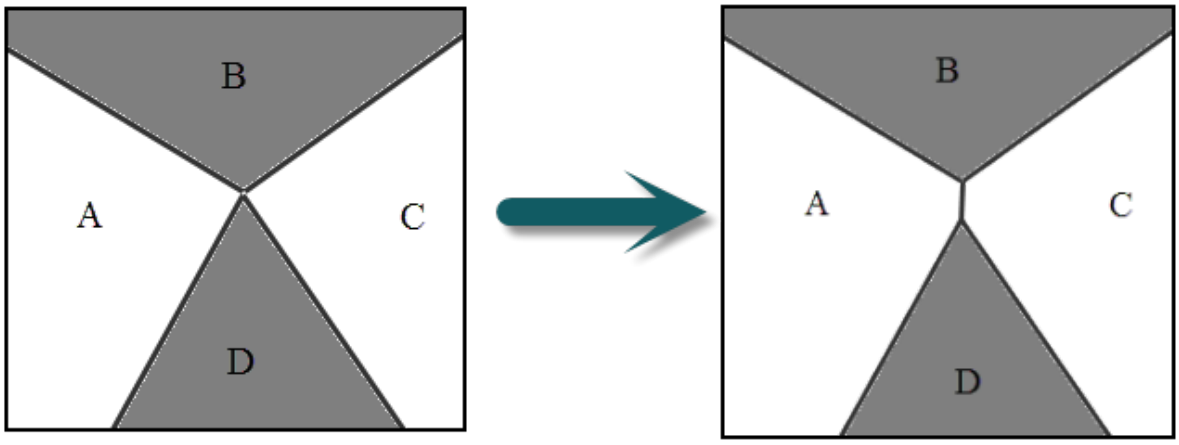

Figure 3-9 – Dividing a QJ into two TJs by adding a small edge in between cells.

A spline of the order of three is then fit to the collected pixels of each edge to create a smooth edge over the obtained pixels. Then, based on the user input spacing and the total length of the edge, mid-points are generated along the created B-spline (red dots in Figure 3-8-B).

In practice, for the end users, it appears that the four steps occur in two separate phases: first, locating the seeds so that each cell has one and only one seed inside, and second, generating the watershed which performs steps 2 to 4 (Figure 3-7 B & C).

3.2 Why Not Track Vertices?

The initial plan for calculating the cellular forces in 3D was to extend the VFM approach so that it could be applied to 3D aggregates. VFM has been able to successfully calculate the membrane forces on 2D aggregates (Section 2.5), and its results have been shown to be compatible with previously reported face tensions, making it a good starting point for this thesis. To extend the VFM, it is first necessary to construct a 3D model which includes all vertices, edges, faces and cells for each time step of an image stack. Then, assuming all generated models are geometrically consistent (same vertices, edges, etc.), the displacement matrix could be obtained for any two consecutive time steps. Finally, with the displacement matrix and cell properties available, an inverse finite element solver would be able to calculate the unique map of forces acting along the membranes. Note that the vertices referred to here (Figure 3-10), are different from the TJ introduced in the previous sections. A TJ is a point along a 3D edge (not necessarily the end points of the edge), which is obtained from a 2D image. The TJ is always in contact with three neighboring cells (considering the medium as a cell for TJs on the boundary), whereas a vertex is a corner (the end nodes of the 3D edge), always touching four neighboring cells.

The software toolbox designed by the author boosted the speed of the digitizing process and made it possible to digitize a full stack including several hundreds of images. Auto-generated TJs and points of edges (i.e., 2D points of digitized images), were then assigned to corresponding faces and edges. Looking at Figure 3-10, it is obvious that the cut planes do not necessarily pass through the points of interest (3D vertices). An interpolation technique might be used to locate these vertices. However, our preliminary result assured that it would

be fairly inaccurate specially when working with biological data. . In addition, small edges with their end points located between two consecutive cut planes will not appear in the 2D sections; this can also happen for long edges parallel to the planes.

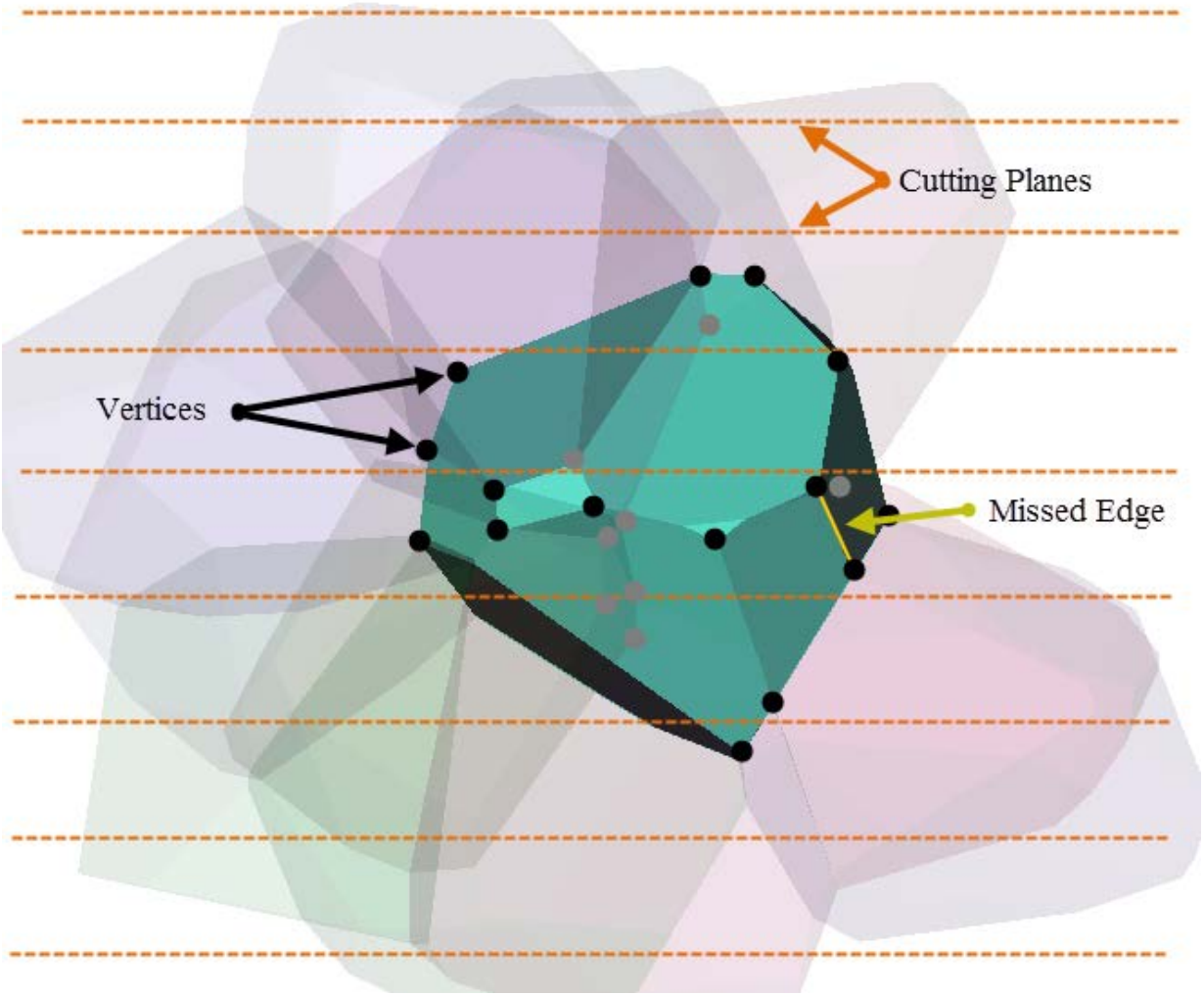

Figure 3-10 – Imaging technique drawbacks for VFM. Based on the imaging process using a confocal microscope, the planes at which the images are taken do not necessarily pass through the node of cells. Only one cell is highlighted for easier visualisation.

Furthermore, it became obvious that it is extremely difficult to accurately locate the position of vertices with this method. Some of the most important reasons are as follows:

1. Low quality images make it difficult to accurately locate TJs which subsequently increases the error seen in the interpolation process (Figure 3-7).

2. The cell aggregate is suspended in a liquid medium during the imaging process, allowing it to move around freely. Although this movement is quite small, there is some error related to this when moving from one time step to the next. This means that each 2D image is slightly rotated to an unknown degree which leads to greater error in the interpolation result.

3. Mesh consistency is the most important issue when using the inverse finite element method. However, it frequently happens that from one spatial stack to the next stack the number of edges and nodes will change. This may be the result of poor image quality or movement of the aggregate during the imaging process.

3.3 Assembling the 3D Model

The challenging part in constructing a 3D cell aggregate model is to determine which edges and TJs seen in the 2D spatial images belong to the same cell, face or edge in 3D. This process is called grouping; node (TJ or edge nodes) gathered from every digitized 2D image (i.e., spatial stack), are categorized into cell, face and edge groups in 3D (Figure 3-11). The grouping process starts with generating an instance of a PCM which is designed to hold all extracted data. The PCM is equipped with a large number of maps which hold the relationships between the points, edges, faces and cells. The software toolbox was designed to include the mathematical tools for curve and surface fitting purposes and have user friendly menus and functions to easily access the required information. As the grouping

process continues and the PCM gets filled with points from each 2D digitized image, the program automatically fits surfaces and curves to the data and keeps them updated as the number of points in the model changes. Two different algorithms were tested for use in the surface fitting process. A hybrid feature was also configured which used both algorithms simultaneously on different faces of the model. The details of both algorithms and the calculation of the dihedral angles (Young angles) are discussed in the next section.

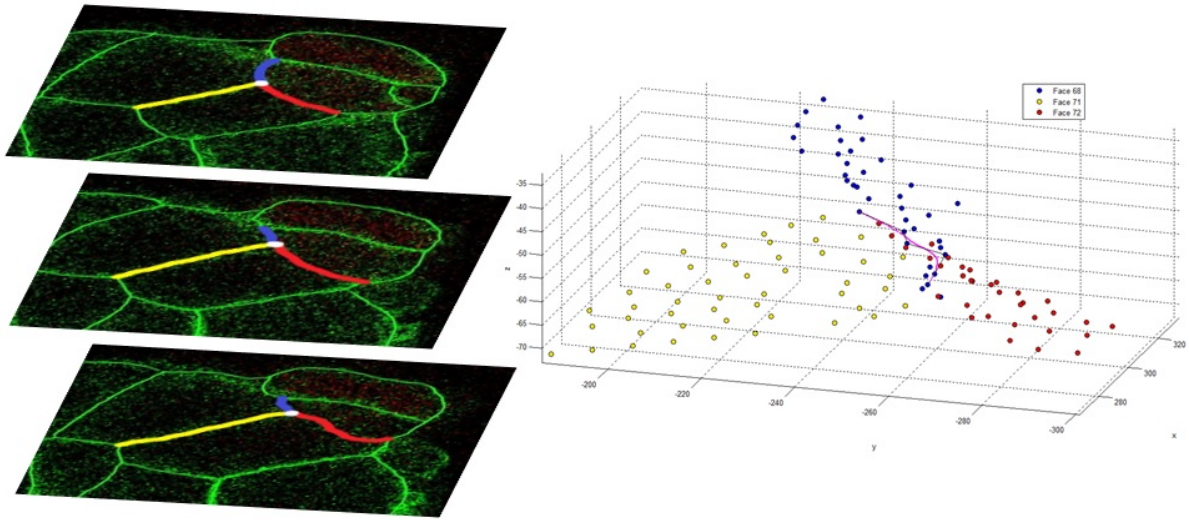

Figure 3-11 – 2D edges in each slice make the PCM in 3D.

Once the Young angles are obtained, the geometric matrix, G, will be assembled. The coded PCM has the capacity to generate, fill and save the required matrices, then call the least square solver to prepare for the required matrices and solve for face tensions. Section 3.3.2 describes these procedures in detail.

3.3.1 Fitting Algorithms and Young Angle Calculations

In order to calculate the so-called Young angles between faces, not only is the geometry of the face required but it is also necessary to have a clear understanding of how to measure these angles. In order to extract the required information about the faces and cells, several toolboxes were developed in C++. These toolboxes were used to obtain the dihedral angles between the adjacent faces. Furthermore, they made it possible to visualize the information by plotting the point clouds and associated surface fits in 3D.

Figure 3-12 shows the B-spline curve (order of three) of an edge passing through the TJs shown in red dots (P_{i-1}, P_i and P_{i+1}). Note that TJs are identified by their neighbor cells (in this case A, B and C) and have been grouped together through the grouping process described in the beginning of Section 3.3 earlier in this chapter. As is the case with the B-spline (shown in blue) in Figure 3-12, in general, edges do not necessarily make a normal angle with the 2D sections. Therefore, the angles between the dashed arrows cannot be counted as the Young (dihedral) angles.

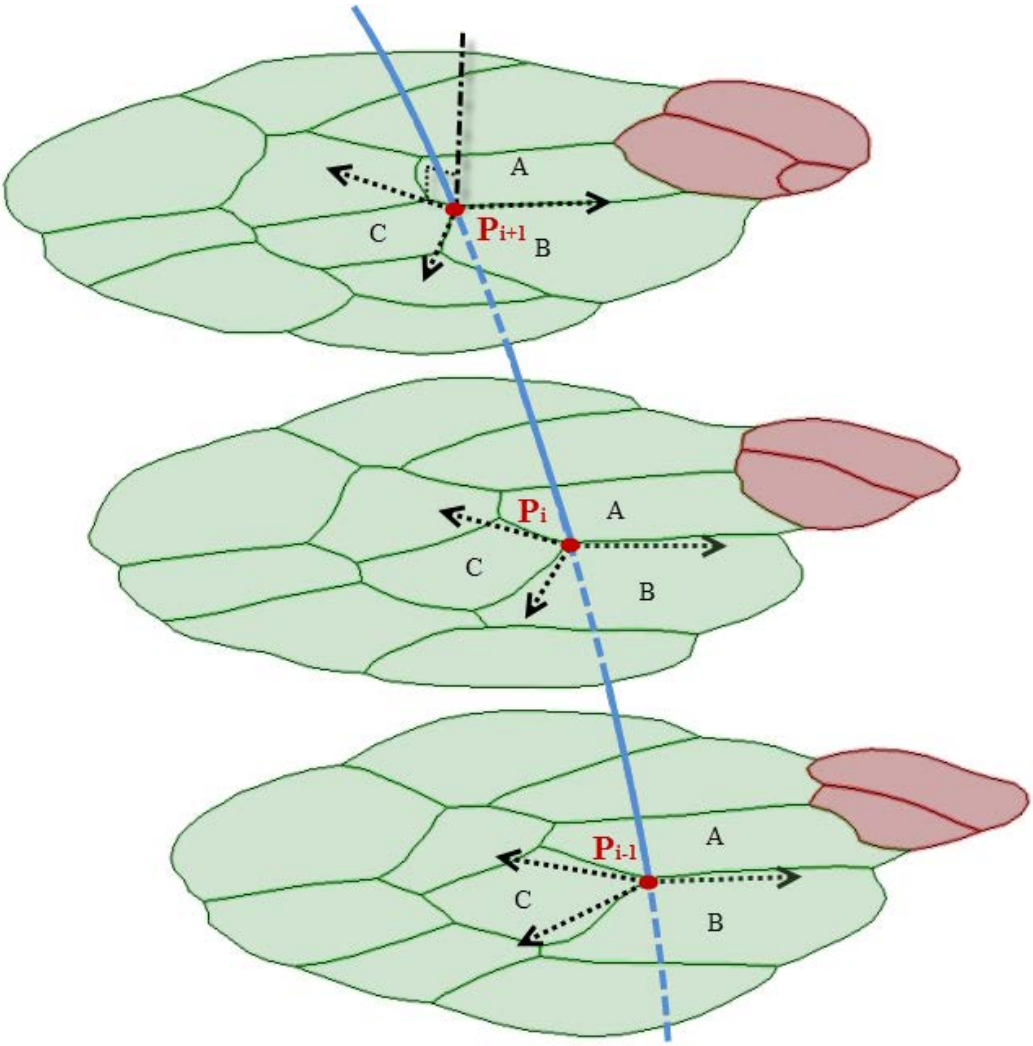

Figure 3-12 – Calculating Young (dihedral) angles. The blue line shows a 3D edge made by connecting the same TJs through consecutive sections.

As the slope of the B-spline changes from one end to the other, the angles between the touching faces seen on 2D images (angles between dashed arrows) vary from one image to another. Figure 3-13 illustrates how the dihedral angles are calculated by means of tangent vectors. In order to obtain the tangent vectors, we have developed two different methods: Sphere fitting and Projection method. Both of these methods use the data of several images in a spatial stack to obtain accurate tangent vectors.

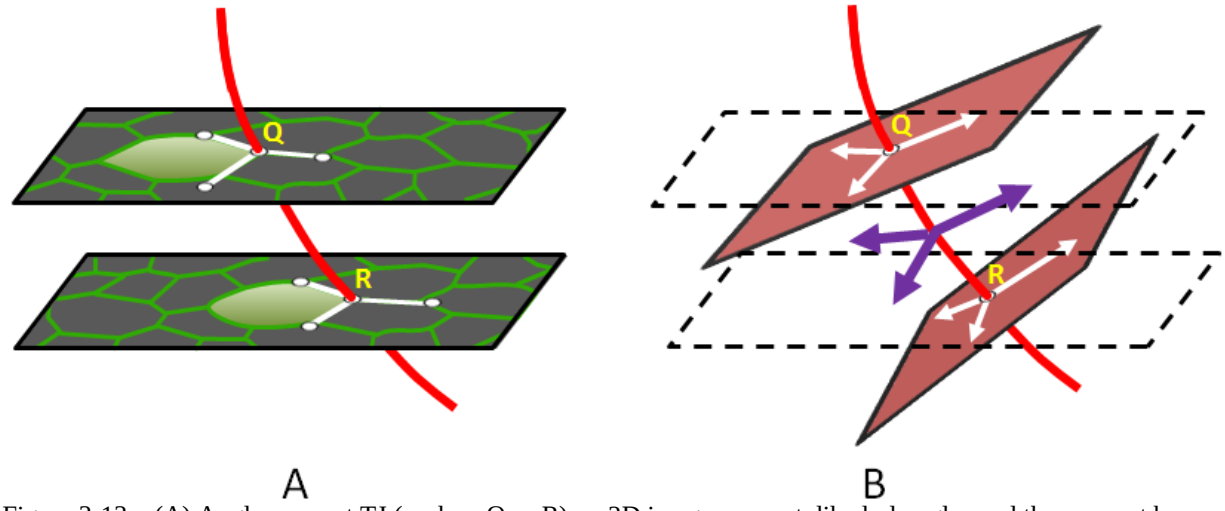

Figure 3-13 – (A) Angles seen at TJ (such as Q or R) on 2D images are not dihedral angles and they cannot be counted as Young angles (B) dihedral angles can be calculated on a plane normal to 3D edge and mid-way along the curve by means of vectors tangent to each touching face.

For cell-medium faces, the pressure difference and isotropic face tension lead to create a convex shape over the entire surface. This means that a sphere can be fit to the point cloud associated with that face. This sphere, then, is used to obtain the tangent vector at the middle of each 3D edge (Figure 3-14). The following steps show how the tangent vectors are obtained for each 3D edge:

1. A B-spline of degree 3 is fit to the point cloud of the edge, (note that the point cloud consists of TJs obtained from 2D images.
2. A point (say point P) is chosen in the middle of the generated B-spline. The tangent vectors are calculated in this point.
3. A plane is defined at point P with normal vector (N) tangent to the B-spline at that point.

4. One of the three connected faces to the given edge is chosen and a sphere is fit to the point cloud by a least squares technique.

5. Vector $\overrightarrow{CP}$ is generated between points C (sphere centre) and P (generated in step 2).

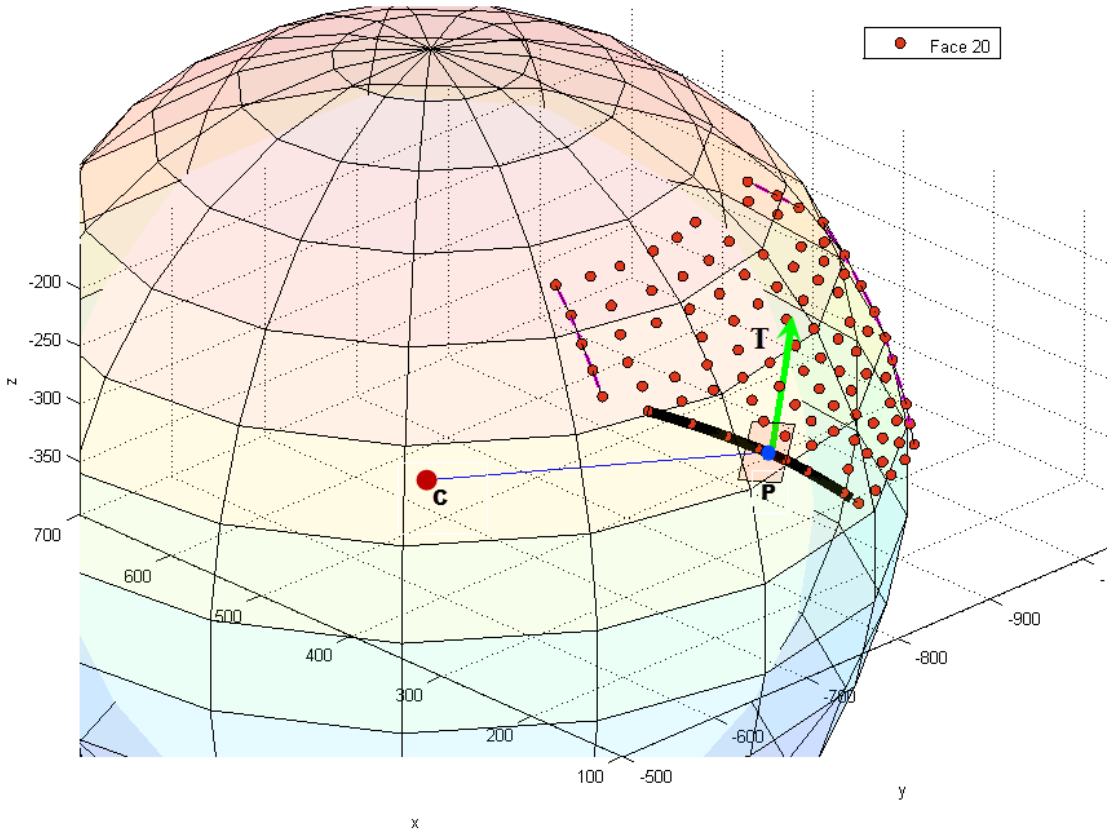

Figure 3-14 – Sphere fitting technique. The tangent vector at point p is obtained by taking the cross product of CP (C showing sphere centre) and the plane normal vector at p. Only one point P is shown along the 3D edge for simplicity.

6. The face tangent vector can be obtained from the following equation:

$$\vec{T} = \overrightarrow{CP} \times \vec{N} \quad (1)$$

where $\overrightarrow{CP}$ is a vector from the sphere's center to a point on an edge curve, $\vec{N}$ is the plane's normal vector, and $\vec{T}$ is the tangent vector of the face for the given edge.

7. The process is repeated for other two faces.

Figure 3-15 shows that projection method applied to two faces with a common edge. In order to find the tangent vectors, this method uses the point cloud itself rather than fitting a pre-defined geometry to it. The following steps explain procedure to obtain the face tangent vectors for a given 3D edge:

1. A B-spline is fit to the point clouds of the given 3D edge.
2. A point (P) is assigned at the midway along the B-spline.
3. Next, using the tangent vector of the edge curve at point P, a plane E is defined in point P. Note that the plane is considered infinite.
4. Points within a certain vicinity of this plane are projected normally onto the plane E. The points will generate a trace of the face geometry. The vicinity value is then determined as 10% of the distance between the two points that are located at the farthest distance in the point cloud (Figure 3-15), so that we do not need to define this value for each face.
5. A B-spline curve (degree of three) is fit to the points and the face tangent vector of the curve at point P is obtained (T1 or T2 shown in Figure 3-15).

The tangent vectors obtained so far are all of unit length vector. The goal is to later solve for the values of the tensions along these vector directions.

Both techniques are implemented by means of the Geometric Tools Engine (GTEngine v1.12). This library is developed in C++ and has the source code available for computing in the field of mathematics, graphics, image analysis, and physics. It is also equipped with predefined functions to fit different geometries and obtain their properties.

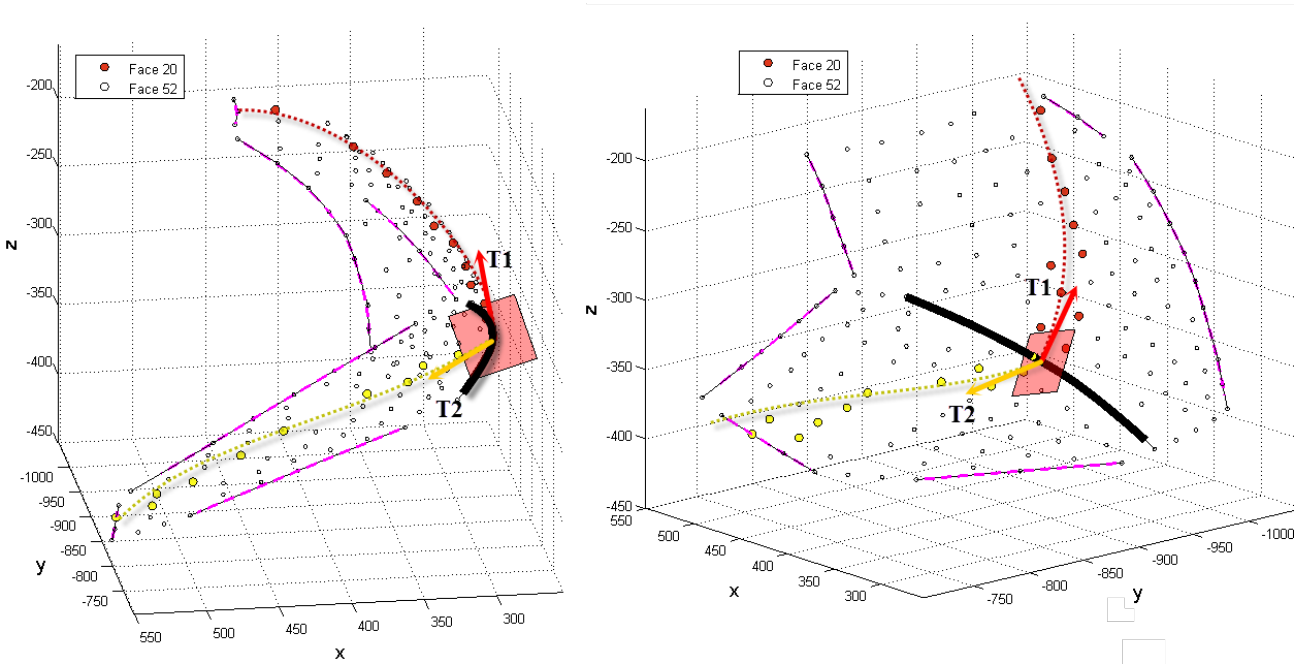

Figure 3-15 – Point projection method for calculating the face tangent vector. The black curve is the common 3D edge between three faces. For simplicity only two faces are shown. The colored points are projected onto the plane. The dotted curve shows the B-spline fit to projected points. The T1 and T2 vectors are the tangent vectors. Both vectors are normal to the curve.

3.3.2 Equation Formation and Least Square Solution

Thin surfaces such as cell membranes are not capable of carrying either shear or bending forces (Cook, Young 1999). Therefore, only tangential forces act along their surface.

Equation 1 shows the relation between these the tangent force and the tension T in the membrane:

$$\gamma = \frac{F}{L} \tag{2}$$

where γ is the linear tension with unit of N/m and L is the length of the circumferential edge or an imaginary cut on which the resultant force F is acting.

Assuming that the cell volumes are constant, the tensions (tangential forces) in surrounding cytoplasm gives rise to an internal pressure. For a membrane between cells i and j, this pressure difference can be written as

$$\Delta P = p_i - p_j \tag{3}$$

A nonzero ΔP makes the membrane take curved shape. This curved shape will satisfy the Young-Laplace Equation.

$$\Delta P = \gamma(\frac{1}{\rho_x} + \frac{1}{\rho_y}) \tag{4}$$

$$\Delta P = 2\gamma/\rho \tag{5}$$

where Δp, is the pressure difference (also known as the Laplace Pressures), γ is the membrane tension and ρ_x and ρ_y are the principal radii of the curvature in each of the axes parallel to the membrane. Considering Equation 4, the pressure values can be calculated once the face tensions γ are available. Assuming that there is only one curvature in both directions, as in a sphere, Equation 4 can be simplified into Equation 5.

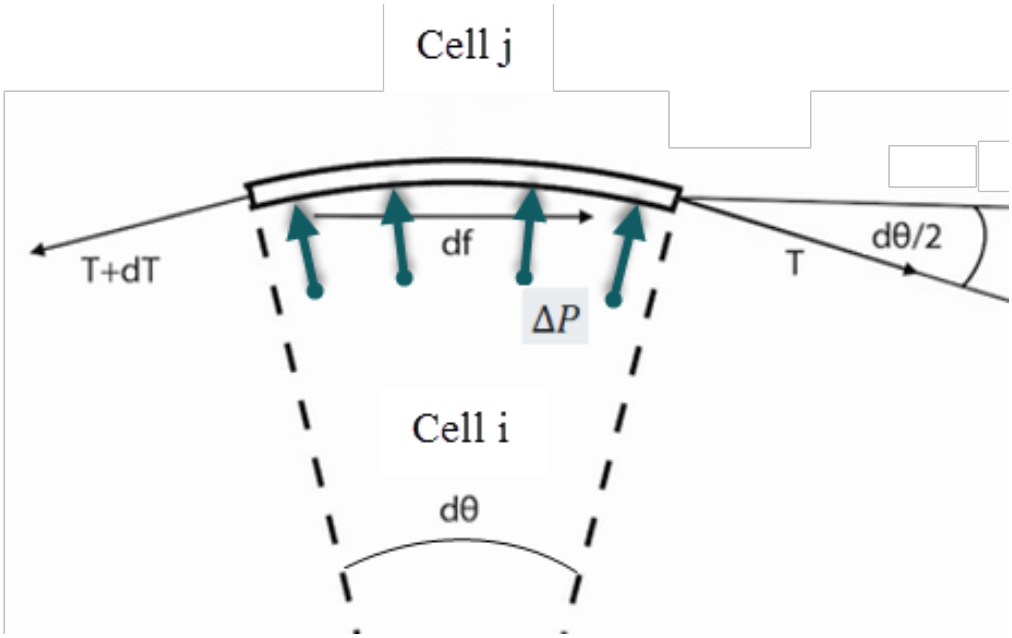

Figure 3-16 – Inside pressure affects the direction and magnitude of the face tensions. The curvature of the face is caused by the presence of internal pressure which, in turn, has changed the direction of the tensions inward to counter balance the pressure.

Considering the fact that all QJs (located on 2D images) are converted into TJs (Figure 3-9), every 3D edges (such as curve shown in blue in Figure 3-12) in our model would be in touch with only three faces.

Consider three cells touching with a common edge (curve). Any two of the cells would also have a common face, F_{ij}, where the subscript identifies which cells it belongs to. The three faces would in turn touch along the same common edge. This curve is in fact the trace of the same TJ through the stack (Figure 3-15). If we assume that the cells are not moving, the force equilibrium should be satisfied between three faces. Assuming that these faces make constant angles with each other along their common edge, we can write the equilibrium equation for a single point on the curve. To this end, as described earlier, the effect of face

tensions would translate to a force vector tangent to each face and normal to the 3D edge. Equation 6 shows the equilibrium condition in vector form. The component form of this equation is shown in Equation 7.

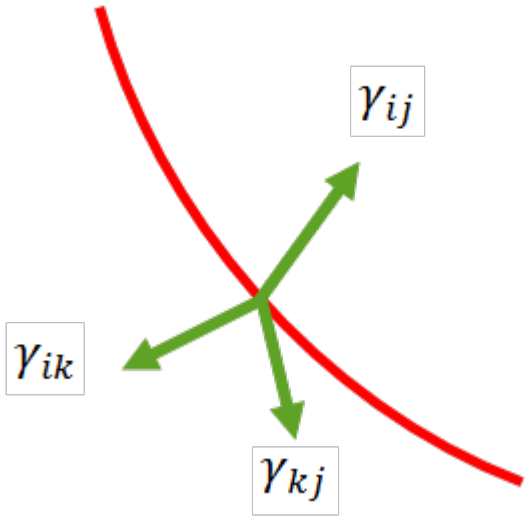

Figure 3-17 – Tangent vectors of three faces in mid-point along the 3D edge. These vectors can be rewritten in component form along x, y and z axis.

$$\sum \gamma_{ij} = 0 \quad \rightarrow \quad \sum L\vec{F}_{ij} = 0 \quad \rightarrow \quad \sum \vec{F}_{ij} = 0 \tag{6}$$

where L is the length of the 3D edge obtained from the B-spline curve. Since this length is the same for all three faces touching the edge, it can be removed to produce the equation:

$$\begin{Bmatrix} F_{ij\,X} + F_{ik\,X} + F_{kj\,X} \\ F_{ij\,Y} + F_{ik\,Y} + F_{kj\,Y} \\ F_{ij\,Z} + F_{ik\,Z} + F_{kj\,Z} \end{Bmatrix} = \begin{Bmatrix} 0 \\ 0 \\ 0 \end{Bmatrix} \tag{7}$$

Assuming these three forces are in balance, Equation (7 shows the system of equation associated with the three tangent vectors in component form. These equations are then assembled into geometric matrix (G) shown in Equation (8.

$$\begin{bmatrix} \ddots & & & & & \\ & G_{ijx} & & G_{ikx} & & G_{kjx} \\ & G_{ijy} & \cdots & G_{ijy} & \cdots & G_{ijy} \\ & G_{ijz} & & G_{ijz} & & G_{ijz} \\ & & & & & \ddots \end{bmatrix} \begin{Bmatrix} \vdots \\ \gamma_{ij} \\ \vdots \\ \gamma_{ik} \\ \vdots \\ \gamma_{kj} \\ \vdots \end{Bmatrix} = \begin{Bmatrix} \vdots \\ 0 \\ \vdots \\ 0 \\ \vdots \\ 0 \\ \vdots \end{Bmatrix} \tag{8}$$

where geometric entries such as G_{ijx} are a value between zero and one and correspond to the contribution of γ_{ij} along the x-axis. Repeating the same process for all edges, results in three times as many equations as the number of edges. These equations can then be simplified by writing them in matrix form:

$$[G_\gamma]\{\gamma\} = \{0\} \tag{9}$$

where each of the triple rows in the G_γ matrix, corresponds to the x-, y- or z-direction of a single node, respectively. Each row contains only 3 trigonometric terms correspond to the attached faces. Equation 9 is homogeneous, and requires an extra constrain to obtain a meaningful solution. This constrain was applied by adding vector C_1 to our G matrix. The constrained least-squares equation system is constructed and solved as follows:

$$\begin{bmatrix} G_\gamma^T G_\gamma & C_1^T \\ C_1 & 0 \end{bmatrix} \begin{Bmatrix} \gamma_1 \\ \vdots \\ \gamma_N \\ \lambda_1 \end{Bmatrix} = \begin{Bmatrix} 0 \\ \vdots \\ 0 \\ N_T \end{Bmatrix} \tag{10}$$

where

$$C_1 = \{1 \quad \ldots \quad 1\} \tag{11}$$

The vector C_1 in the last row adds an extra condition, $\overline{\gamma} = 1$, which makes the elements in the tension vector to have mean value of one. N_T in the right hand side on Equation 10 is the

number of faces being included in our equation, and λ_1 is the Lagrange multiplier associated with this constraint. Since we are dealing with an overdetermined system and our G matrix is generally well conditioned, a least absolute deviation solver (Hayashi 2000, Kwiesielewicz 1996), was used to solve Equation 10. The solution to Equation 10 is a set of tensions for all faces included in that equation. In order to find the correct magnitudes for the tensions, an external data such as the tension for a particular face is required.

Once the tension vectors are obtained, the intracellular pressures can be calculated. The number of equations in these calculations is equal to the number of faces used in Equation 9. Generally, small faces cannot be used for pressure calculations since they are not large enough to provide reliable curvature information. However, since faces in the PCM are only defined if they already have sufficient points in their point cloud, small faces would not be generated. In general, cells in an aggregate are in touch with several neighbor cells which results in an over-determined system of equations. For any face inside an aggregate we can write Equation (3) and then assemble all such equations in the form

$$[G_p]\{p\} = \{q\} \tag{12}$$

where each row of the equation above represents the pressure equation (Equation (3)) for a face. Therefore, the left side of Equation 12 shows $\Delta \mathrm{p}_{ij}$. In each line of G_p matrix, only two pressures are involved resulting in two non-zero entries, a 1 and a -1. Once the face tensions are available, using Equation 6, the right hand side of Equation 12 is calculated. Now that the G_p and q matrices are known, we can solve for the pressures in a least square manner. Again, to avoid a zero solution, a constrained least-square system is set up:

$$\begin{bmatrix} G_p^T G_p & C_2^T \\ C_2 & 0 \end{bmatrix} \begin{Bmatrix} p_1 \\ \vdots \\ p_N \\ \lambda_2 \end{Bmatrix} = \begin{Bmatrix} G_p^T q \\ 0 \end{Bmatrix} \tag{13}$$

where

$$C_2 = \{1 \quad \dots \quad 1\} \tag{14}$$

and λ_2 is the Lagrange multiplier associated with the constraint $\overline{\mathrm{p}} = 1$.

In order to assess the quality of the calculated tensions, we can look at several parameters such as condition number, residuals and standard errors. Although, these parameters do not guarantee a correct answers but they will strengthen the results since they are required for any proper answer. The condition number is the first of these tools that shows the ratio of the greatest to smallest singular value. In other words, the condition number corresponds to the relative change on the output for a relative change in the input. The condition number can be calculated by singular value decomposition.

Another tool to evaluate our approximate results obtained from least square is the residual vector

$$R = G_\gamma \gamma - 0 \tag{15}$$

The residual vector here, indicates how well we satisfy the original equations. In general, the solution always has some inaccuracy because of the error in Young angle calculation or noisy images.

Finally, to calculate the confidence limits for the calculated tensions, we obtained the conventional standard error from covariance matrix (Hayashi 2000). The standard errors show the overall uncertainty in the calculated tensions.

3.4 Synthetic Data for Verification

In order to test and validate the proposed PCM and selected algorithm approaches, the steps outlined above were tried on two types of synthetic models in which the ground truth values of face tensions were already known. Each synthetic model was generated with different approaches. The first type of model was generated by Voronoi tessellations, a conventional approach, an approach previously developed in our lab (Viens, Brodland 2007). The second type of synthetic model was generated by Surface Evolver software. These synthetic models are called V-type and S-type, respectively, throughout the next chapters. To prepare the V-type synthetic data, the Voronoi model was first converted into finite element meshes consisting of 3D elements with assigned face tensions. This model was run in forward finite element code until further movement ceased (Brodland, Veldhuis 2003, Chen, Brodland 2000). This step is called annealing process (Figure 3-18) and ensures that our model meets the static equilibrium condition which is required for the proposed solution to remain valid. In order to generate a model which closely resembles biological data, cells in the aggregates were randomly assigned to one of two cell types, giving rise to five interface types with corresponding face tensions. The aggregate was converted into a stack of 2D meshes made from intersecting stacks of planes equally spaced along the z-axis. This was done to emulate the type of 2D images which would be generated from a confocal microscope. All force

information was then erased from the finite element patches and only geometry data was saved into each slice. Then, the face tensions were obtained by calculating the Young angles, assembling the system of equations and solving the system. The results were then compared with true values used to create the synthetic data. The advantages and disadvantages of this method are noted in detail in Chapter 4. The spacing value used in stacks of cut planes determines the number of 2D slices the code will generate from the 3D model. In other words, the spacing value affects the amount of data captured from the original 3D model into 2D images. As will be seen in Chapter 4, the greater the number of slices, the more information will be made available and the more accurate the results obtained. However, the drawback is that it is not actually feasible to take a large number of pictures in real biological specimens due to photobleaching and phototoxicity effects.

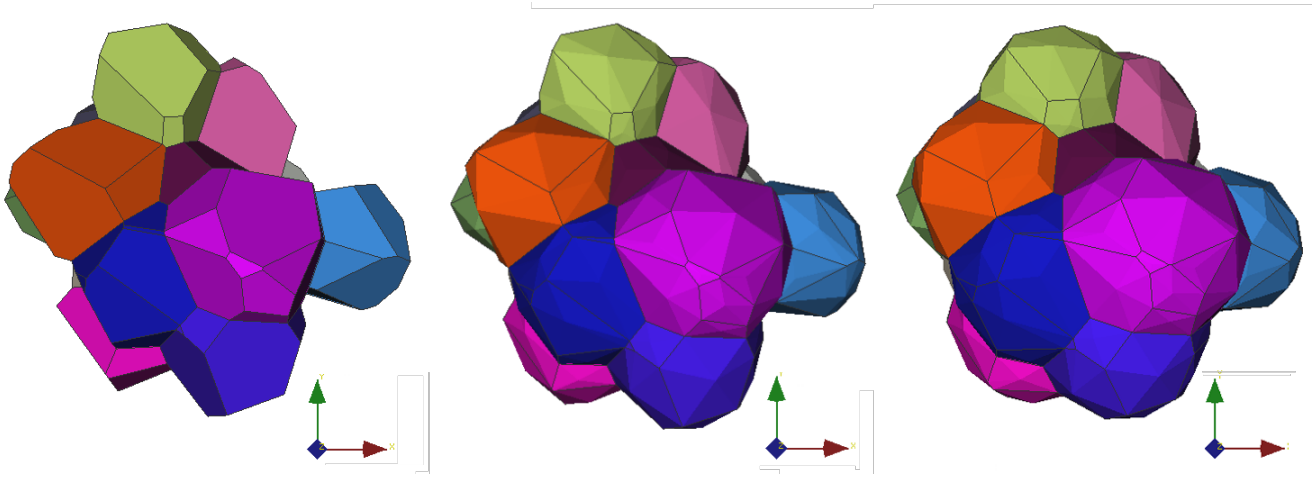

Figure 3-18 – Annealing process (left to right), applied to the synthetic model before generating the image stacks.

The S-type synthetic model was generated using a completely different software. Examining all commercially available software, Surface Evolver seemed to be a good option for creating a model for the purpose of performance comparison with the novel proposed

approach of this thesis. Surface Evolver is an interactive program for the study of surfaces shaped by surface tension and other energies and subject to various constraints (Figure 3-19). Within this software a surface is implemented as a union of triangles. The user defines an initial set of surfaces with desired tensions in a "datafile." Then the software evolves all surfaces toward minimal energy by a gradient descent method. The aim is to find a minimal energy surface or to model the process of evolution by mean curvature (Brakke 2005).

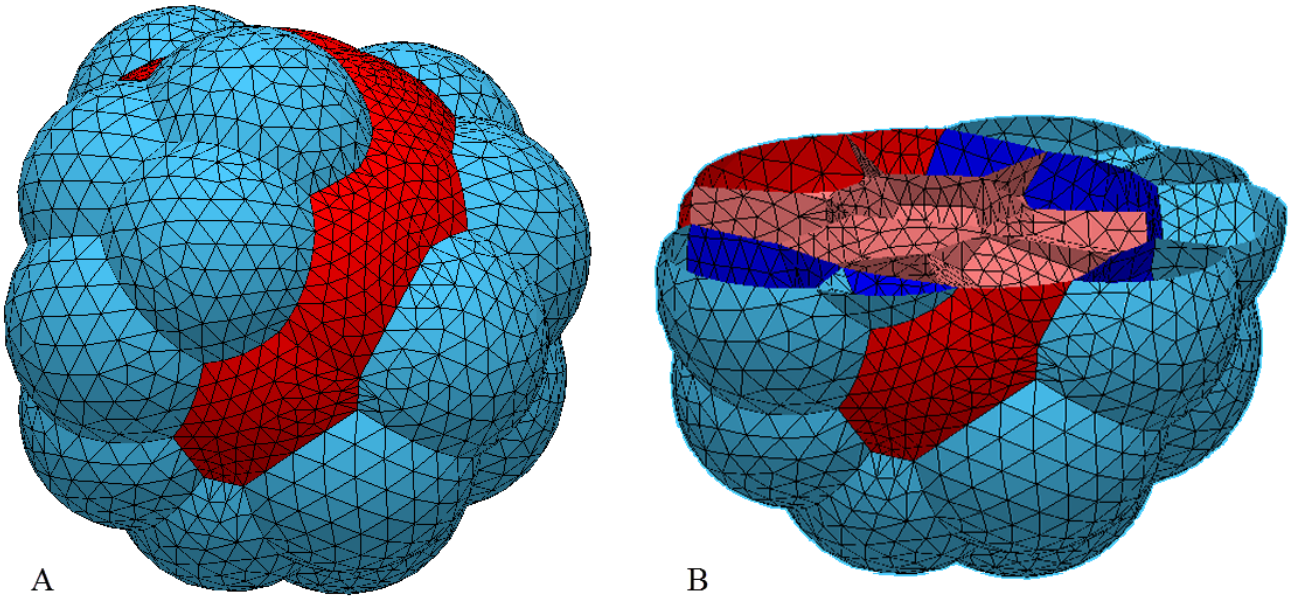

Figure 3-19 – Surface Evolver synthetic model. (A) An aggregate of thirty cells is fully evolved so that no displacement is observed. (B) The model has been cut to show the inside faces.

Finally, whether the direction from which the images are taken in the stack has a significant role on obtained results was investigated. To assess this, a synthetic model was

sliced along two different vectors and their resultant face tensions were compared. These runs and their findings will be discussed in detail in the next chapter.

Chapter 4
Results and Discussion

This chapter contains a summary of the results obtained using the algorithms described in Chapter 3 with both data from synthetic models and biological specimens. Section 4.1, discusses the results found using the CellFIT toolkit (Brodland, Veldhuis et al. 2014) on the S-type synthetic model and compares them against the results of the 3D approach proposed in this thesis for the same model. Note that the CellFIT approach was originally developed to study 2D data sets, such as monolayer tissues (i.e., epithelium), but given the similarity of concept between the two models, it was considered worthwhile to use the CellFIT results as a comparator when assessing the performance of the proposed 3D method. In Section 4.2, the results of the sphere fitting algorithm when used on both S- and V-type synthetic models are discussed. In Section 4.3, the point projection algorithm is used in place of the sphere fitting algorithm to calculate the tensions. Then the results of both sphere fitting and Point Projection methods are compared against the true tension values. Next, in Section 4.4, the results for the hybrid algorithm are shown with the point projection algorithm applied to internal (cell-cell) faces and the sphere fitting algorithm applied to the outer (cell-medium)

faces. We show that the hybrid method works best, giving tensions within 6% of their true values. Section 4.5 shows the results for the same synthetic model sliced along different, randomly chosen axes. It is demonstrated that the proposed algorithm works well regardless of the direction of the slicing. Using synthetic models, in Section 4.6, the optimal number of slices required to generate accurate tensions was investigated. Then in Section 4.7, the algorithms were applied to the biological data and results compared with those obtained in other labs.

As briefly noted in Section 3.4, two types of synthetic model were prepared in this thesis to make sure the proposed algorithm works properly. The approach to generating the first model, V-Type, was developed in the lab in which the author was researching. The second model, S-type, was generated by means of Surface Evolver software (Brakke 2005). In this chapter, we will use the same name to refer to each model.

The V-Type model was synthesized with the Voronoi algorithm which was run long enough to allow the annealing process to take place (Figure 3-18). It contained fifteen cells with two different cell types randomly assigned through the patch. The S-Type model included thirty cells with randomly assigned cell types. For simplicity, the cell types were named Red and Green. Here, in this thesis, they are representing mesoderm and ectoderm cells that are found in biological data and their name, Red and Green, were chosen based on the staining color used for coloring the cytoplasm of mesoderm and ectoderm cells, respectively. However, with the right cellular properties, Red and Green could represent any type of cell. Having two types of cells and considering the surrounding liquid (medium) as a

separate cell leads to five types of membrane based on the neighboring cells which are shown in Table 4-1.

Table 4-1 – Input tensions for the synthetic models. Each column represents a face type.

	Face Types				
	Red-Red	Green-Green	Red-Green	Red-Medium	Green-Medium
Assigned Tensions	**1**	**1.5**	**2.5**	**3**	**1.5**
Number of Faces (V-Type)	**6**	**22**	**18**	**4**	**11**
Number of Faces (S-Type)	**44**	**28**	**48**	**14**	**17**
Tension Normalizing Factor	**0.542**				
Normalized Tensions	**0.54**	**0.81**	**1.36**	**1.63**	**0.81**

As described in Chapter 3, the relative face tensions are being solved with a mean value of one for all faces. Therefore, in order to compare the calculated tensions with input values for the synthetic models, the input tension values need to be in the same scale and have mean values of one. Based on the number of faces, the last row of the Table 4-1 contains the modified tensions with an average of one, so that the output results can be compared.

All synthetic models were generated with the same initial faces tensions shown in Table 4-1, and were sliced with the same spacing or average number of slices per cell (SPC) of nine, as is normally found in the biological data. In this way, it was ensured that more data would not be artificially extracted than what is available in practice with biological data.

4.1 2D Approximation (CellFIT)

The CellFIT toolkit – developed and published by Brodland and his group (Brodland, Veldhuis et al. 2014) – is designed to work on cells that are formed in a monolayer surface. This toolkit looks for TJs and the curvature of the cell outlines in 2D digitized images. Then, it calculates the relative tensions of different membranes. In this thesis, this toolkit is applied to a single slice of the synthetic 3D patch (Figure 4-1). The result can then be compared with true tension values to get a sense of the level of error introduced upon 3D aggregates.

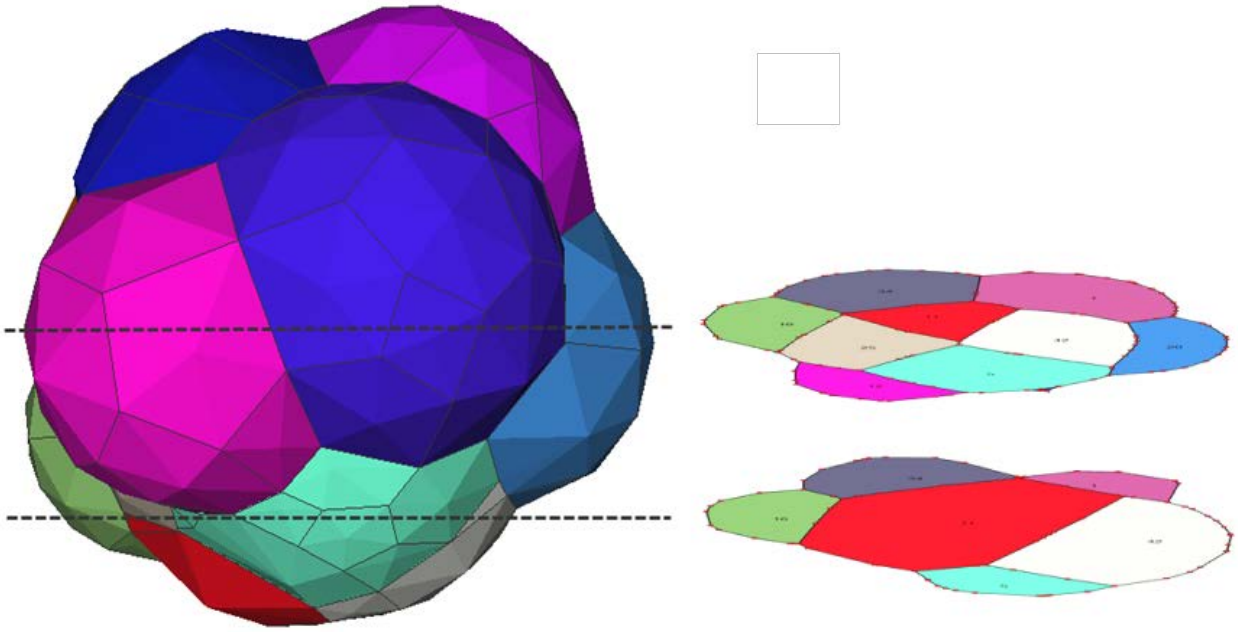

Figure 4-1 – A V-type synthetic model (Voronoi model) of 15 cells was used for CellFIT analysis. The aggregate was sliced with 30 horizontal planes (dashed lines). For simplicity only two slices are shown. Each of the slices was fed into the CellFIT toolkit.

The first row of Table 4-1 shows assigned values for face tensions before the annealing process starts. The second row corresponds to the number of faces of each type in the model. Note that since the assigned tension values are just a set of relative tensions, they should be of the same scale before they can be compared to the solved tensions. Therefore, the same condition of having the mean value of one is applied to all of the input tensions and the result is shown as modified values in the last row of Table 4-1. These values are used as the true values for comparison with the obtained results in this chapter.

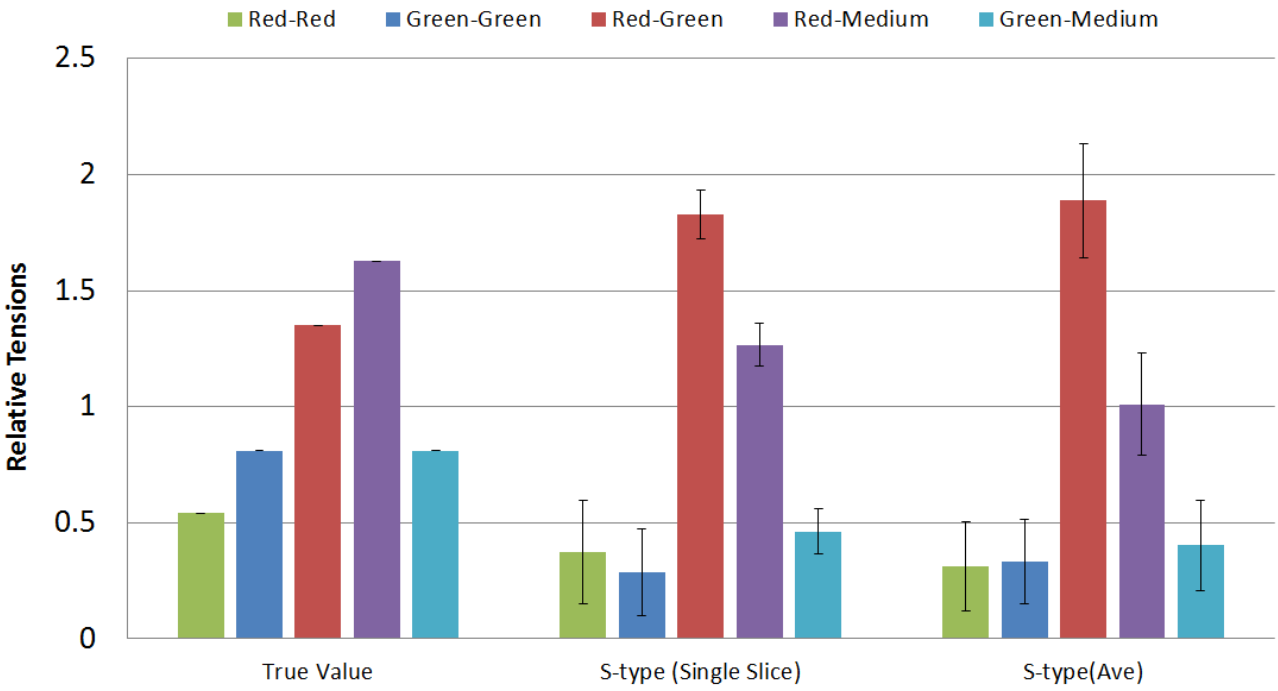

Figure 4-2 – CellFIT-2D results on 3D synthetic data. The first column in left shows the tensions values used to generate the synthetic S-type model. The middle group shows the results of the CellFIT-2D on a single section taken from the middle of the 3D aggregate. The right group shows the average of the tensions obtained for each single section.

Figure 4-2 shows the results of the calculated tensions for both the V-type and S-type synthetic models. The horizontal axis shows the five different face types whereas the vertical axis shows tensions values. The solid blue bar shows the true modified values shown in Table 4-1. Single slice analysis of both models (green colour columns), shows the high amount of error in the calculated tensions. Both slices were chosen from a region close to the middle of the aggregate so that the input section included as many cells as possible.

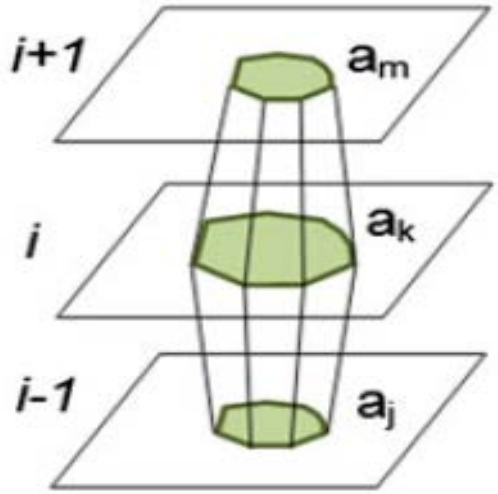

Figure 4-3 – Grouping process. Once the slices of a cell is sorted in spatial order they generally take a tapered shape. This tapering indicates that the 3D edges are also tends to move apart from normal vector of the slice plane (Kin Shun Leung, Veldhuis 2010).

The analysis shows that by choosing sections toward one end of the aggregate (away from the middle of the aggregate), the results from the CellFIT-2D software get worse. This is due to the tapered shape of the sliced cells. Generally, the slices in the middle of the aggregate have the largest area and this area decreases as the slices are taken closer to either end. (Figure 4-3). It should be noted that for a 3D patch of cells, a cutting plane at any given Z

level might pass through the end of one cell and the middle of another. This means that the angle between the 3D edge and the image's normal vector for some cells would be larger than for others. To compensate for this error, CellFIT was applied to all 2D digitized images and the average tensions were calculated. The purple columns in Figure 4-2 show the average values and diversity of slice values through the aggregate.

Figure 4.2 shows that the results for both the V-Type and S-Type models, have significant amounts of error with respect to the true values. This illustrates clearly that 2D algorithms are not reliable with 3D data.

4.2 Sphere Fitting Algorithm

As a first step, the sphere fitting algorithm was used on both synthetic models. As it is shown in Figure 4-4, the results for the S-Type model are a better match to the true tension values. Since the same algorithm was used on both synthetic models, the root of this discrepancy must lie within the accuracy of the fitting algorithm and the differences in the geometries of the two models.

Each face of the V-Type model consists of one centroid and multiple circumferential nodes. The centroid can move out of the face plane to generate curvature in the presence of intracellular pressure. To do so, each face divides into triangles where the face centroid is always one of the three vertices. Although the movement of the centroid introduces a curvature to the face, it represents the true shape of the face poorly. The S-Type model, on the other hand, is made of patches of triangles, relatively small compared to the size of the

cells, and perfectly generates the true curvature of the faces. Therefore, it can be considered as one of the sources of the difference we see in this result.

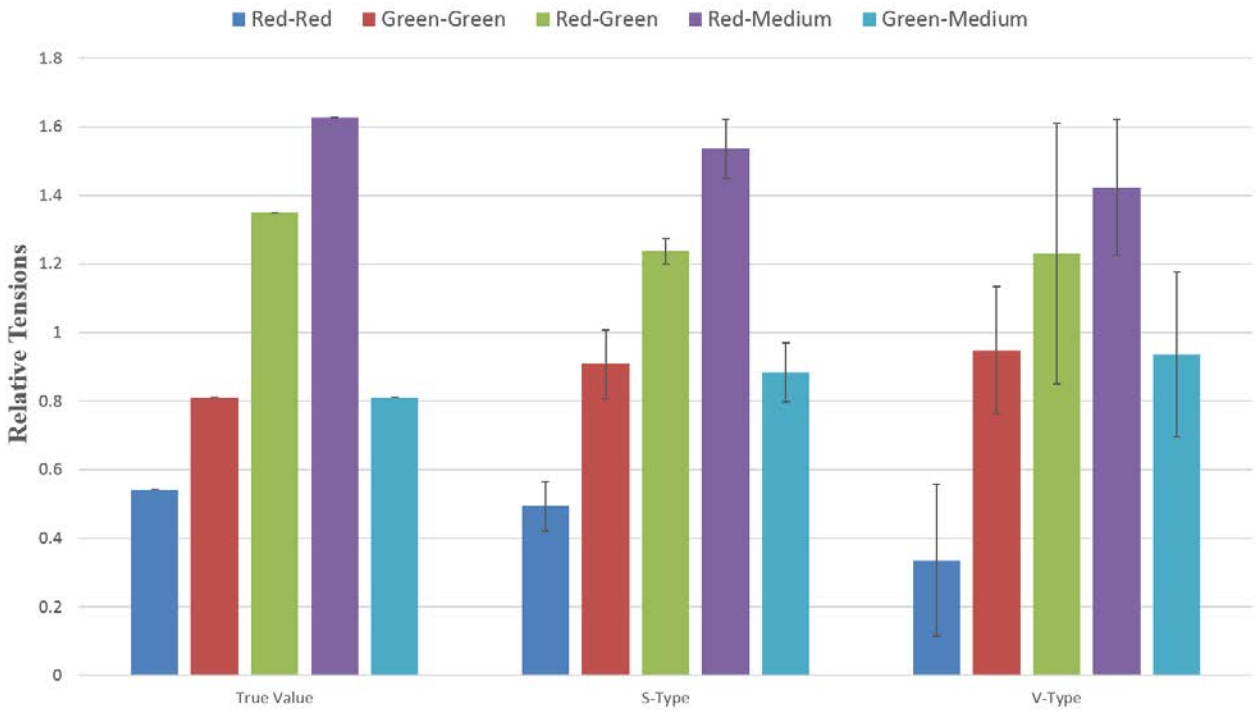

Figure 4-4 – Sphere fitting algorithm results. The Evolver method generates a slightly better result on cell-medium faces. The error bars show the standard deviation of all faces in each group.

Based on this understanding of the causes for the observed difference between the results of the two models, we can divide the faces into two different groups: cell-cell and cell-medium type and investigate the accuracy of the calculated tensions within each group. Figure 4-4 shows that cell-medium and cell-cell tensions obtained by the sphere fitting algorithm are within 8% and 12%, respectively. Medium faces are expected to have more accurate result since they have a round sphere-like geometry.

4.3 Point Projection Algorithm

The results of the point projection algorithm also show differences between the V-Type and S-Type model results (Figure 4-5). We can assume the same reason discussed in the last section is behind this difference. However, this time a high amount of error is observed on the green-medium face type. This was again predictable due to the nature of the algorithm used. The results show that the point projection method works well with interior faces which do not have a high curvature and gives weak results in obtaining accurate tangent vectors for medium faces.

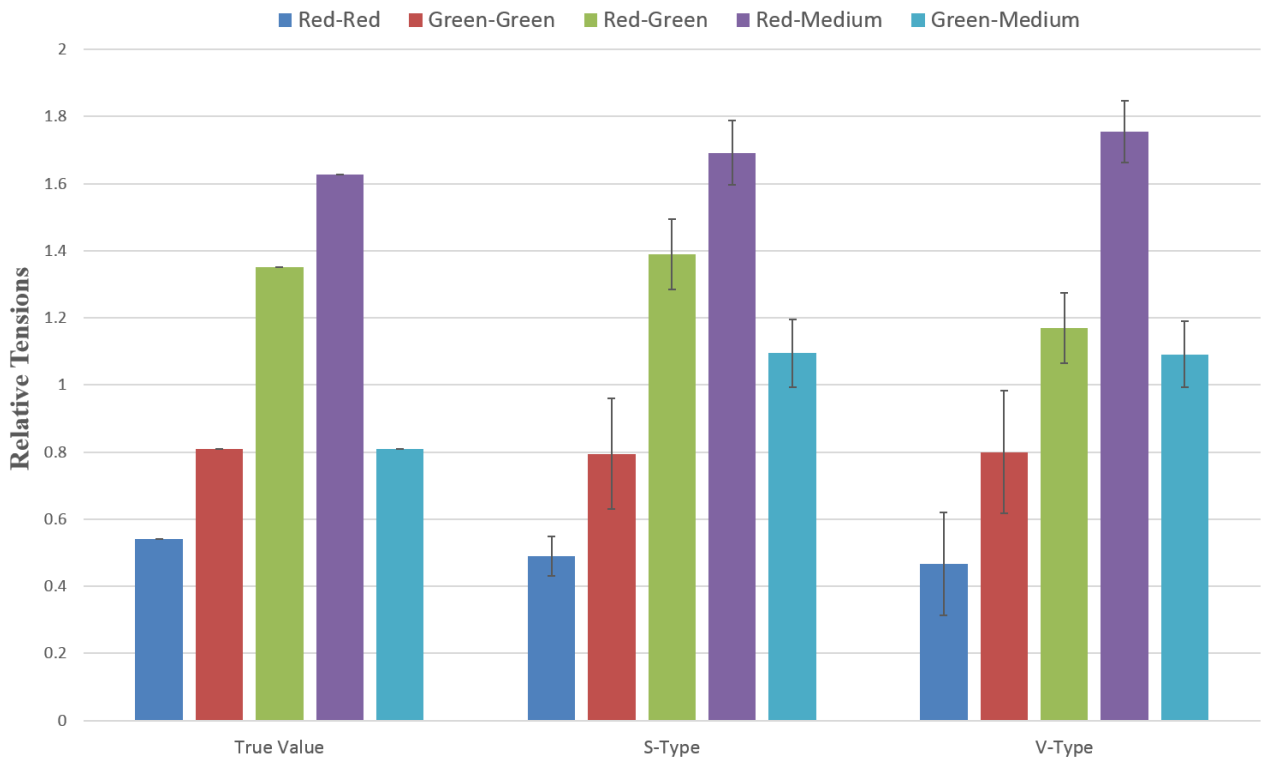

Figure 4-5 – Point projection algorithm results.

4.4 Hybrid Algorithm

In the hybrid algorithm, the point projection algorithm is used on internal faces (small curvature and large radius), and the sphere fitting algorithm is used on external faces (high curvature). In order to better compare the results of each method, information was gathered separately for each model. Figure 4-6 shows all three methods on the S-Type model. As can be seen, the hybrid method generated the most accurate results (within 7% of true values). The procedure was repeated for the V-Type model and the result is shown in Figure 4-7.

Overall the hybrid equations are very well conditioned – having the condition number of 15.14 to 18.20 for the S-Type model with 45 slices (13 SPC). Figure 4-8 shows the force residuals as calculated along the x, y and z axes. These residuals are within a small range and emphasize that the equations are generating accurate results.

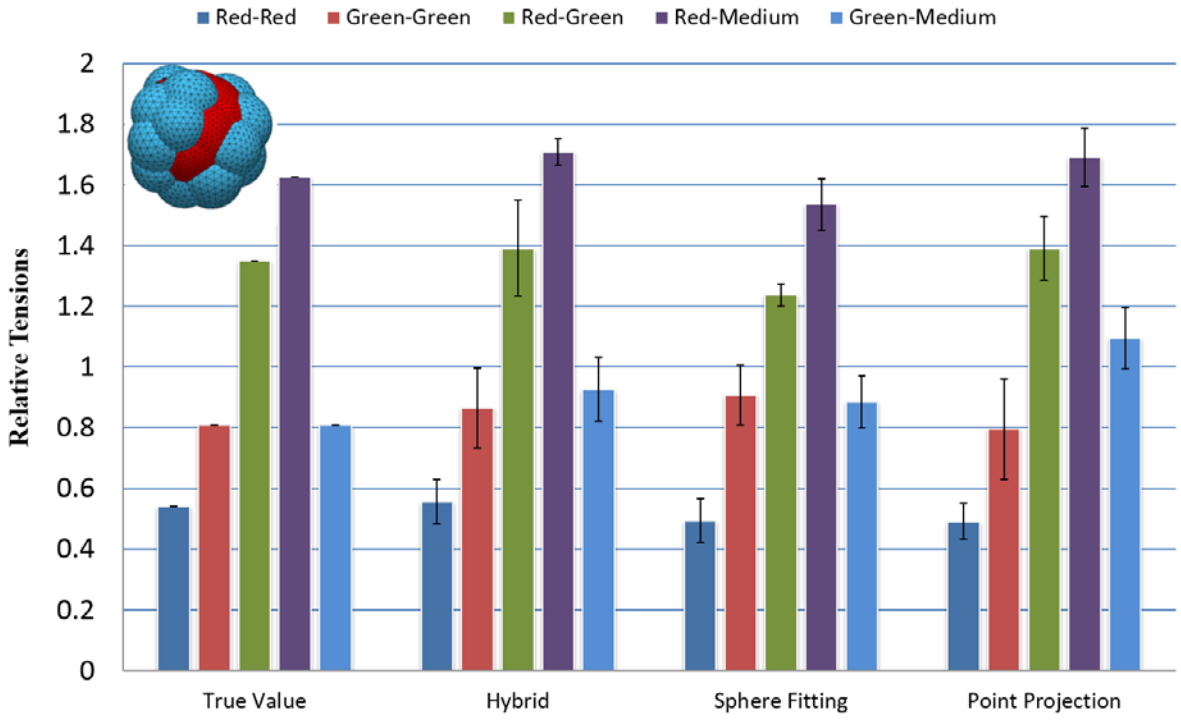

Figure 4-6 – Surface Evolver results

To explore the effect of noise on the results, different noise levels were introduced to the Young angles and the resulting tensions were compared with the previously obtained results. For this purpose, Gaussian-distributed errors with different RMS levels were introduced into each of the face angles before assembling the geometric matrix of Equation (9). The q level of noise in figure below corresponds to the RMS error of q degrees. For each noise level, a thousand different sets of noise values were introduced and the analysis rerun. As shown in Figure 4-9, a good level of accuracy was obtained with RMS noise levels of up to ten degrees. And finally, the confidence limits are drawn in Figure 4-10 for the obtained tensions based on the covariance matrix of the assembled geometric matrix, G.

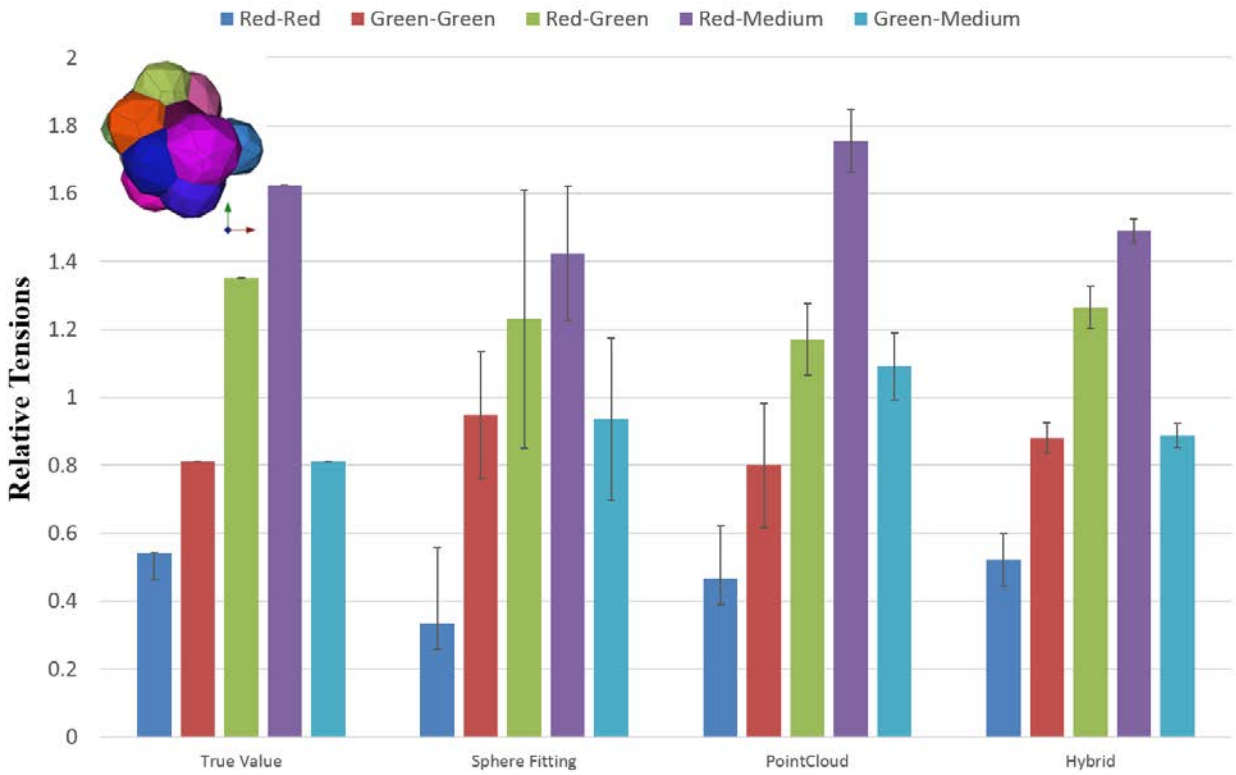

Figure 4-7 – Results of both fitting algorithms (sphere fitting and projection method) on Cell3D model.

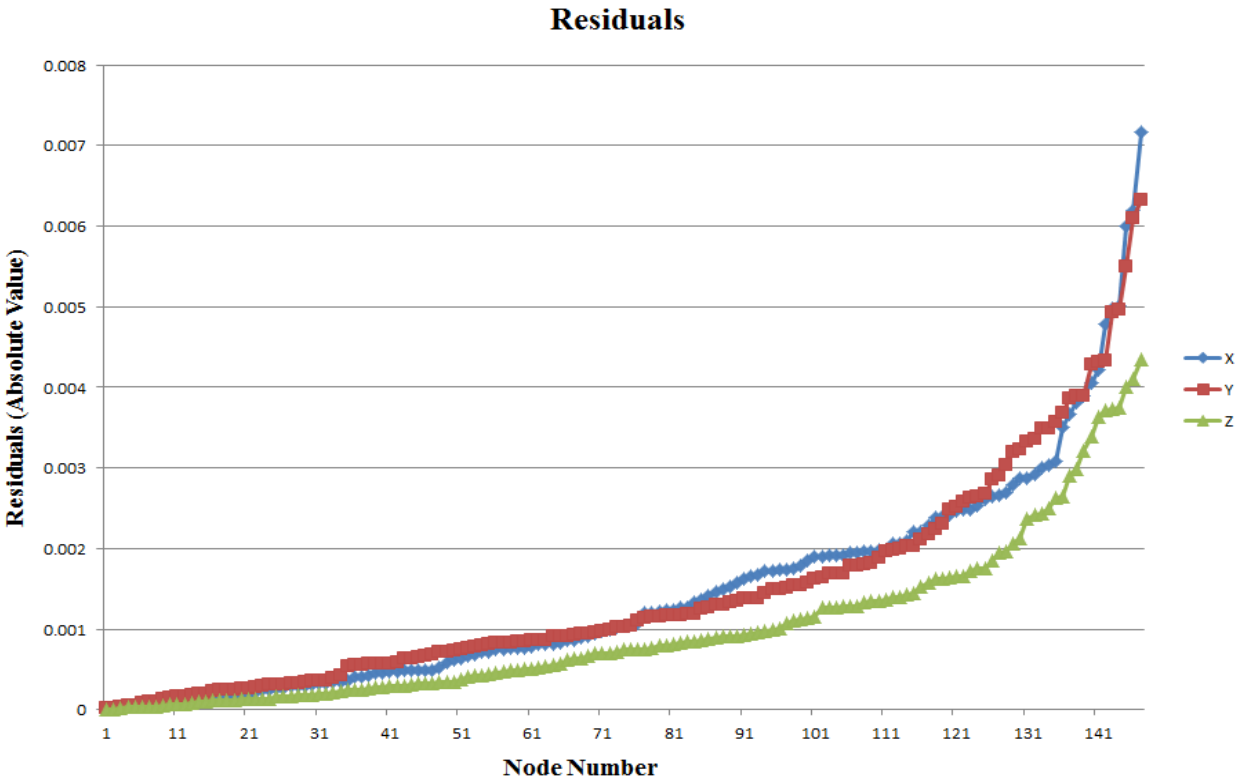

Figure 4-8 – Residuals of the Hybrid equations

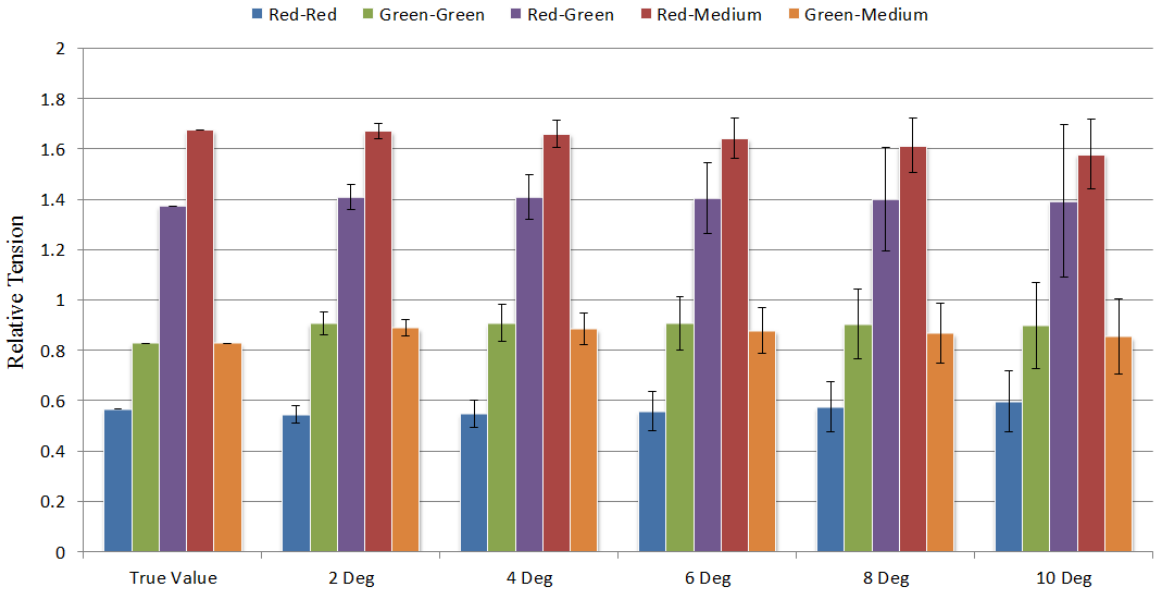

Figure 4-9 – Introducing noise to the S-type synthetic model (45 slices). The level of error for 6 and 10 degrees of noise are 2.6% and 5.5% respectively.

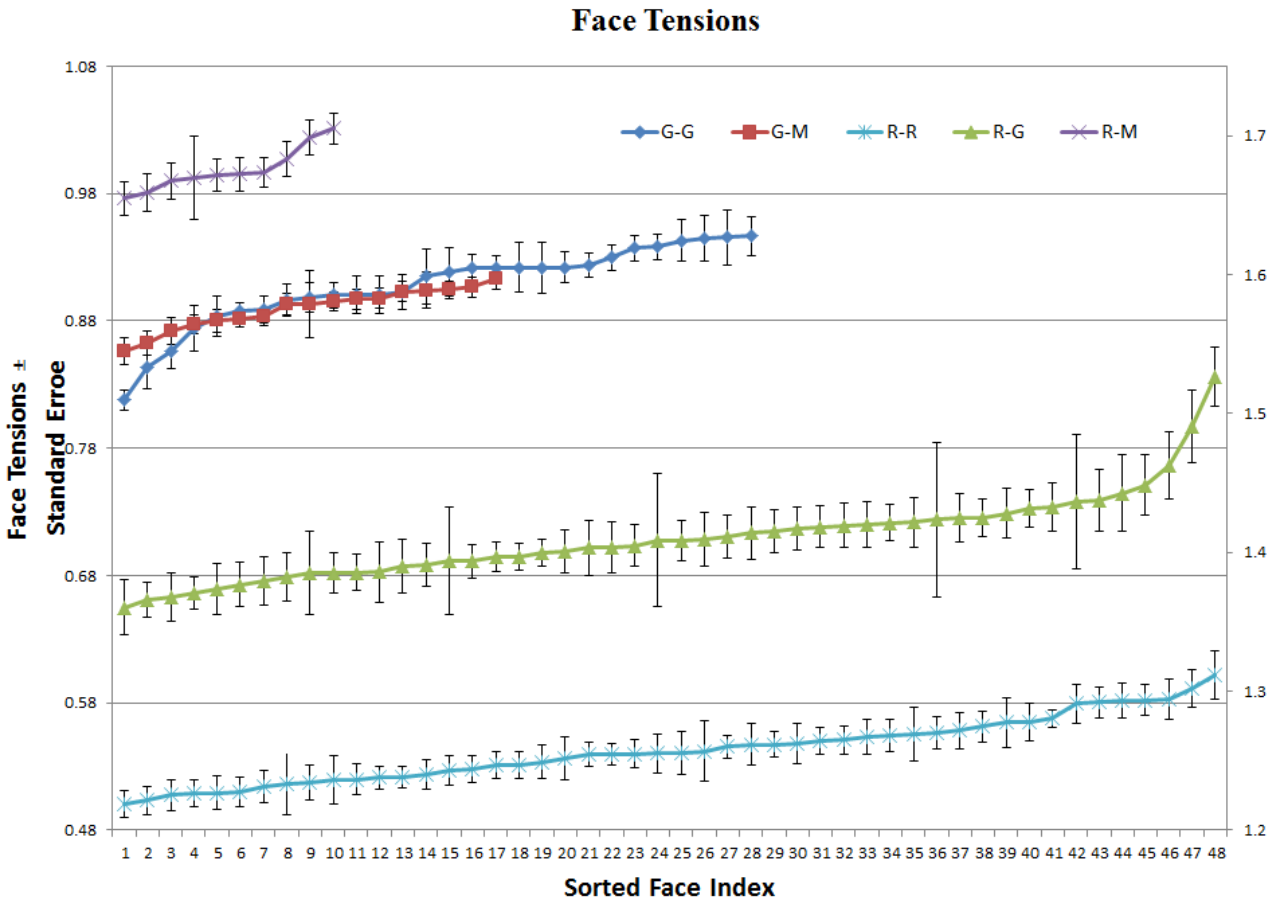

Figure 4-10 – Calculated face tensions with standard error are shown for each face type. The Red-Medium and Red- Green curves are drawn according to the secondary axis on the right.

4.5 Slicing Along Two Different Vectors

To verify that the accuracy of the results is independent of the direction at which the stack is made, we created a 45 slice S-type synthetic model sliced along the Z and Y axes. This model has an average of 13 slices per cell which is consistent with models generated with confocal microscopes. Figure 4-11 compares the result found for the same model sliced along two different axes. The maximum observed error for all methods was %4. This error is

greatest when the vectors make an angle around 90°and decrease as we move toward either end.

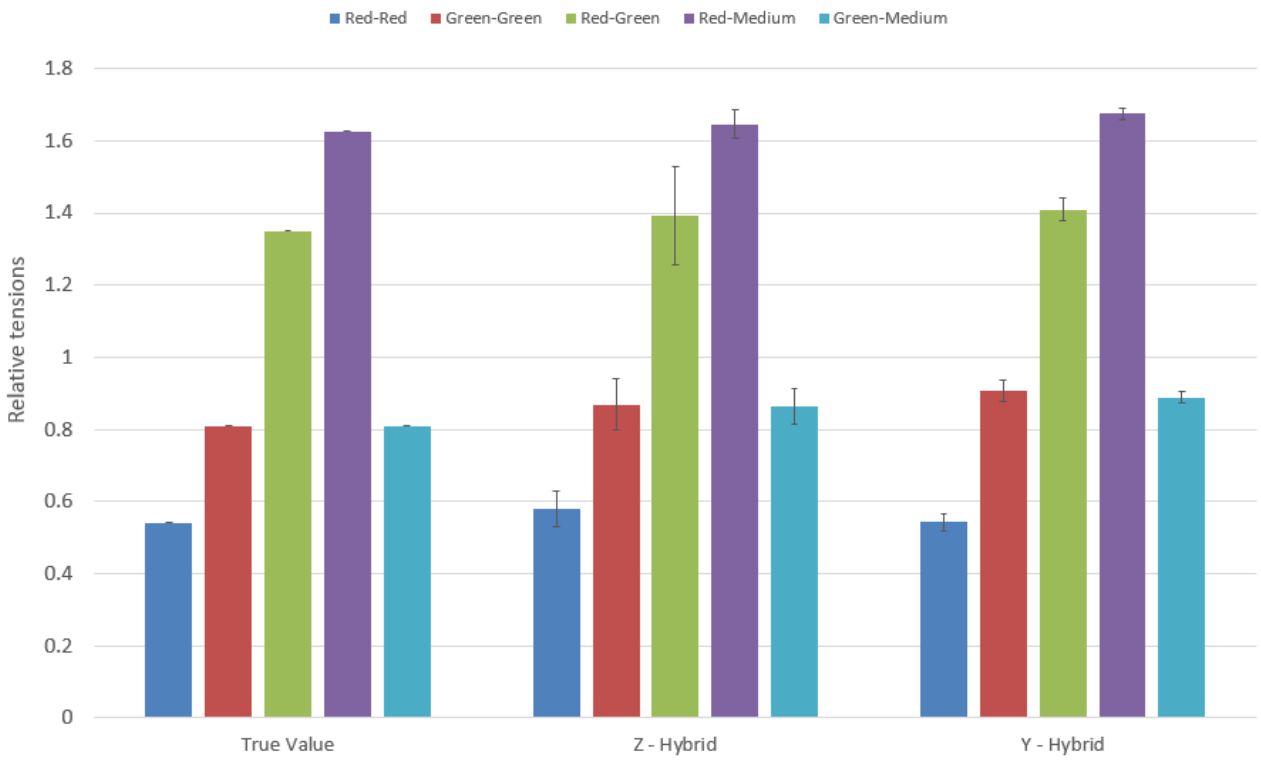

Figure 4-11 – Results for the three approaches applied to an S-type synthetic model with 45 slices, along Z and Y axes.

4.6 Optimal Number of Slices

It is obvious that the number of SPC has a direct impact on the accuracy of obtained results. However, it also directly determines the total number of images that need to be taken which can easily increase to tens of hours of imaging work on a confocal microscope. Therefore, it is important to find the most feasible spacing which obtains the best achievable results. To find the optimal value, we tried different spacing generating from 20 to 100 slices

(average SPC of 6 to 30) through the aggregate on S-type synthetic model. Then the results of each case were compared with true values (Figure 4-12). In order to be able to generalize these result to aggregates with a different number of cells or different cell sizes, we introduced a parameter called average number of slices per cell. In the case where cell volumes are of the same order, this parameter can be calculated by dividing the average cell diameter by spacing. However, this formula might not be applicable for cases involving large deviations in cell volumes.

The root mean square (RMS) of the results shows that an average SPC of 13 (equal to 45 sections for the whole aggregate in our case) and over, generates the best possible results (within 6% of the true values). It also illustrate that increasing the average SPC beyond 15 has less effect on the accuracy. A model with an average SPC of 6 or less would introduce a large amount of error in the obtained tensions. Our experiments also show that for models with an average SPC smaller than 8, the grouping process (the process by which the code finds sections of a specific cell through spatial images) of digitized slices becomes very difficult.

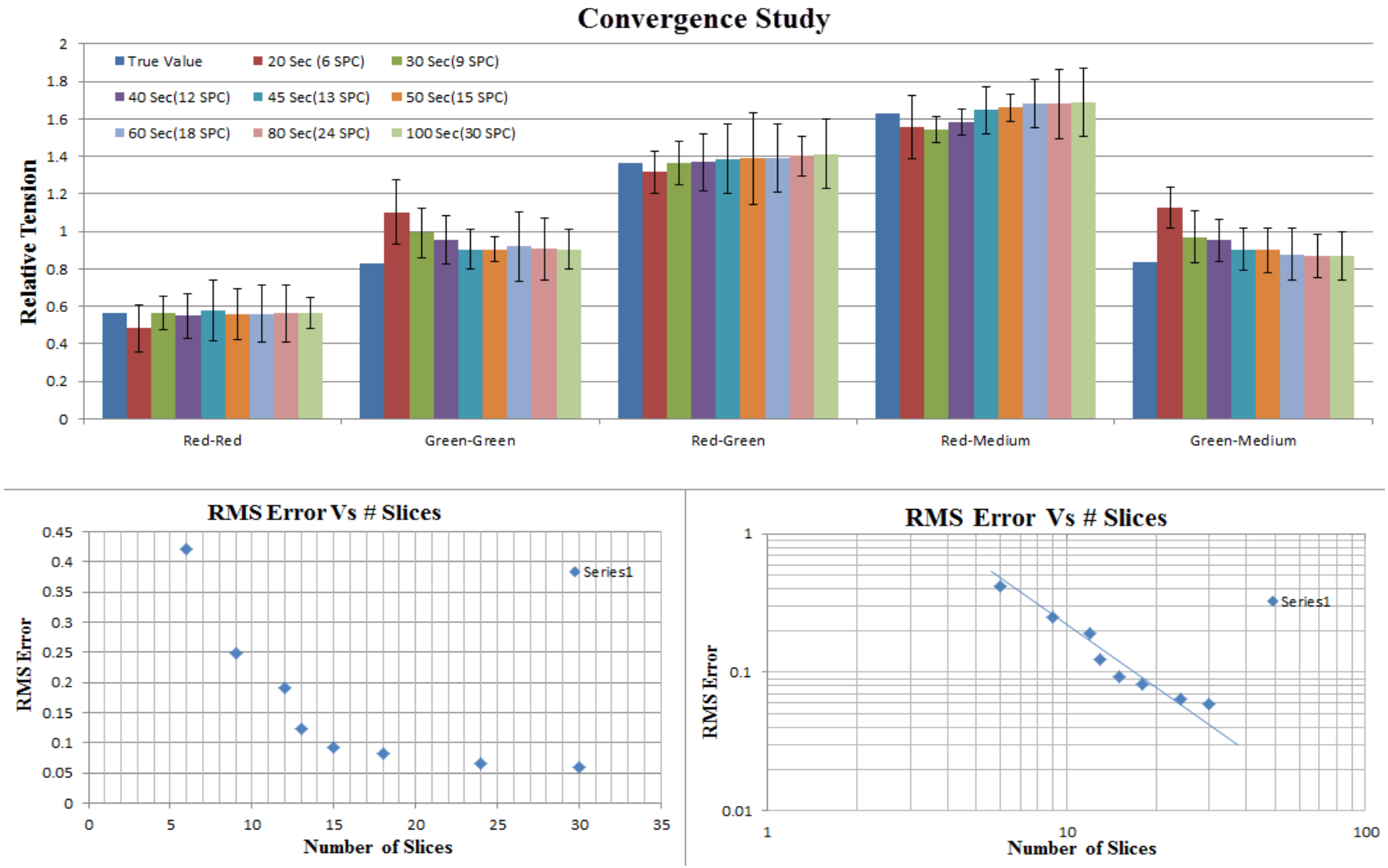

Figure 4-12 – Convergence result of the number of cuts per cells.

4.7 Analysis of Biological Data

Mechanical forces play an important role in a wide range of biological processes including embryo development, wound healing, cancer invasion and tissue engineering (Walgenbach, Voigt et al. 2001, Trinkaus 1984, Nodder, Martin 1997, Chaffer, Weinberg 2011). Knowledge of the underlying mechanical forces driving cell and tissue motions is an important part of understanding how these systems work. Being able to infer cellular forces from the 3D shapes of cells is an important step in correctly figuring out the basic mechanics of cell and tissue reshaping as well as identifying the effects that these forces have on mitosis, gene expression and differentiation.

To demonstrate the power of this method, we used it to investigate cell segregation during zebrafish gastrulation. Cell segregation is the process whereby epiblast cells internalize and become mesoderm cells (Figure 4-13).

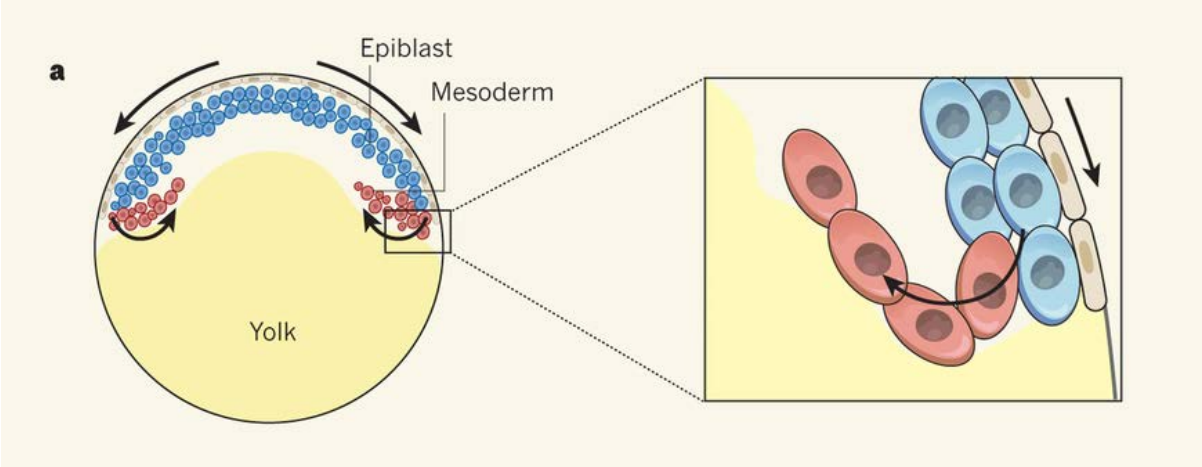

Figure 4-13 – Cell Segregation – epiblast cells either stay on the outside and become ectoderm cells or internalize and become mesoderm cells (shown in red)

Zebrafish is a popular animal model among medical scientists and biological researchers. Their genes have been sequenced and studied in detail and many clones and mutants exist.

Also, zebrafish embryos are see-through which facilitates observing morphological changes such as cell sorting and migration through its development (Detrich, Westerfield et al. 2011).

Zebrafish are notable for their high regenerative ability. During the spawning process, the female fish lays hundreds of eggs in the interval of two to three hours which provides many sample for scientist to work on. The fertilized eggs become transparent almost immediately which make them more desirable for research purposes. The generation time of zebrafish is approximately three month which is very short comparing with many other animals. Zebrafish adults are small in size and they tend to live together in shoals. Consequently, it is cost effective to use them for the research purposes. Also, zebrafish are more similar to humans than other invertebrates such as worms *Caenorhabditis elegans* and fruit flies *Drosophila Melanogaster* which makes them suitable research models to investigate human development and diseases.

Zebrafish gastrulation is an embryonic development process which leads to formation of three cell layers – the ectoderm, mesoderm and endoderm (Figure 4-14). Gastrulation is the first large-scale morphogenetic process to occur during zebrafish development and has three major features: epiboly, the spreading and thinning of cell layers; internalization of mesoderm and endoderm progenitors; and convergent extension, the narrowing and extension of the body axis (Rohde, Heisenberg 2007). The zebrafish embryo is initially a single blastomere connected to a large yolk cell. Successive cell divisions form a large blastoderm that remains situated on top of the yolk cell. An epithelial monolayer, called the enveloping layer (EVL), forms and completely covers the underlying blastomeres, serving as a protective outer surface.

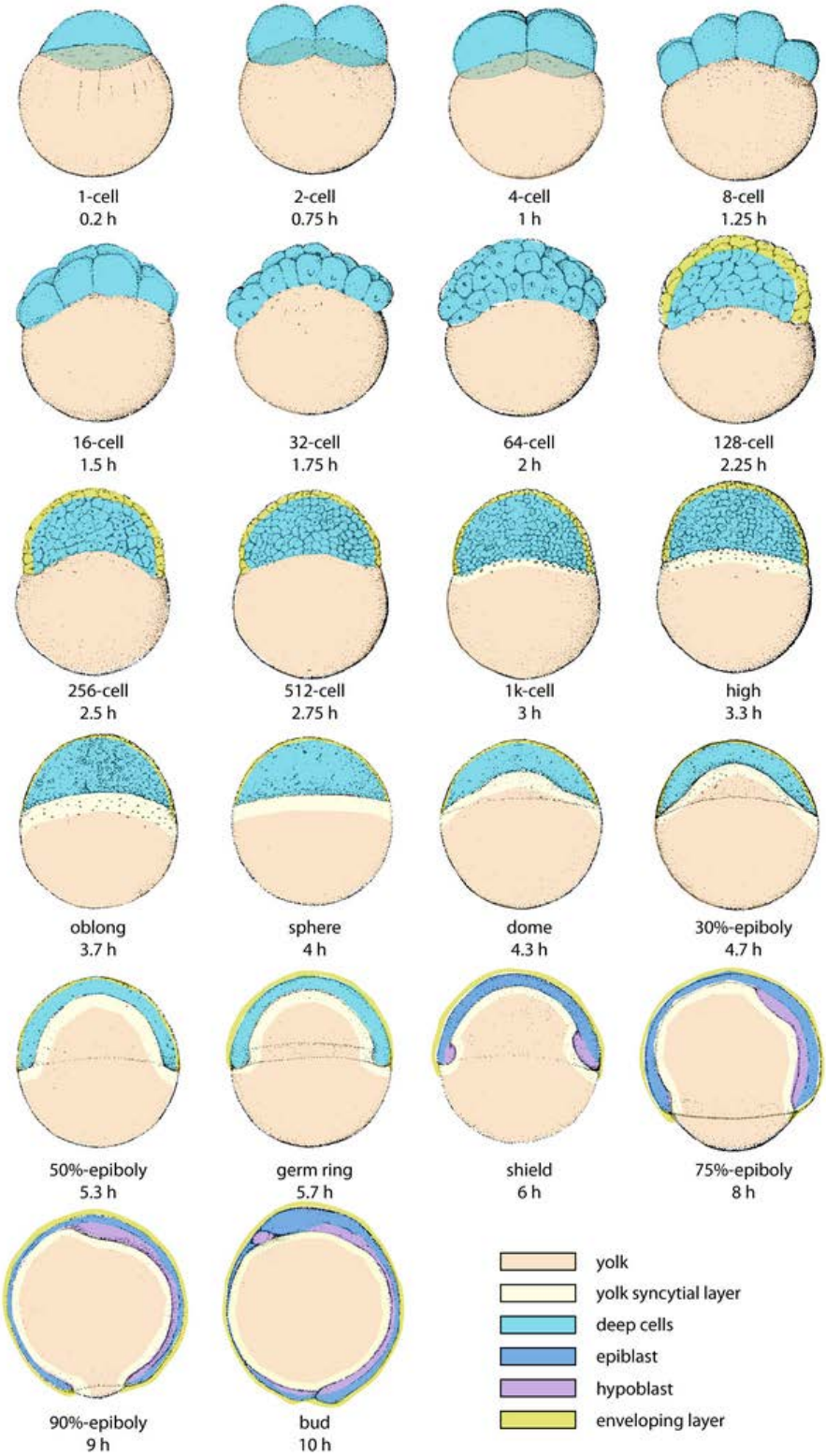

Figure 4-14 – Zebrafish early developmental stages (Kimmel, Ballard et al. 1995).

During epiboly the blastoderm thins and the yolk cell bulges upwards. Eventually the thinning blastoderm spreads past the equator of the embryo. After epiboly covers 50% of the yolk cell cells start to internalize and form the mesoderm and endoderm (Figure 4-13). The cell movements of convergent extension begin at the same time as internalization at 50% epiboly.

The processes and forces directing cell internalization are not yet understood (Krens, Heisenberg 2011). To investigate these forces we worked with biological collaborators Gabby Krens and C.P. Heisenberg, from the Institute of Science and Technology (IST) Austria. A first step was to look at the forces driving ectoderm and mesoderm cell motions in culture (*in vitro*). Ectoderm and mesoderm cells were isolated and collected from zebrafish embryos and then mixed together. Time-lapse confocal image stacks were then collected of these aggregates while the cells moved and rearranged. Details of the embryo preparation are as follows: Injected zebrafish embryos were kept at 28 – 31 °C until they were dissociated into single cells at sphere-stage (4 hpf). Cell sorting experiments were performed as described (Klopper, Krens et al. 2010), with the following modifications: micro-molds with a diameter of ± 400 μm and a height of ± 800 μm were made from a PDMS negative obtained from microtissues.com (http://www.microtissues.com/) according to the suppliers guidelines. The agarose (2 %) micro-mold gel was equilibrated for at least 4 h with 4 mL of CO2- independent DMEM/F12 medium (Invitrogen, containing L-Glut, 15mM Hepes, and 100U/mL penicillin and streptomycin and adjusted to pH 7.5) at 31 °C. The different germ layer progenitor cell types were isolated and mixed by first removing the embryo animal pole of an equal number of mesoderm and ectoderm induced embryos (see

above). The pooled animal poles were dissociated to a homogeneous single cell mix by gently tapping the tube. The cell mixture was then seeded on the micro-wells, and their sorting was recorded in 8 - 9 of the 256 micro-wells for at least 5 h in 3D over time at 28.5 °C by acquisition of 4 µm-spaced z-stacks of the aggregate in 2 - 3 channels every 5 min, using a Leica SP5 confocal microscope equipped with a Leica 25x 0.95NA dipping lens.

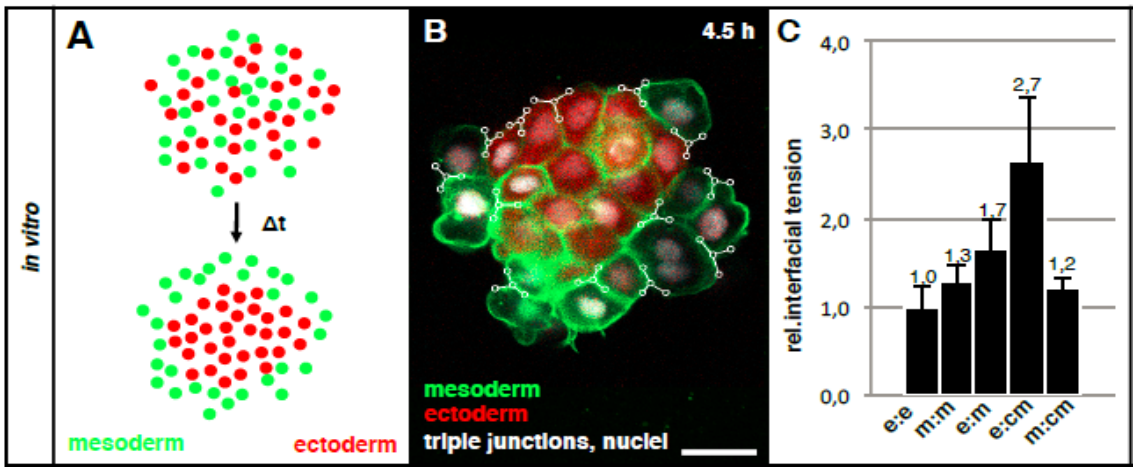

Figure 4-15 – Tension calculation on same cell types by our collaborators. (A) In the first step, cells were led to sort out completely. (B) Once they stopped moving the angle calculation were performed. (C) The TJ equations were solved with ratio solver.

The mixed ectoderm and mesoderm cells sort out according to their relative interfacial and surface tensions such that the mesoderm cells go the outside and surround the ectoderm cells. Schematic illustrations of the starting and end configurations for a typical in vitro sorting assay are shown in Figure 4-15A. A single confocal image plane of a typical aggregate is shown in Figure 4-15B. Five types of interfaces are present in these experiments depending on whether a cell is touching another cell of a same or different type or touching the surrounding liquid medium: ectoderm-ectoderm (e-e), mesoderm-mesoderm (m-m),

ectoderm-mesoderm (e-m), ectoderm-cell medium (e-cm), and mesoderm-cell medium (m-cm). Tensions were calculated and averaged from more than 6 sorting experiments using a version of CellFIT-3D like the one presented here except that interface tangent vectors were digitized manually. Resulting tensions are shown in Figure 4-15C.

Details of our force inference process for a single experiment – using the fully automated digitization process -- are shown below. An aggregate with 24 cells was digitized (Figure 4-16).

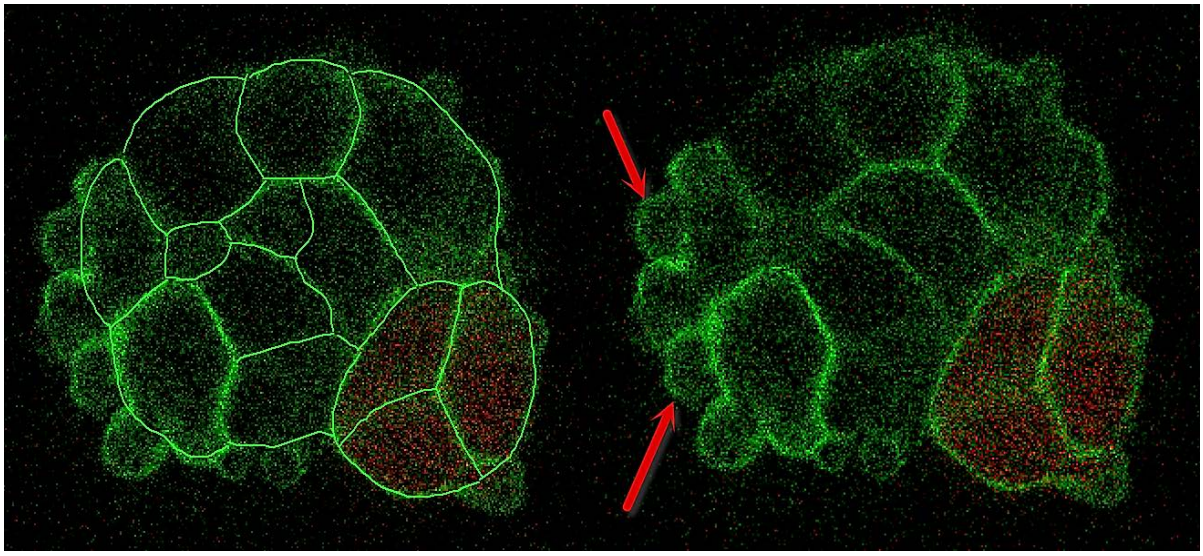

Figure 4-16 – Protrusions on cell membranes. Protrusions were smoothed out through a digitizing process. Since the edges are not clearly visible, this process will introduce some error in calculating the Young angles.

There are several factors that affect the digitization process and make it challenging. Cell blebs and protrusions need to be ignored and lack of clarity or detail in the imaging of cell boundaries sometimes makes it difficult to determine where exactly the boundaries lie (Figure 4-16).

Once digitization was performed on all the images in the z-stack they were assembled and cells associated between slices (Figure 4-17).

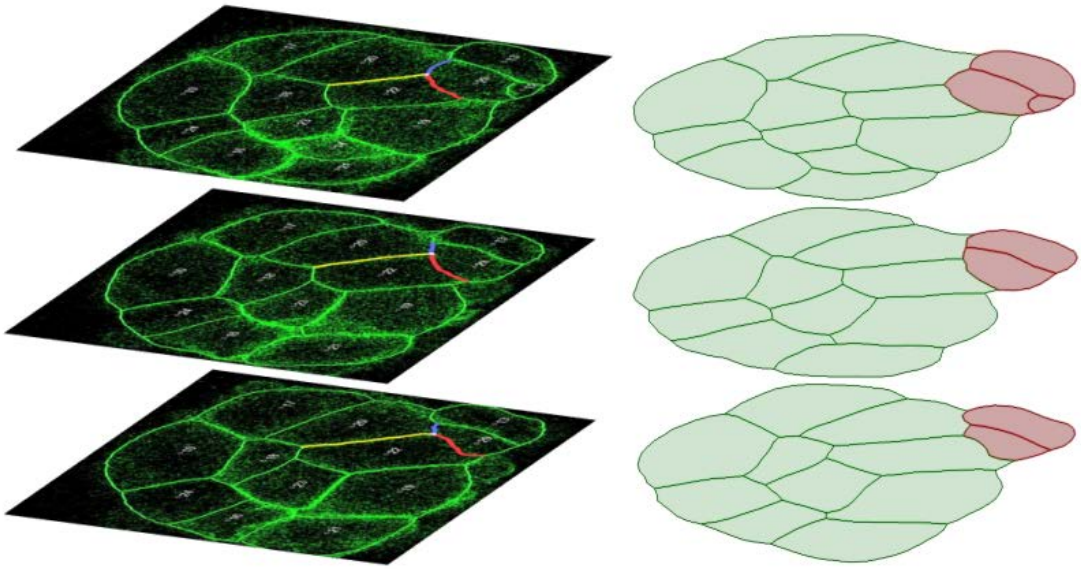

Figure 4-17 – Digitized and assembled slices.

Equations were then constructed and tensions solved for. Figure 4-18 shows the result of the three different approaches for this data set as well as the averaged tension values from the manual CellFIT-3D analyses. Sphere fitting was the least accurate of the methods. Our investigation revealed that for some twisted internal faces, it was not possible to find a well matched sphere and as a result the associated tension vectors had a high amount error. The point projection method, on the other hand, does not attempt to fit any specific shape in order to calculate the angles and so achieved more accurate values for the face tensions. Compared to the averaged results from multiple data sets using the manual CellFIT-3D approach - these results for a particular data set are similar and within the range of test to test variability.

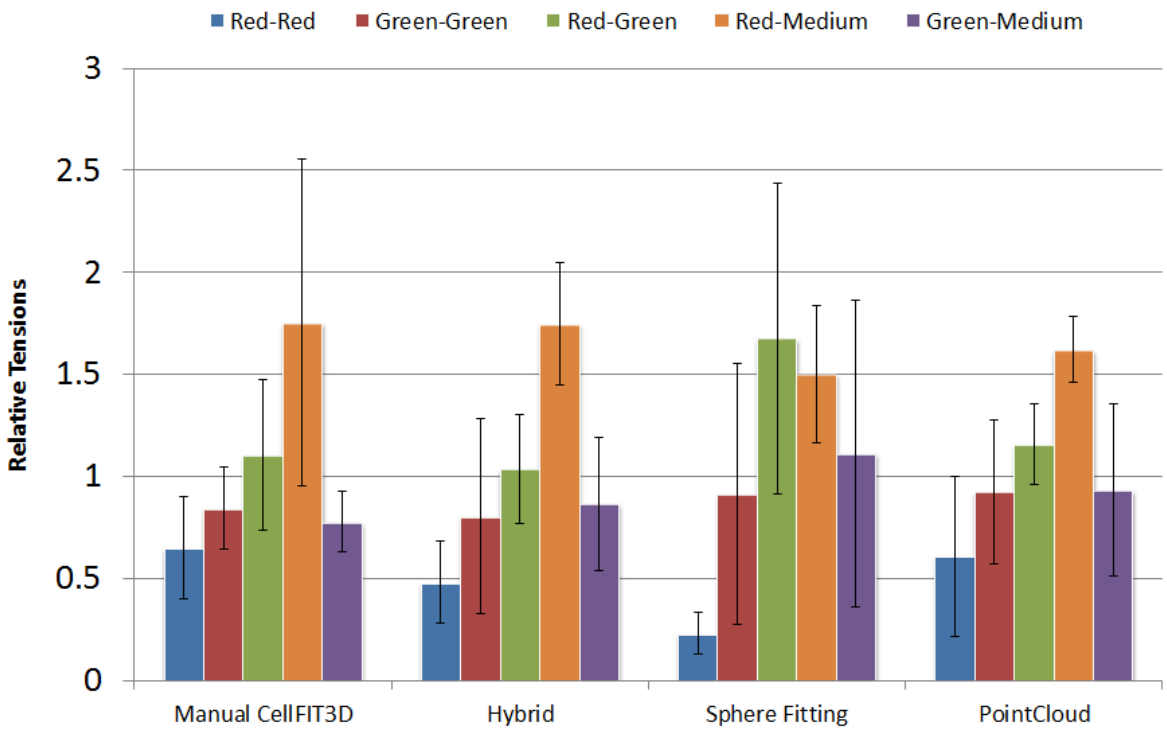

Figure 4-18 – Comparing results of our collaborators with results of our method

To investigate the accuracy and reliability of the calculated results we can look at the calculated residuals (Figure 4-19) and standard errors (Figure 4-20). The residuals are obtained using Equation (15 from Section 3.3.2. For each data, the directional components of the residual are converted into a single curve by obtaining the square root value for each point. The residuals are shown in ascending sorted order. The residuals of this biological data are low when compared with the synthetic data reported in section 4.4 and shown in Figure 4-19. This indicates that the estimated tensions satisfy the original equations well. Finally, Figure 4-20 shows the standard errors associated with each face tension. They are shown in ascending order according to interface type and are calculated as described in Section 3.3.2. The standard errors are fairly large but within expected experimental variability.

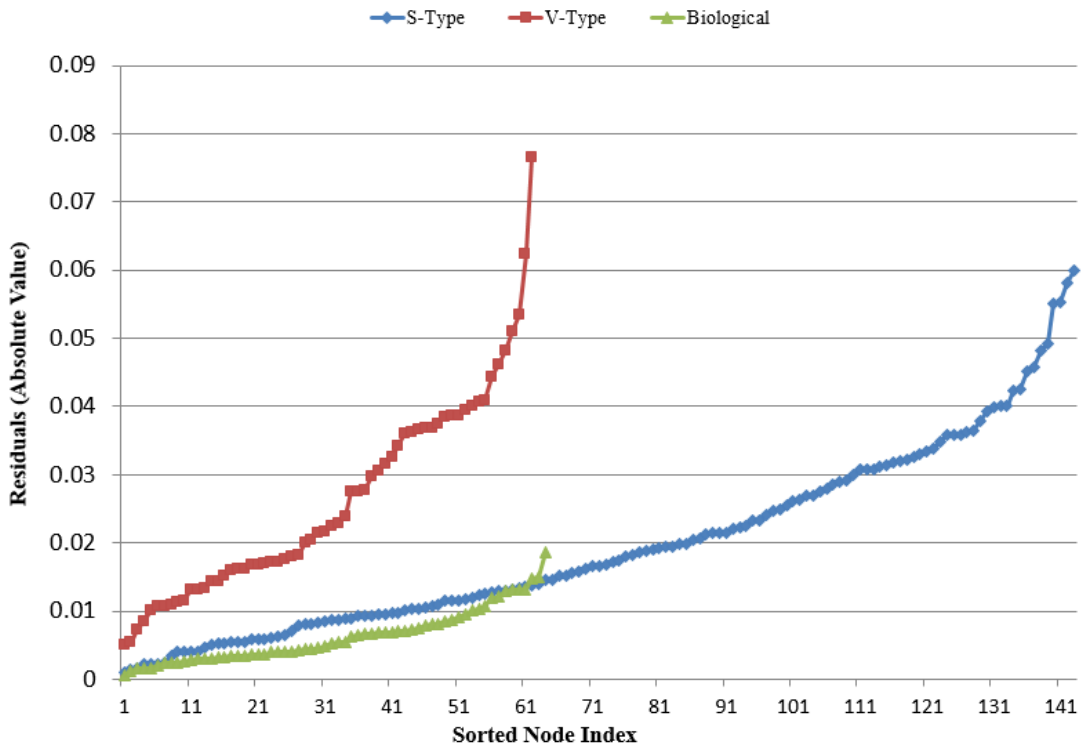

Figure 4-19 – Comparing residuals of hybrid method for biological data and two synthetic models.

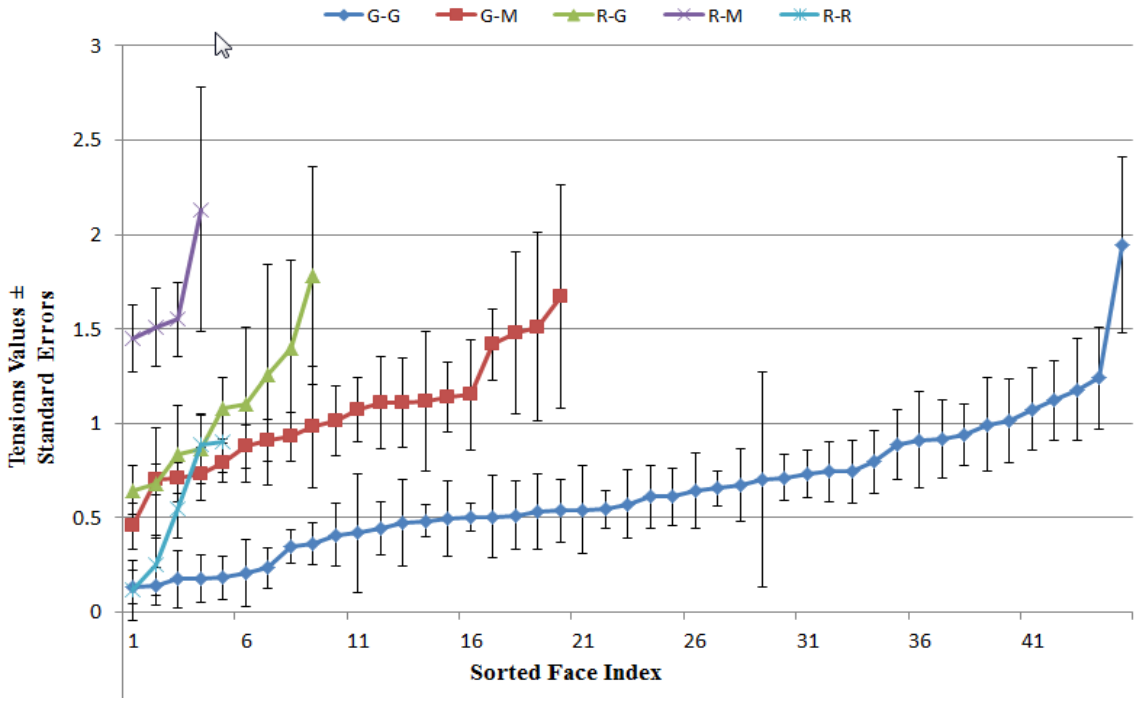

Figure 4-20 – Standard error for all faces.

These force results can also be compared to two other methods used for calculating tensions on these cell types. The first method involves using AFM indentation to extract cell-cortex tensions (Krieg, Arboleda-Estudillo et al. 2008). In this technique cell-cortex tension was measured by deforming the surface of single cells with a colloidal force probe and recorded the resulting force-indentation curves with an AFM (Figure 4-21). Cell-cortex tension was extracted from force-indentation curves using the cortical shell-liquid core or liquid droplet model (Krieg, Arboleda-Estudillo et al. 2008). Distribution of the recorded tensions for ectoderm, endoderm and mesoderm progenitor cells are shown in Figure 4-22.

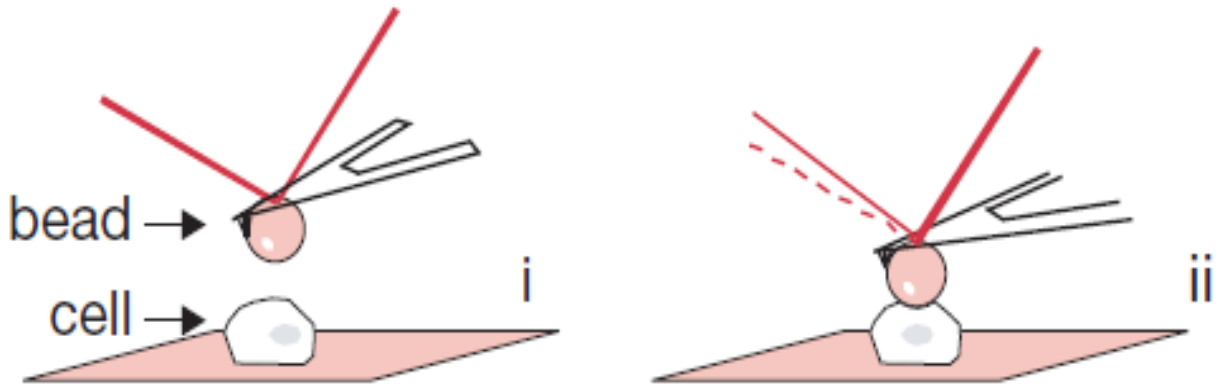

Figure 4-21 – AFM setup for cell-cortex tension measurements (Krieg, Arboleda-Estudillo et al. 2008).

The AFM measurement compares the tension of each cell type with the corresponding group control and as a result it is only possible to compare the medium faces of mesoderm and ectoderm cells. The AFM method produced results showing that the ectoderm-medium face tensions (red-medium) are 1.6 times higher than the mesoderm-medium ones.

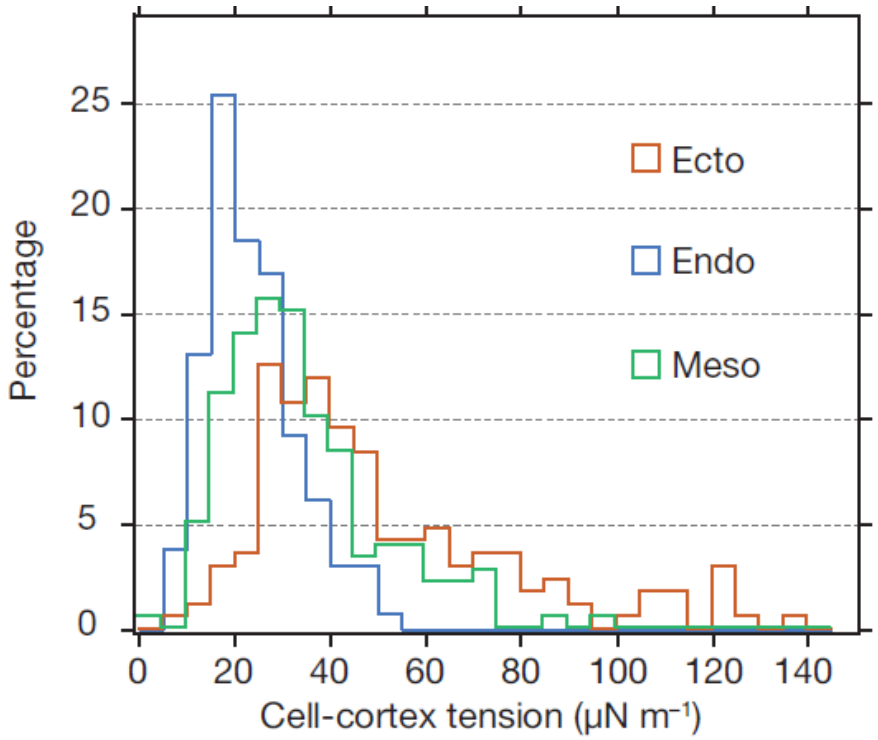

Figure 4-22 – Measured tensions of three progenitor cells

The second method of calculating cell face tensions involves looking at contact angles of cell doublets (Figure 4-23A) and pulling on them using a dual pipette aspiration assay and analyzing cell shapes directly after separation (Figure 4-23B and C) (Maitre, Berthoumieux et al. 2012). In this approach, the ratios of γ_{cc}/γ_{cm} can be calculated. The pipette aspiration experiments produced results where the ratio of γ_{cc}/γ_{cm} for ectoderm cells equals 0.5 and for mesoderm cells equals 0.65.

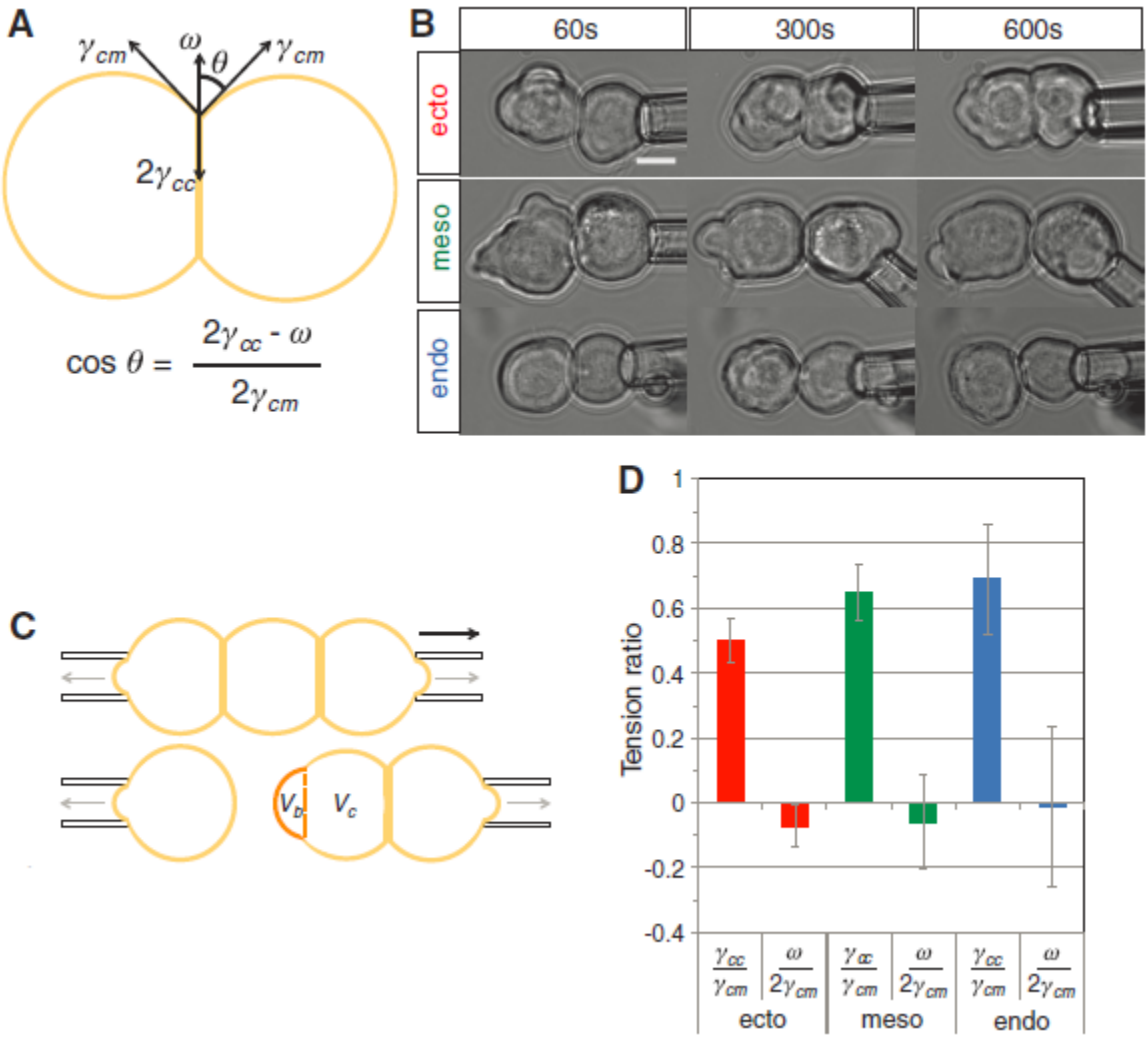

Figure 4-23 – Micropipette aspiration method reports the relative cortex tensions.

Comparing the interfacial tension results of our CellFIT-3D approach on mesoderm and ectoderm sorting experiments with the AFM results on single cells shows that both techniques find the correct tension order for cell-medium cortex tensions. That is, the ectoderm-medium tensions are higher than mesoderm-medium ones. However, the ratio that each approach reports is different. The hybrid results show that ectoderm-medium tensions

are 2.25 times higher than the mesoderm-medium ones while the AFM approach finds this ratio to be 1.6.

When comparing the results our CellFIT-3D approach with the micropipette aspiration experiments on cell doublets and triplets, we find some even greater differences. The micropipette approach reported ratios of 0.5 for ectoderm cells compared to 0.37 for the cellFIT-3D method. For mesoderm cells the micropipette approach reported 0.65 compared to the cellFIT-3D results of 1.08. These results are normalized and summarized in Figure 12.

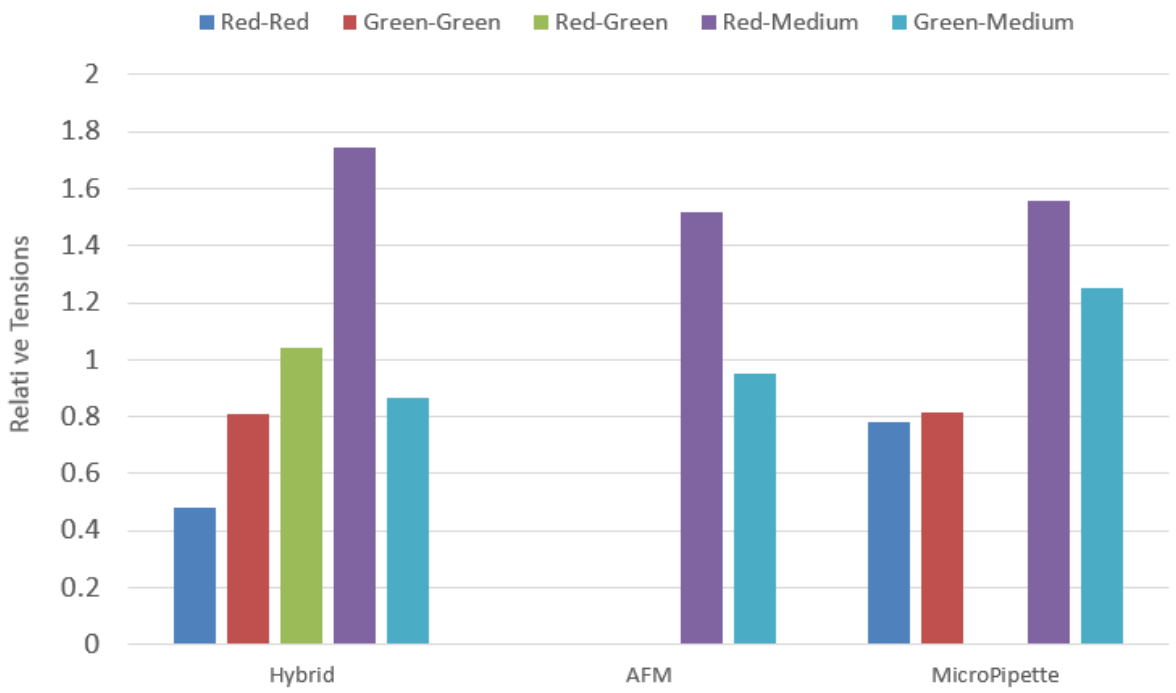

Figure 4-24 – Comparing results of Hybrid approach on Biological data with AFM and Micropipette reported tensions.

Considering that each approach was carried out on different set of cells with very different protocols and assumptions, we expect to see some difference in the reported answers. A more

careful look at the underlying assumptions in each approach may be helpful in understanding these differences.

As discussed in Section 2.1.3, tensions in the membrane are known to be responsible sorting and engulfment. Here, we try to investigate how our results match to the theories describing these movements. Mesoderm and ectoderm progenitor cells of zebrafish have been observed to sort out from each other in these *in vitro* experiments. The mesoderm cells also tend to engulf the ectoderm cells. In many of the experiments the mesoderm cells totally engulf the ectoderm cells. Sometimes, like in the biological data example reported in this section, only partial engulfment occurs. For the engulfment to happen certain tension configuration needs to be satisfied. According to the DITH, for the total engulfment to occur, the following equation must be satisfied:

$$\gamma_{e-m} < \gamma_{e-M} - \gamma_{e-M}$$

where e is ectoderm, m is mesoderm, and M is liquid medium. The above equation is sufficient for total engulfment to occur. The condition for partial engulfment is as follows:

$$\gamma_{e-m} < \gamma_{e-M}$$

For different cell types to sort out from each other, the DITH says that tension of heterotypic faces should be greater than the average tension of homotypic ones. That is:

$$\gamma_{e-m} > \frac{\gamma_{e-e} + \gamma_{m-m}}{2}$$

Substituting the tensions obtained from the hybrid CellFIT-3D method into the equations above we see that they only satisfy the partial engulfment condition but not the total

engulfment condition which is consistent with our observations. The sorting condition is also satisfied, again consistent with observed behaviour.

Next steps in investigating cell segregation during zebrafish gastrulation involve looking at the internalizing cells in living embryos (*in vivo*). Initial force inference results suggest that forces and mechanisms are very different when comparing the cells in culture versus in living embryos. This is evident in that in the *in vitro* sorting experiments the mesoderm cells sort to the outside with the ectoderm cells on the inside – which is the opposite of the sorting behaviour *in vivo* where the mesoderm cells move to the inside.

Chapter 5
Conclusion and Future Directions

As this research has demonstrated, it is possible to successfully develop a method to extend the 2D CellFIT approach to 3D and thereby to calculate the tensions that act along individual cell-cell and cell-membrane edges in 3D aggregates.

Several approaches were considered for calculating the angles between adjacent faces. These included fitting spheres to the point clouds associated with particular edges and local plane fitting along the edges of point clouds. Sphere fitting worked best on cell-medium faces and local plane fitting was best for internal faces. A hybrid approach in which the more accurate representation for each face type is used gave the best overall results. When a sufficient number of sections (image slices) pass through each cell, tests on synthetic data suggested that the edge forces can be found to within 6% of their true values. If the 3D nature of the aggregate is ignored and a 2D approach is applied instead to individual sections, analyses based on synthetic data suggest errors in the order of 35%. In the presence of noise, poor image quality and other inevitable factors associated with experimental data, even greater error would be expected.

The density of the points in the point clouds used to carry out the fitting of spheres and other geometries is dependent on the spacing of the confocal sections; closer sections giving higher point densities. If cells have on average 7 sections, a section spacing consistent with that needed for automated cell reconstruction (Kin Shun Leung, Veldhuis 2010), then force

estimates in the order of 25% can be obtained. However, improvements continue to be realized up to 15 sections per cell, a number that seems excessive today, but may be quite practical to obtain in the future as imaging techniques advance.

The presented technique here, is only applicable to static aggregates in which cells do not undergo morphogenetic changes such as mitosis. Considering the static condition satisfied, any region of interest can be separately analyzed for the cases where comp the geometry of the whole aggregate is not available.

When applied to confocal image sets obtained from experiments, CellFIT-3D was able to clearly distinguish differences in the forces acting along different types of cell boundaries, information that is fundamental to understanding why cells move and reshape. The tensions obtained using CellFIT-3D were consistent with those estimated using other experimental techniques. Only with information of this kind can one truly understand why embryos reshape as they do, why cancer cell sometimes migrate so as to produce metastases and why cells of heterogeneous types in engineered tissues reorganize into physiological geometries or fail to do so.

In order to carry out the 3D analyses, a considerable amount of coding was developed, with the goal of developing a pipeline that could take in raw confocal images and produce force maps. Some of the steps in this process were quite complex and full automation was not achieved. The potential of the method is great and to reduce the amount of hand work needed to process confocal data sets, further work is warranted.

In particular, the watershed process that produces cell outlines from the confocal images needs further work. One reason is that it serves as the gateway for incoming data, the quality of which falls outside the control of the software. Edge tracing is also an inherently difficult process and when coupled with input data of variable quality becomes most difficult to achieve reliably. This is another area that merits further theoretical and computational attention. Finally, the algorithms that calculate the Young angles warrant further study. In order to fully automate the process proposed by the author, algorithms are needed so that the user does not have to manually identify which edges are on the interior and which on the exterior of the mass. Future algorithms might be able to automate the identification process or involve new fitting approaches that do not require this distinction to be made.

The current software was designed to operate in a software development environment and further refinements would be required for it to serve in a production environment. In addition to full automation, output information provided to assist with debugging and code optimization should be removed as it would not be helpful to end users of the software. The goal of the revisions should be to produce a pipeline that offers quality measures (Brodland, Veldhuis et al. 2014), so the user can know the degree of confidence that should be placed in the forces calculated by the algorithm.

This thesis has demonstrated that the forces acting along the edges of cells in 3D aggregates can be determined from confocal stacks if appropriate software is available, and the author hopes that in time CellFIT-3D will become a standard tool for learning about the mechanics of cells.

Bibliography

ADAM, N.K., 1968. *The Physics and Chemistry of Surfaces.* New York: Dover Publications.

ALBERTS, B., BRAY, D., HOPKIN, K., JOHNSON, A., LEWIS, J., ROBERTS, K., RAFF, M. and WALTER, P., 2014. *Essential cell biology. 4th Edition.* Fourth edn. New York: Garland Publishing Inc.

ALBERTS, B., BRAY, D., JOHNSON, A., LEWIS, J., MARTIN, R. and WALTER, P., 1998. *Essential Cell Biology.* New York: Garland Publishing Inc.

AMERICAN CANCER SOCIETY, 2015. *Cancer facts & figures 2015.* Atlanta: American Cancer Society.

ANDASARI, V., ROPER, R.T., SWAT, M.H. and CHAPLAIN, M.A., 2012. Integrating intracellular dynamics using CompuCell3D and Bionetsolver: applications to multiscale modelling of cancer cell growth and invasion. *PloS one,* **7**(3), pp. e33726.

ANON, E., SERRA-PICAMAL, X., HERSEN, P., GAUTHIER, N.C., SHEETZ, M.P., TREPAT, X. and LADOUX, B., 2012. Cell crawling mediates collective cell migration to close undamaged epithelial gaps. *Proceedings of the National Academy of Sciences of the United States of America,* **109**(27), pp. 10891-10896.

ARMSTRONG, P.B., 1989. Cell sorting out: The self-assembly of tissues in vitro. *Critical Reviews in Biochemistry and Molecular Biology,* **24**(2), pp. 119-149.

BAKER, P.C., 1965. Fine Structure and morphogenic movements in the Gastrula of the Treefrog, Hyla Regilla. *Journal of Cell Biology,* **24, no.1**, pp. 95-116.

BAKER, E.L., LU, J., YU, D., BONNECAZE, R.T. and ZAMAN, M.H., 2010. Cancer cell stiffness: integrated roles of three-dimensional matrix stiffness and transforming potential. *Biophysical journal,* **99**(7), pp. 2048-2057.

BAUSCH, A.R., MOLLER, W. and SACKMANN, E., 1999. Measurement of local viscoelasticity and forces in living cells by magnetic tweezers. *Biophysical journal,* **76**(1 Pt 1), pp. 573-579.

BENKO, R. and BRODLAND, G.W., 2007. Measurement of in vivo stress resultants in neurulation-stage amphibian embryos. *Annals of Biomedical Engineering,* **35**(4), pp. 672-681.

BEUCHER, S. and MEYER, F., 1992. Chapter 12: The morphological approach to segmentation: the watershed transformation. In: E.R. DOUGHERTY, ed, *Mathematical morphology in image processing.* New York: Marcel Dekker, Inc, pp. 433-481.

BODENSTEIN, L., 1986. A dynamic simulation model of tissue growth and cell pattering, *Cell Differentiation,* **19**, pp. 19-33.

BORGHI, N., SOROKINA, M., SHCHERBAKOVA, O.G., WEIS, W.I., PRUITT, B.L., NELSON, W.J. and DUNN, A.R., 2012. E-cadherin is under constitutive actomyosin-generated tension that is increased at cell-cell contacts upon externally applied stretch. *Proceedings of the National Academy of Sciences of the United States of America*, **109**, pp. 12568-12573.

BRAKKE, K.A., 2005-last update, The Surface Evolver.

BRODLAND, G.W., 2004. Computational modeling of cell sorting, tissue engulfment, and related phenomena: A review. *Applied Mechanics Review,* **57**(1), pp. 47-76.

BRODLAND, G.W. and CLAUSI, D.A., 1995. Cytoskeletal mechanics of neurulation: Insights obtained from computer simulations. *Biochemical Cell Biology*, **73**, pp. 545-553.

BRODLAND, G.W., SCOTT, M.J., MACLEAN, A.F., GLOBUS, M., VETHAMANY-GLOBUS, S., GORDON, R., VELDHUIS, J.H. and DEL MAESTRO, R., 1996. Morphogenetic movements during axolotl neural tube formation tracked by digital imaging. *Development Genes and Evolution,* **205**(5), pp. 311-318.

BRODLAND, G.W. and VELDHUIS, J.H., 2003. A computer model for reshaping of cells in epithelia due to in-plane deformation and annealing. *Computer Methods in Biomechanics and Biomedical Engineering,* **6**(2), pp. 89-98.

BRODLAND, G.W., 2006. Do lamellipodia have the mechanical capacity to drive convergent extension? *The International Journal of Developmental Biology,* **50**(2-3), pp. 151-155.

BRODLAND, G.W., 2002. The Differential Interfacial Tension Hypothesis (DITH): a comprehensive theory for the self-rearrangement of embryonic cells and tissues. *Journal of Biomechanical Engineering,* **124**(2), pp. 188-197.

BRODLAND, G.W., CHEN, D.I. and VELDHUIS, J.H., 2006. A cell-based constitutive model for embryonic epithelia and other planar aggregates of biological cells. *International Journal of Plasticity*, **22**(6), pp. 965-995.

BRODLAND, G.W. and CHEN, H.H., 2000a. The mechanics of cell sorting and envelopment. *Journal of Biomechanics*, **33**(7), pp. 845-851.

BRODLAND, G.W. and CHEN, H.H., 2000b. The mechanics of heterotypic cell aggregates: insights from computer simulations. *Journal of Biomechanical Engineering,* **122**(4), pp. 402-407.

BRODLAND, G.W., CHEN, X., LEE, P. and MARSDEN, M., 2010. From genes to neural tube defects (NTDs): insights from multiscale computational modeling. *HFSP journal*, **4**(3-4), pp. 142-152.

BRODLAND, G.W., CONTE, V., CRANSTON, P.G., VELDHUIS, J., NARASIMHAN, S., HUTSON, M.S., JACINTO, A., ULRICH, F., BAUM, B. and MIODOWNIK, M., 2010. Video force

microscopy reveals the mechanics of ventral furrow invagination in Drosophila. *Proceedings of the National Academy of Sciences of the United States of America,* **107**(51), pp. 22111-22116.

BRODLAND, G.W. and VELDHUIS, J.H., 2012. The mechanics of metastasis: insights from a computational model. *PloS one,* **7**(9), pp. e44281.

BRODLAND, G.W., VELDHUIS, J.H., KIM, S., PERRONE, M., MASHBURN, D. and HUTSON, M.S., 2014. CellFIT: a cellular force-inference toolkit using curvilinear cell boundaries. *PloS one,* **9**(6), pp. e99116.

BRODLAND, G.W., 2003. New information from cell aggregate compression tests and its implications for theories of cell sorting. *Biorheology,* **40**(1-3), pp. 273-277.

BRUGUES, A., ESTER, CONTE, V., VELDHUIS, J.H., GUPTA, M., COLOMBELLI, J., MUNOZ, J.J., BRODLAND, G.W., LADOUX, B. and TREPAT, X., 2014. Forces driving epithelial wound healing. *Nature Physics,* **advance online publication**.

BRUN, R.B. and GARSON, J.A., 1983. Neurulation in the Mexican salamander (Ambystoma mexicanum): a drug study and cell shape analysis of the epidermis and the neural plate. *Journal of Embryology and Experimental Morphology,* **74**, pp. 275-295.

BURNSIDE, M.B. and JACOBSON, A.G., 1968. Analysis of morphogenetic movements in the neural plate of the newt *Taricha Torosa*. *Developmental Biology,* **18**, pp. 537-552.

CAMPAS, O., MAMMOTO, T., HASSO, S., SPERLING, R.A., O'CONNELL, D., BISCHOF, A.G., MAAS, R., WEITZ, D.A., MAHADEVAN, L. and INGBER, D.E., 2014. Quantifying cell-generated mechanical forces within living embryonic tissues. *Nature methods,* **11**(2), pp. 183-189.

CHAFFER, C.L. and WEINBERG, R.A., 2011. A perspective on cancer cell metastasis. *Science (New York, N.Y.),* **331**(6024), pp. 1559-1564.

CHEN, H.H. and BRODLAND, G.W., 2000. Cell-level finite element studies of viscous cells in planar aggregates. *Journal of Biomechanical Engineering,* **122**(4), pp. 394-401.

CHEN, X. and BRODLAND, G.W., 2008. Multi-scale finite element modeling allows the mechanics of amphibian neurulation to be elucidated. *Physical Biology,* **5**(1), pp. 015003.

CLARK, R.A.F.(.A.F. and HENSON, P.M.(.M., 1988. *Molecular and cellular biology of wound repair.* New York: Plenum Press.

CLAUSI, D.A. and BRODLAND, G.W., 1993. Mechanical evaluation of theories of neurulation using computer simulations. *Development,* **118**, pp. 1013-1023.

COOK, R.D. and YOUNG, W.C., 1999. *Advanced mechanics of materials.* 2 edn. Upper Saddle River, N.J.: Prentice Hall.

COWIN, S.C., 2000. How is a Tissue built? *ASME Journal of Biomechanical Engineering,* **122**, pp. 553-569.

DAHMANN, C., OATES, A.C. and BRAND, M., 2011. Boundary formation and maintenance in tissue development. *Nature reviews.Genetics,* **12**(1), pp. 43-55.

DAVIDSON, L.A., KOEHL, M.A.R., KELLER, R. and OSTER, G.F., 1995. How do Sea-Urchins Invaginate - using Biomechanics to Distinguish between Mechanisms of Primary Invagination. *Development,* **121**(7), pp. 2005-2018.

DETRICH, H.W., WESTERFIELD, M. and ZON, L.I., 2011. *The zebrafish : genetics, genomics and informatics.* Boston Mass. : Elsevier/Academic: Amsterdam Netherlands.

FUCHIZAKI, K., KUSABA, T. and KAWASAKI, K., 1995. Computer modelling of three-dimensional cellular pattern growth. *Philosophical Magazine B,* **71**(3), pp. 333-357.

GEIGER, T.R. and PEEPER, D.S., 2009. Metastasis mechanisms. *Biochimica et biophysica acta,* **1796**(2), pp. 293-308.

GLAZIER, J.A. and GRANER, F., 1993. Simulation of the differential adhesion driven rearrangement of biological cells. *Physical Review E. Statistical Physics, Plasmas, Fluids, and Related Interdisciplinary Topics,* **47**(3), pp. 2128-2154.

GOEL, N., CAMPBELL, R.D., GORDON, R., ROSEN, R., MARTINEZ, H. and YCAS, M., 1970. Self-sorting of isotropic cells. *Journal of theoretical biology,* **28**(3), pp. 423-468.

GORDON, R., GOEL, N.S., STEINBERG, M.S. and WISEMAN, L.L., 1972. A rheological mechanism sufficient to explain the kinetics of cell sorting. *Journal of theoretical biology,* **37**(1), pp. 43-73.

HARRIS, A.K., 1976. Is cell sorting caused by differences in the work of intercellular adhesion? A critique of the steinberg hypothesis. *Journal of theoretical biology,* **61**(2, pp. 267-285), pp. September.

HAYASHI, F., 2000. *Econometrics.* Princeton: Princeton University Press.

HONDA, H., 1983. Geometric models for cells in tissues. *International Review of Cytology,* **81**, pp. 191-248.

HONDA, H., 1978. Description of cellular patterns by Dirichlet domains: the two-dimensional case. *Journal of Theoretical Biology,* **72**, pp. 523-543.

HONDA, H., YAMANAKA, H. and EGUCHI, G., 1986. Transformation of a polygonal cellular pattern during sexual maturation of the avian oviduct epithelium: computer simulation. *Journal of embryology and experimental morphology,* **98**, pp. 1-19.

HUTSON, M.S., VELDHUIS, J.H., MA, X., LYNCH, H.E., CRANSTON, P.G. and BRODLAND, G.W., 2009. *Combining Laser Microsurgery and Finite Element Modeling to Assess Cell-Level Epithelial Mechanics.*

INGBER, D.E., 2003. Tensegrity II. How structural networks influence cellular information processing networks. *Journal of Cell Science*, **116**, pp. 1397-408.

ISHIHARA, S., SUGIMURA, K., COX, S.J., BONNET, I., BELLAICHE, Y. and GRANER, F., 2013. Comparative study of non-invasive force and stress inference methods in tissue. *The European physical journal.E, Soft matter*, **36**(4), pp. 9859-13045-8. Epub 2013 Apr 26.

JACOBSON, A.G. and GORDON, R., 1976. Changes in shape of the developing vertebrate nervous system analyzed experimentally, mathematically and by computer simulation. *Journal of Experimental Zoology*, **197**, pp. 191-246.

KARFUNKEL, P., 1970. The role of microtubules and microfilaments in neurulation in *Xenopus*. *Developmental Biology*, **25, Issue 1**, pp. 30-56.

KASZA, K.E., VADER, D., KOSTER, S., WANG, N. and WEITZ, D.A., 2011. Magnetic twisting cytometry. *Cold Spring Harbor protocols*, **2011**(4), pp. pdb.prot5599.

KELLER, R., DAVIDSON, L., EDLUND, A., ELUL, T., EZIN, M., SHOOK, D. and SKOGLUND, P., 2000. Mechanisms of convergence and extension by cell intercalation. *Philosophical Transactions of the Royal Society of London. Series B, Biological Sciences*, **355**(1399), pp. 897-922.

KELLER, R., 2006. Mechanisms of elongation in embryogenesis. *Development (Cambridge, England)*, **133**(12), pp. 2291-2302.

KIMMEL, C.B., BALLARD, W.W., KIMMEL, S.R., ULLMANN, B. and SCHILLING, T.F., 1995. Stages of embryonic development of the zebrafish. *Developmental dynamics : an official publication of the American Association of Anatomists*, **203**, pp. 253-310.

KIN SHUN LEUNG, T. and VELDHUIS, J.H., 2010. Identifying same-cell contours in image stacks: A key step in making 3D reconstruction. *Annals of Biomedical Engineering*, .

KLOPPER, A., KRENS, G., GRILL, S. and HEISENBERG, C., 2010. Finite-size corrections to scaling behavior in sorted cell aggregates. *The European physical journal E, Soft matter*, **33**, pp. 99-103.

KRENS, S.F. and HEISENBERG, C.P., 2011. Cell sorting in development. *Current topics in developmental biology*, **95**, pp. 189-213.

KRIEG, M., ARBOLEDA-ESTUDILLO, Y., PUECH, P.-., KÄFER, J., GRANER, F., MÜLLER, D.J. and HEISENBERG, C.-., 2008. Tensile forces govern germ-layer organization in zebrafish. *Nature Cell Biology*, **10**(4), pp. 429-436.

KUMAR, S. and WEAVER, V.M., 2009. Mechanics, malignancy, and metastasis: the force journey of a tumor cell. *Cancer metastasis reviews,* **28**(1-2), pp. 113-127.

KWIESIELEWICZ, M., 1996. The logarithmic least squares and the generalized pseudoinverse in estimating ratios. *European Journal of Operational Research,* **93**(3), pp. 611-619.

LECUIT, T. and LENNE, P.F., 2007. Cell surface mechanics and the control of cell shape, tissue patterns and morphogenesis. *Nature reviews.Molecular cell biology,* **8**(8), pp. 633-644.

LECUIT, T., LENNE, P.F. and MUNRO, E., 2011. Force generation, transmission, and integration during cell and tissue morphogenesis. *Annual Review of Cell and Developmental Biology,* **27**, pp. 157-184.

LEE, C., SCHERR, H.M. and WALLINGFORD, J.B., 2007. Shroom family proteins regulate gamma-tubulin distribution and microtubule architecture during epithelial cell shape change. *Development (Cambridge, England),* **134**(7), pp. 1431-1441.

LEGANT, W.R., MILLER, J.S., BLAKELY, B.L., COHEN, D.M., GENIN, G.M. and CHEN, C.S., 2010. Measurement of mechanical tractions exerted by cells in three-dimensional matrices. *Nature methods,* **7**(12), pp. 969-971.

LEWIS, W.H., 1947. Mechanics of invagination. *Anatomical Record,* **97**, pp. 139-156.

MAITRE, J.L., BERTHOUMIEUX, H., KRENS, S.F., SALBREUX, G., JULICHER, F., PALUCH, E. and HEISENBERG, C.P., 2012. Adhesion functions in cell sorting by mechanically coupling the cortices of adhering cells. *Science (New York, N.Y.),* **338**(6104), pp. 253-256.

MARTIN, A.C., KASCHUBE, M. and WIESCHAUS, E.F., 2009. Pulsed contractions of an actin-myosin network drive apical constriction. *Nature,* **457**, pp. 495-499.

MARTIN, A.C., 2010. Pulsation and stabilization: contractile forces that underlie morphogenesis. *Developmental biology,* **341**(1), pp. 114-125.

MARUSYK, A. and POLYAK, K., 2010. Tumor heterogeneity: causes and consequences. *Biochimica et biophysica acta,* **1805**(1), pp. 105-117.

MICAH, D. and WAN, Y., 1999. Stresses at the Cell-to-Substrate Interface During Locomotion of Fibroblasts. *Biophysical Journal,* **76**, pp. 2307-2316.

NODDER, S. and MARTIN, P., 1997. Wound healing in embryos: a review. *Anatomy and Embryology,* **195**(3), pp. 215-228.

PALSSON, E., 2001. A three-dimensional model of cell movement in multicellular systems. *Future Generation Computer System,* **17**, pp. 835-852.

PHILLIPS, H. and STEINBERG, M.S., 1969. Equilibrium measurements of embryonic chick cell adhesiveness, I: Shape equilibrium in centrifugal fields. *Proceedings of the National Academy of Sciences of the United States of America,* **64**, pp. 121-127.

PILOT, F. and LECUIT, T., 2005. Compartmentalized morphogenesis in epithelia: From cell to tissue shape. *Developmental Dynamics,* **232**, pp. 685-694.

RAMASUBRAMANIAN, A., LATACHA, K.S., BENJAMIN, J.M., VORONOV, D.A., RAVI, A. and TABER, L.A., 2006. Computational model for early cardiac looping. *Annals of Biomedical Engineering,* **34**(8), pp. 1355-1369.

RAUZI, M. and LECUIT, T., 2009. Closing in on mechanisms of tissue morphogenesis. *Cell,* **137**(7), pp. 1183-1185.

RAUZI, M., VERANT, P., LECUIT, T. and LENNE, P.F., 2008. Nature and anisotropy of cortical forces orienting Drosophila tissue morphogenesis. *Nature cell biology,* **10**(12), pp. 1401-1410.

ROHDE, L.A. and HEISENBERG, C., 2007. Zebrafish gastrulation: cell movements, signals, and mechanisms. *International Review of Cytology,* **261**, pp. 159-192.

SAID, N. and THEODORESCU, D., 2009. Pathways of metastasis suppression in bladder cancer. *Cancer metastasis reviews,* **28**(3-4), pp. 327-333.

SAUSEDO, R.A., SMITH, J.L. and SCHOENWOLF, G.C., 1997. Role of nonrandomly oriented cell division in shaping and bending of the neural plate. *The Journal of comparative neurology,* **381**(4), pp. 473-488.

SHIBUE, T. and WEINBERG, R.A., 2011. Metastatic colonization: settlement, adaptation and propagation of tumor cells in a foreign tissue environment. *Seminars in cancer biology,* **21**(2), pp. 99-106.

SOLON, J., KAYA-COPUR, A., COLOMBELLI, J. and BRUNNER, D., 2009. Pulsed forces timed by a ratchet-like mechanism drive directed tissue movement during dorsal closure. *Cell,* **137**(7), pp. 1331-1342.

STEINBERG, M.S., 1996. Adhesion in development: An historical overview. *Developmental Biology,* **180**, pp. 377-388.

STEINBERG, M.S., 1963. Reconstruction of tissues by dissociated cells. *Science,* **141**(3579), pp. 401-408.

STEINBERG, M.S., 1970. Does differential adhesion govern self-assembly process in histogenesis? Equilibrium configurations and the emergence of a hierarchy among populations of embryonic cells. *Journal of Experimental Zoology,* **173**, pp. 395-434.

STOLTZ, J.F. and WANG, X., 2002. From biomechanics to mechanobiology. *Biorheology,* **39**, pp. 5-10.

SUN, M.Z., GRAHAM, J.S., HEGEDUS, B., MARGA, F., ZHANG, Y., FORGACS, G. and GRANDBOIS, M., 2005. Multiple membrane tethers probed by atomic force microscopy. *Biophysical journal,* **89**(6), pp. 4320-4329.

TAMBE, D.T., CROUTELLE, U., TREPAT, X., PARK, C.Y., KIM, J.H., MILLET, E., BUTLER, J.P. and FREDBERG, J.J., 2013. Monolayer stress microscopy: limitations, artifacts, and accuracy of recovered intercellular stresses. *PloS one,* **8**(2), pp. e55172.

TANEMURA, M., 1988. Random packing and random tessellation in relation to the dimension of space. *Journal of microscopy,* **151**, pp. 247-255.

TANEMURA, M., OGAWA, T. and OGITA, N., 1983. A new algorithm for three-dimensional Voronoi tessellation. *journal of computational physics,* **50-51**, pp. 191-207.

THOMAS, G., BURNHAM, N.A., CAMESANO, T.A. and WEN, Q., 2013. Measuring the mechanical properties of living cells using atomic force microscopy. *Journal of visualized experiments : JoVE,* **(76). doi**(76), pp. 10.3791/50497.

TREPAT, X., WASSERMAN, M.R., THOMAS, E.A., MILLET, E., WEITZ, D.A., BUTLER, J.P. and FREDBERG, J.J., 2009. Physical Forces during Collective Cell Migration. *Nature Physics,* **5**, pp. 426.

TRINKAUS, J.P., 1984. *Cells Into Organs: The Forces the Shape the Embryo.* Englewood Cliffs, NJ: Prentice-Hall.

UMEDA, T. and INOUYE, K., 2004. Cell sorting by differential cell motility: a model for pattern formation in Dictyostelium. *Journal of Theoretical Biology,* **226**, pp. 215-224.

VARNER, V.D., VORONOV, D.A. and TABER, L.A., 2010. Mechanics of head fold formation: investigating tissue-level forces during early development. *Development (Cambridge, England),* **137**(22), pp. 3801-3811.

VELDHUIS, J.H., BRODLAND, G.W., WIEBE, C.J. and BOOTSMA, G.J., 2005. Multiview robotic microscope reveals the in-plane kinematics of amphibian neurulation. *Annals of Biomedical Engineering,* **33**(6), pp. 821-828.

VIENS, D. and BRODLAND, G.W., 2007. A three-dimensional finite element model for the mechanics of cell-cell interactions. *Journal of Biomechanical Engineering,* **129**(5), pp. 651-657.

WALGENBACH, K.J., VOIGT, M., RIABIKHIN, A.W., ANDREE, C., SCHAEFER, D.J., GALLA, T.J. and BJÖRN, G., 2001. Tissue engineering in plastic reconstructive surgery. *The Anatomical Record,* **263**(4), pp. 372-378.

WONG, V.W., AKAISHI, S., LONGAKER, M.T. and GURTNER, G.C., 2011. Pushing back: wound mechanotransduction in repair and regeneration. *The Journal of investigative dermatology*, **131**(11), pp. 2186-2196.

YANG, J. and BRODLAND, G.W., 2009. Estimating Interfacial Tension from the Shape Histories of Cells in Compressed Aggregates: A Computational Study. *Annals of Biomedical Engineering*, .

ZAMIR, E.A., CZIRÓK, A., RONGISH, B.J. and LITTLE, C.D., 2005. A digital image-based method for computational tissue fate mapping during early avian morphogenesis. *Annals of Biomedical Engineering*, **33**(6), pp. 854-865.